PLASMA BASED METHODS FOR THE SYNTHESIS AND DEPOSITION OF NANOPARTICLES

By

Alexander Ho

A DISSERTATION

Submitted to
Michigan State University
in partial fulfillment of the requirements
for the degree of

Mechanical Engineering – Doctor of Philosophy

2022

ABSTRACT

PLASMA BASED METHODS FOR THE SYNTHESIS AND DEPOSITON OF NANOPARTICLES

By

Alexander Ho

Nanoparticles exhibit tunable properties that offer the opportunity to improve existing technologies. Nanoparticles also posses emergent properties that are not shared by their bulk scale counterparts; this difference in properties allows for application of materials in devices and processes that were traditionally unsuitable. For semiconducting nanoparticles, the emergent and tunable properties hold promise for applications in solar cells, light emitting devices, sensors, catalysis, and a variety of other spaces.

Explored first was the synthesis of InN, GaN, and $In_xGa_{1-x}N$ at low pressure. These materials posses properties suitable for high-power and high-frequency electronics applications. The materials also posses bandgaps that span from the IR to the UV allowing for the use in a host of optoelectronic applications. A low pressure RF plasma reactor was used to dissociate precursor gases whose subsequent reactions formed the nanoaprticles. Nanoaprticles were then collected and characterized with a host of techniques. Experiments were conducted that demonstrated the synthesis of crystalline nanoparticles with narrow size distributions. It was shown that particle size and crystallinty could be controlled through modulation of residence time and RF power respectively. This method demonstrated the synthesis of luminescent $In_xGa_{1-x}N$ nanoparticles without any subsequent surface modification or post-synthesis treatment.\par

To eliminate the time and capital costs of vacuum equipment and processes an atmospheric pressure microplasma operated with ambient surroundings was investigated. With this method crystalline silicon nanoparticles were synthesized. OES and FTIR were used in conjunction to ascertain if particles were synthesized in an oxygen contaminated environment. Results of the experiments indicate particles were not exposed to oxygen in the reaction volume.\par

Lastly an integrated atmospheric pressure synthesis reactor and aerosol jet printing process are described. Such a process would be useful for fabrication or prototyping of devices that require nanoparticles. Combination of the reactor with a motorized stage and gantry allowed for deposition of nanoparticles with linewidths down to 100 microns. Methods to improve impaction efficiency were implemented and allowed for capture of sub-5 nm particles that exhibited luminescence at 680 nm. Also demonstrated was the control of synthesis parameters at the time of deposition to deposit particles with spatially varied properties.

Dedicated to my parents, sister, and friends.

ACKNOWLEDGEMENTS

I would like to give thanks to all of my fellow lab mates for their time spent discussing and conducting experiments. I would also like to thank Dr. Per Askeland for his assistance with various microscopy and spectroscopy techniques. My thanks is also expressed to Dr. John McCracken for his assistance with magnetic resonance studies and engaging conversations. Finally, I want to express my deepest gratitude to my advisor Dr. Rebecca Anthony. Without her time, guidance, and willingness to offer an opportunity for graduate studies, this work would not have been possible.

TABLE OF CONTENTS

LIST OF TABLES ix

LIST OF FIGURES x

KEY TO ABBREVIATIONS xv

CHAPTER 1 INTRODUCTION 1
- 1.1 Motivation for study of Nanoparticle Synthesis and Deposition 1
- 1.2 Primer on Semiconductor Nanoparticles 2
- 1.3 Nonthermal Plasma Synthesis 3
- 1.4 Aerosol Jet Printing 5
- 1.5 Outline of Work 6

CHAPTER 2 EXPERIMENTAL METHODS 7
- 2.1 X-Ray Diffraction 7
- 2.2 Microscopy 8
  - 2.2.1 Transmission Electron Microscopy 8
    - 2.2.1.1 Selected Area Electron Diffraction 10
    - 2.2.1.2 Energy Dispersive X-Ray Spectroscopy 11
  - 2.2.2 Scanning Electron Microscopy 11
  - 2.2.3 Optical Microscopy 11
- 2.3 Spectroscopy 11
  - 2.3.1 Fourier Transform Infrared Spectroscopy 11
  - 2.3.2 Photoluminescence Spectroscopy 12
  - 2.3.3 X-Ray Photoelectron Spectroscopy 12
  - 2.3.4 Electron Paramagnetic Resonance 13
  - 2.3.5 UV-VIS Absorption Spectroscopy 14

CHAPTER 3 LOW-PRESSURE SYNTHESIS OF GaN, InN, AND $In_XGa_{1-X}N$ NANOPARTICLES 17
- 3.1 Introduction 17
- 3.2 Experimental Methods 18
  - 3.2.1 Low-Pressure Plasma Reactor 18
- 3.3 Results and Discussion 22
  - 3.3.1 Gallium Nitride Nanoparticle Synthesis 22
    - 3.3.1.1 Size and Crystallinty Analysis 22
    - 3.3.1.2 Composition and Surface Analysis 25
    - 3.3.1.3 Optical Properties and Defect Characterization 31
  - 3.3.2 Indium Nitride Nanoparticle Synthesis 33
    - 3.3.2.1 Size and Crystallinty Analysis 33
    - 3.3.2.2 Composition and Surface Analysis 36
    - 3.3.2.3 Optical Properties 37

3.3.3 Indium$_x$ Gallium$_{1-x}$ Nirtide Synthesis 38
3.3.3.1 Size and Crystallinty Analysis 38
3.3.3.2 Composition and Surface Analysis 43
3.3.3.3 Optical Properties 45
3.4 Conclusions 48

CHAPTER 4 ATMOSPHERIC PRESSURE SYNTHESIS OF SILICON NANOPARTICLES 49
4.1 Introduction 49
4.2 Experimental Setup 49
4.2.1 Atmospheric Pressure Reactor 49
4.3 Results and Discussion 51
4.3.1 Process and Structural Characterization 51
4.3.2 Surface Oxidation 55
4.3.3 Optical Properties 59
4.4 Conclusion 60

CHAPTER 5 DRY AEROSOL JET PRINTING OF SILICON NANOPARTICLES 61
5.1 Introduction 61
5.2 Experimental Setup 62
5.3 Results and Discussion 64
5.3.1 Printing Resolution 64
5.3.2 Impaction Efficiency 66
5.3.3 Spatially Varied Particle Printing 72
5.4 Conclusions 74

CHAPTER 6 CONCLUSIONS AND FUTURE WORK 75
6.1 Nitrides Synthesis 75
6.2 Atmospheric Pressure Synthesis 76
6.3 Nanoparticle Printing 77

APPENDICES 78
APPENDIX A POWER DENSITY MEASUREMENT AND CALCULATION 79
APPENDIX B FLOW ANALYSIS 82

BIBLIOGRAPHY 87

LIST OF TABLES

Table 3.1: Table listing average diameter of particle synthesized at different TMG flowrates. 41

Table 3.2: Table listing flowrates of metallic precursor gases and the resulting ratio of observed metallic species as measured by EDS. 44

Table 3.3: Table listing TMG and TMI flowrates and peak PL emission for $In_xGa_{1-x}N$ samples. 46

Table 4.1: Table listing parameters for silicon nanoparticles and the resulting silane concentration and residence time. 54

Table 5.1: Table linewidths of deposits from different nozzle diameters. 66

Table 5.2: Table listing the number of aerodynamic lenses and associated diameter of spot deposition. 70

Table 5.3: Table listing the magnitude of the applied voltage and associated diameter of spot deposition. 71

LIST OF FIGURES

Figure 1.1: Energy momentum diagrams that form band structure of common semiconductors.[1] . . . 3

Figure 1.2: Image of a nonthermal plasma reactor. . . . 4

Figure 1.3: Depiction of aerosol jet printing process. . . . 5

Figure 2.1: (a) Bright-field TEM image with crystalline particle near center of image. (b) FFT of image with spots marked with white circles. Inverse FFT of image with yellow line used to plot grayscale profile for lattice spacing measuremnt. . 10

Figure 2.2: Energy diagram of electron spin states depicting energy level splitting with application of magnetic field.[2] . . . 14

Figure 2.3: (a) Simulated absorption spectrum. (b) Resulting Tauc plot after conversion of data to absorption and then $(\alpha h\nu)^n$ . . . 16

Figure 3.1: Comparison of GaN, $In_xGa_{1-x}N$, and InN nanoparticles. . . . 18

Figure 3.2: Rendering of experimental setup used to synthesize nitride materials. Not shown here are two heaters used to heat TMI lines to reduce risk of condensation of TMI in the process . . . 20

Figure 3.3: Typical reactor configuration used for synthesis of nitride materials. Background and precursor gases enter from the top of the reactor, enter the reaction zone where particles are synthesized, particles are then carried by the gas flow and collected on substrates beneath the orifice. . . . 21

Figure 3.4: Diffraction pattern obtained for particles synthesized with residence time of 51 ms. Long tick marks denote the central locations of peaks obtained from Rietveld refinement of diffraction pattern. . . . 22

Figure 3.5: Representative TEM images of GaN nanoparticles synthesized at different powers. (a) Particles synthesized at 130 W. (b) Particles synthesized at 150 W. (c) Particles synthesized at 175 W. . . . 24

Figure 3.6: Nanoparticle size distributions synthesized at different residence times. Black curves are normal distribution overlays. Number at the top of each bin denotes the number of particles counted in each bin . . . 25

Figure 3.7: XPS spectra of the (a) Ga 2p3/2, (b) C 1s, (c) N 1s, and (d) O 1s peaks. Each peak is an average of three samples with the standard deviation denoted by the shaded region 26

Figure 3.8: FTIR spectra of GaN nanoparticles that displays change in particle surface with time. 27

Figure 3.9: Reduced range of FTIR spectrum from 400-850 cm^{-1} where deconvolution of the spectrum has yielded component peaks corresponding to a variety of vibrational modes at the particle surface. 29

Figure 3.10: Reduced range of FTIR spectrum from 2000-2200 $cm^{-1}$where deconvolution of the spectrum has yielded component peaks corresponding to a variety of vibrational modes at the particle surface. 29

Figure 3.11: Reduced range of FTIR spectrum from 2400-3750 $cm^{-1}$where deconvolution of spectrum has yielded component peaks corresponding to a variety of vibrational modes at the particle surface. 30

Figure 3.12: (a)Tauc plot of bulk GaN.[3] (b)Tauc plot with fitted line to linear portion of the plot. Intersection of dashed red line with the absiccca corresponds to the estimated bandgap. 31

Figure 3.13: Representative EPR spectrum of GaN nanoparticles. 33

Figure 3.14: TEM images of InN nanoparticles at different magnifications. 34

Figure 3.15: SAED pattern of InN nanoparticles. With equivalent 2ϑ values denoted at the extrema of the rings. 34

Figure 3.16: XRD pattern fitted to hexagonal InN. Diffraction pattern is a convolution of the component peaks. 35

Figure 3.17: Representative FTIR spectrum of InN nanoaprticles. 37

Figure 3.18: Tauc plot obtained from UV-VIS-NIR absorption spectrum of InN nanoparticles. 38

Figure 3.19: (a) Plot displaying the various residence times used to synthesize $In_xGa_{1-x}N$ nanoparticles and the rate of deposition.(b) Plot comparing the power density as measured using a voltage proxy (v) method or subtractive method (s) against the rate of deposition. 39

Figure 3.20: Bar charts that depict the relationship between the deposition rate and the relative flowrates (Q denotes the sum of all flows). The charts display the same data differing only by the scale of the "Percentage of Flow" axis. 40

Figure 3.21: Comparison of XRD patterns for InN, $In_xGa_{1-x}N$, and GaN nanoparticles. The tick marks denote location of either InN or GaN peak positions from ICSD 42

Figure 3.22: (a) TEM image of $In_xGa_{1-x}N$ nanoparticles. (b) SAED pattern of $In_xGa_{1-x}N$ nanoparticles. (c) Conversion of SAED pattern to XRD using radial intensity of SAED and conversion from reciprocal space to 2ϑ space. 42

Figure 3.23: (a) XRD pattern of $In_xGa_{1-x}N$ nanoparticles synthesized with increasing TMG flowrate and constant TMI flowrate. (b) XRD pattern of $In_xGa_{1-x}N$ nanoparticles synthesized with increasing TMI flowrate and constant TMG flowrate. . . 44

Figure 3.24: FTIR spectra of GaN, $In_xGa_{1-x}N$, and InN nanoparticles. 45

Figure 3.25: (a) Image of PL from $In_xGa_{1-x}N$ sample with 405 nm LED. (b) PL spectra of $In_xGa_{1-x}N$ nanoaprticles excited with 405 nm LED 47

Figure 3.26: (a) PL emitted from $In_xGa_{1-x}N$ sample immediatley ater synthesis, 3 days, and 6 days post synthesis.(b) PL emitted from $In_xGa_{1-x}N$ samples at 1 and 3 days post synthesis. 47

Figure 4.1: Rendering of components used to synthesize silicon nanoparticles at atmospheric pressure. Not depicted here is stainless steel enclosure used to create air-free environment for synthesis. Enclosure contained the reactor, stage, and associated components used to move the stage and reactor. 51

Figure 4.2: (a) XRD of silicon nanoparticles synthesized at 90W with diffraction peaks in positions typical of silicon nanoparticles. (b) TEM image of silicon nanoparticles synthesized at 90 W with lattice fringes present. 52

Figure 4.3: (a) Indexed SAED pattern of silicon nanoparticles. (b) Dark-Field TEM image of silicon nanoparticles. 53

Figure 4.4: Change in nanoparticle diameter at various combinations of argon and silane flowrates. 54

Figure 4.5: Depositon rate of silicon nanoparticles onto the reactor walls and substrate. . . . 55

Figure 4.6: (a)Comparison of OES spectra collected with a surrounding argon atmosphere and an air atmosphere.(b) OES spectra collected at various distances from the reactor outlet with a surrounding air atmosphere 56

Figure 4.7: FTIR spectra of silicon nanoparticles taken at time several intervals post synthesis. 57

Figure 4.8: FTIR spectra of silicon nanoparticles taken at time several intervals post synthesis. 58

Figure 4.9: (a) Tauc plot of silicon nanoparticles. (b) PL spectrum of nanoparticles. Inset is deposition of particles onto a copper substrate, the central portion did not exhibit PL while the outer edge had visible PL. 60

Figure 5.1: Rendering of components used to deposit silicon nanoparticles with inkless aerosol jet printing approach. 62

Figure 5.2: From left to right: CAD model, software generated tool path, and sample. . . . 63

Figure 5.3: Rendering and Image of tubes used for aerodynamic lenses. 64

Figure 5.4: Optical image of silicon nanoparticles deposited in a line. 65

Figure 5.5: SEM image of nanoparticles deposited onto silicon wafer. Exposed section was milled with FIB. 66

Figure 5.6: Plot displaying the interplay between nozzle diameter, flow velocity, pressure, and nanoparticle diameter on the Stokes number. 67

Figure 5.7: Difference in deposition of particles synthesized at the same conditions but deposited at chamber pressures of 4 Torr and 760 Torr. 68

Figure 5.8: (a) Deposition of particles from straight ended tube with no intervention.(b) Deposition from straight ended tube with two aerodynamic lenses.(c) Deposition from straight ended tube with substrate biased by high voltage power supply. 69

Figure 5.9: (a) Radial position of particles released at different initial radial positions as a function of the tube length.(b) Relative change between the initial and final radial position for each particle. 70

Figure 5.10: (a) SEM image of nanoparticles deposited with two aerodynamic lenses.(b) SEM image of nanoparticles deposited with substrate biased by high voltage power supply.(c) Cross sectional SEM image of nanoparticles deposited with substrate biased by high voltage power supply. 72

Figure 5.11: (Row 1) Bright-field TEM images of silicon nanoparticles synthesized at different powers.(Row 2) Dark-field TEM images of silicon nanoparticles synthesized at different powers.(Row 3) SAED patterns of silicon nanoparticles synthesized at different powers.(Row 4) XRD patterns of silicon nanoparticles synthesized at different powers. 73

Figure A.1: Comparison of voltage proxy and subtractive method for power transfer estimation. 81

Figure B.1: Plots of Pe for different gas flow velocities and pressures. Pe is plotted for both calculations of the friction coefficient. 84

Figure B.2: Schlieren images of jets impinging upon substrates.[4] 86

KEY TO ABBREVIATIONS

LED Light-emitting device

0D Zero-dimensional

1D One-dimensional

2D Two-dimensional

CAD Computer-aided design

CAM Computer-aided manufacturing

XRD X-ray diffraction

SAED Selected area electron diffraction

TEM Transmission electron microscopy

FFT Fast Fourier transform

EDS Energy disperisve X-ray spectroscopy

SEM Scanning electron microscopy

FTIR Fourier transform infrared spectroscopy

PL Photoluminescence spectroscopy

XPS X-ray photoelectron spectroscopy

EPR Electron paramagnetic resonance

UV-VIS Ultraviolet-Visible

OES Optical emission spectroscopy

GaN Gallium nitride

InN Indium nitride

InGaN Indium gallium nitride

ALD Atomic layer deposition

CVD Chemical vapor deposition

MOCVD Metal organic vapor deposition

RF Radio-frequency

TMG	Trimethylgallium
TMI	Trimethylindium
NH_3	Ammonia
Ar	Argon
MFC	Mass flow controller
τ	Residence time
Stk	Stokes number
Es	Electrostatic number

CHAPTER 1

INTRODUCTION

1.1 Motivation for study of Nanoparticle Synthesis and Deposition

Energy consumption has risen by 53% since 1995[5] and as many nations continue to develop, energy needs will likely increase for the foreseeable future. As such it will be necessary to develop sustainable technologies that can support the demands of a developing planet. Many of the already developed countries benefited from the commercial and industrial use of conventional energy sources such as fossil fuels. While this energy source has provided enormous benefit to the human populous there is the risk to serious environmental, and economic damage if long-term use of fossil fuels continues to be the major source of energy globally, without the increase of energy production from renewable sources.[6]

To reduce the demand of energy from fossil fuels, electrification of devices and processes that currently rely on fossil fuels would provide benefit. Such devices or processes may include: energy production, thermal industrial processes, transportation, heating, and cooling. Clear pushes towards electrification have been made with the commercial and industrial use of windmills, solar cells, electric cars, electric appliances, etc. Many of the devices that exist can be improved through increases in efficiency, utilization, and tailoring of application space.

Many devices are limited by the materials that they are composed of because the properties determine the operational limits of the device. There are many ways to change materials properties through electrical, mechanical, and chemical processing. In the space of nanomaterials the properties of the material can be altered by controlling the size of the material. Such tunablity allows for the production of light-emitting devices (LEDs) that can emit in the infrared, visible, and ultraviolet range of the electromagnetic spectrum.[7–9] Similarly such materials can absorb in these regions allowing for their integration into solar cells. The tunablity of properties can also be extended to applications in biological materials,[10,11] catalysis,[12] and energy storage.[13]

1.2 Primer on Semiconductor Nanoparticles

Evidence of nanoparticle use dates roughly 4000 years[14] with evidence of chemical synthesis occuring between 1400 and 1300 BC.[15] Most early uses of particles were as additives for dyes and pigments. The first scientific documentation of nanoparticle preparation is attributed to Micheal Faraday in 1857 for a gold colloid with optical characteristics differing from its bulk counterpart.[16] With the development of quantum mechanics in the 1900's a formal understanding of nanoparticle behavior was made and today .

Nanomaterials are materials who have at least one dimension under 1000 nm, more often the range spans from ones to a few hundred nm. Nanoparticles are zero-dimensional (0D) materials where all spatial dimensions are confined to the nanoscale. This in contrast to one-dimensional (1D) or two-dimensional (2D) which have either one or two spatial dimensions confined to the nanoscale; common examples of such materials are carbon nanotubes and graphene respectively. Nanoparticles are not limited to the conventional classifications of materials; metals, ceramics, and polymer nanoparticles all exist. Nanoparticles are encountered quite often as byproducts of many commercial, industrial, and consumer processes. Semiconductor nanoparticles are of particular interest because the electronic structure of the materials and resulting properties are dependent on the "size" of the particles. Size is used with some ambiguity to refer to the total states available to electrons in the particle - often the diameter is used to characterize the size of particles. A crucial property of semiconductors is the band gap of the material, which is defined as the difference in energy between the valence and conduction band maximum and minimum, respectively. The valence band describes the set of ground energy states that electrons occupy in a semiconducting or insulating material whereas the conduction band describes the set of excited states an electron can occupy in the material. The band gap is a region of energies that electrons cannot occupy when in the material. While not readily obvious this property allows for the function of many modern electronics, when the size of the band gap is compatible with either optical or electrical excitation of electrons from the valence band states into the conduction band.

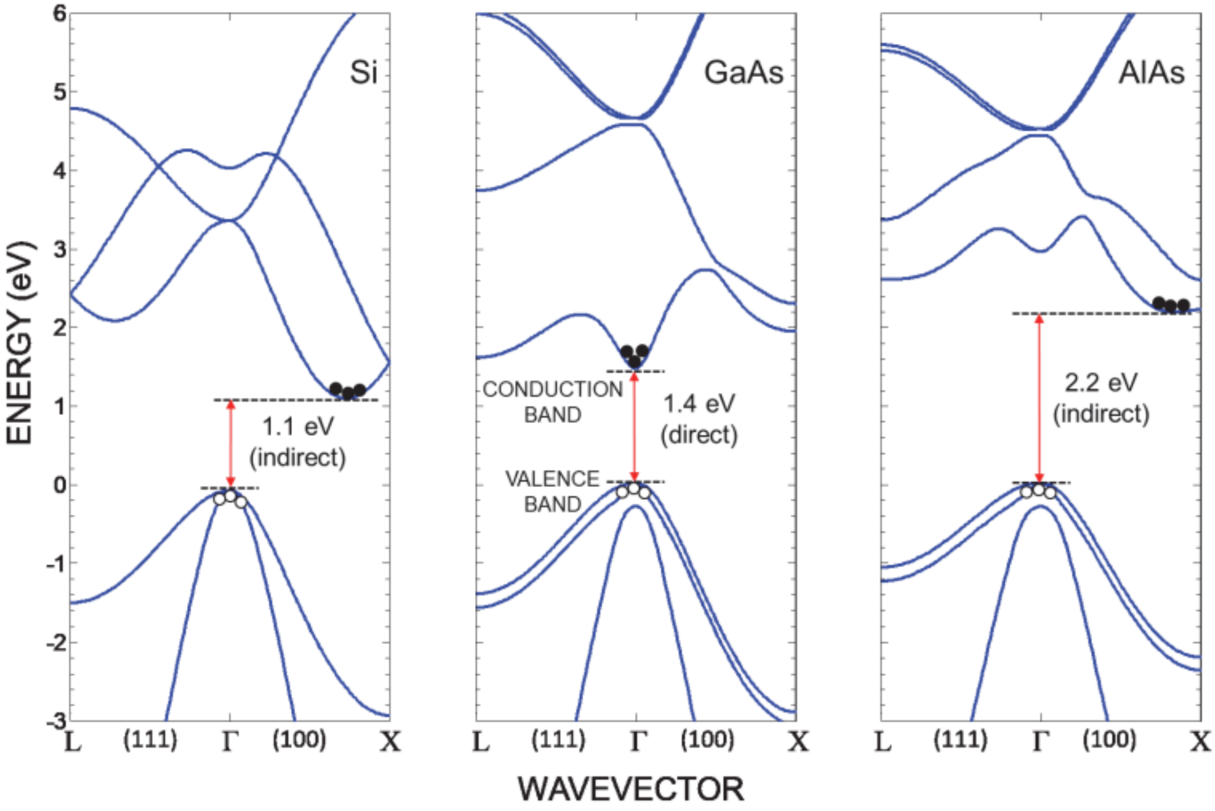

Figure 1.1: Energy momentum diagrams that form band structure of common semiconductors.[1]

Quantum confinement of materials is said to occur when the diameter of the particle approaches the Bohr-exciton radius of that material. The Bohr-exciton radius can be calculated with the following relationship,

$$a_b = \epsilon_r \frac{m_e}{\mu} a_0 \tag{1.1}$$

where a_b is the Bohr-exciton radius, ε is the materials dielectric constant, μ is the reduced mass, and a_0 is the Bohr radius. Typical value range from one's to tens of nanometers. Once materials approach their Bohr-exciton radius size related shifts of their properties occur.

1.3 Nonthermal Plasma Synthesis

Nanoparticle synthesis can be broadly categorized into liquid or gas phase synthesis. Liquid phase processes have been used to synthesize group II-VI and IV-VI semiconductors but these processes are often limited by boiling points of the solvents making the use of such processes

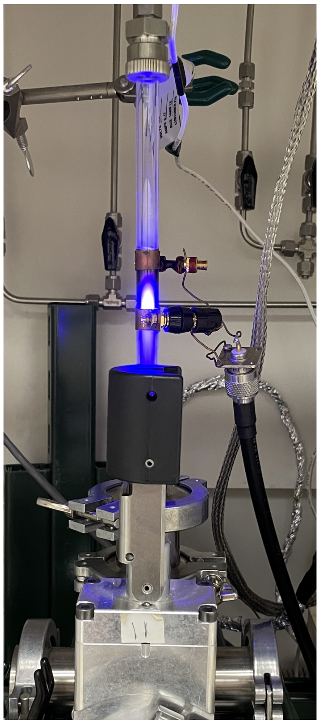

Figure 1.2: Image of a nonthermal plasma reactor.

difficult to synthesize other types of materials.[17] Gas phase synthesis inherently does not require solvents and can be used to synthesize crystalline nanoparticles of many kinds.[18–21] Gas phase synthesis may be further subdivided into thermal and nonthermal techniques. Common thermal techniques include laser pyrolysis, thermal pyrolysis, and thermal plasmas. While these methods are successful at producing nanoparticles they are prone to particle agglomeration due to lack of charged species and the high temperatures typically involved.[17] This agglomeration may result in large size distributions which may lead to an undesired dispersion to the properties of synthesized materials. A prominent nonthermal method for the synthesis of nanoparticles is nonthermal plasma (also called low-temperature plasma) whose defining feature is that the plasma species are not in thermal equilibrium with one another (i.e. plasma species have different temperatures). During synthesis nanoparticles tend to take on a net negative charge suppressing particle agglomeration leading to narrow size distributions which is desired for uniformity of properties within a sample.[22]

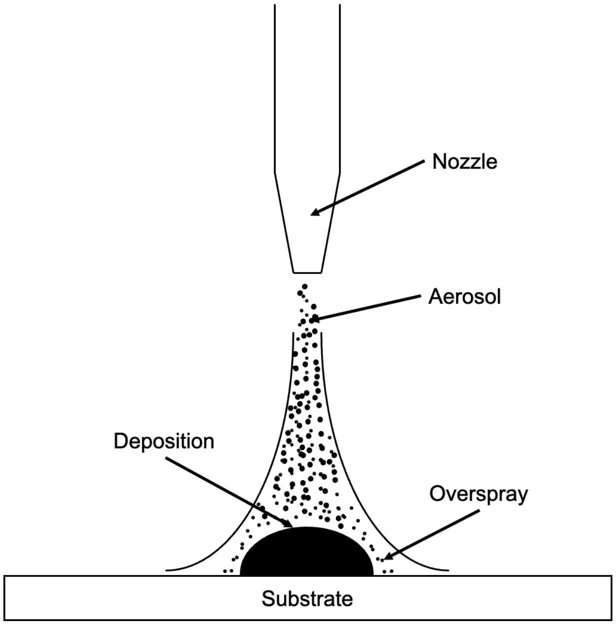

Figure 1.3: Depiction of aerosol jet printing process.

1.4 Aerosol Jet Printing

Additive manufacturing promises to play an important role in the future of manufacturing processes. The popularized fused deposition modeling for the additive manufacturing with polymers has brought the use of such techniques to the common vernacular. Additive manufacturing is not limited to polymers and well defined processes have been developed for not just polymers but metals, ceramics, and biological materials. Additive manufacturing can be categorized into several groups, of which one is direct-write processes. Direct-write processes are used to controllably deposit features onto substrates in patterns defined with computer-aided design (CAD) and computer-aided manufacturing (CAM) programs.[23]

Aerosol jet printing is a direct write process where an aerosol composed of a carrier gas and a particulate phase is directed towards a substrate to form desired patterns. Often a solid phase is dispersed into a liquid which is then atomized and carried to the substrate. The use of liquid is done to achieve viscosities suitable for atomization as well as aiding in deposition of the material.

1.5 Outline of Work

This work examines the RF plasma synthesis of gallium ntiride, indium nitride, indium gallium nitride, and silicon. The synthesis method is a continuous all gas phase approach wherein powders of nanoparticles are collected. Explorations of synthesis and deposition schemes at low-pressure and atmospheric pressure are explored.

Chapter 3 is divided into three sections to examine low-pressure synthesis of GaN, InN, and $In_xGa_{1-x}N$. The relationship between synthesis parameters and the resulting particle crystallinty, size distribution, emission and absorption properties, and defects is presented. While many demonstrations of synthesis of such particles have been achieved plasma based synthesis reports are limited. We demonstrate that with this method particles can be synthesized with sizes smaller than their Bohr-exciton radius. Further demonstrated is the ability to control particle size and crystallinty by adjusting synthesis parameters. Photon emission from $In_xGa_{1-x}N$ nanoparticles was observed for the first time with a gas phase method.

Chapter 4 describes the use of an atmospheric pressure reactor for the synthesis of silicon nanoparticles with ambient air surroundings. Experiments were conducted to determine relationship between synthesis parameters and the resulting particle size distribution and crystallinty. Study of particle oxidation and gas species in the plasma were conducted to demosntrate that particles are synthesized in a near oxygen free environment at the time of synthesis. Examination of the optical proeties indicated that particles had a blue-shifted bandgap with emission at 605 nm.

Chapter 5 examines the integration of the atmospheric pressure reactor with a motorized system to explore the use of plasma synthesis for aerosol jet printing of nanoparticles. With system it is demonstrated that particle properties can be controlled at the time of deposition. Methods to improve printing resolution and reduce overspray are examined.

CHAPTER 2

EXPERIMENTAL METHODS

Several instruments and techniques were used to characterize samples. The general procedure used with each instrument is described in the following sections. If deviations from the following procedures were used they will be noted and described as they appear in the text.

2.1 X-Ray Diffraction

X-ray Diffraction (XRD) is a powerful technique that relies upon the interaction of atoms and x-ray radiation to produce data related to the structure and composition of solid (bulk, powder, or thin-film) samples. XRD patterns manifest from the combination of constructive and deconstructive interference. The periodic arrangement of atoms in a crystal lattice results in the diffraction of incident x-rays, the diffracted rays then form an interference pattern. When conducting XRD there is a source arm and detector arm. During a scan the intensity of diffracted x-rays is plotted against the angle between the incident beam and the detector. Typical interference patterns display peaks at particular locations where a periodic arrangement of atoms is present. Bragg's Law relates the interplanar spacing of atoms to the Bragg angle which can be used for material identification.

$$n\lambda = 2dsin(\theta) \tag{2.1}$$

Further information can be obtained from the interference pattern by examination of the peak width. The primary sources of peak width are Scherrer broadening, lattice strain, and instrumental broadening. Scherrer broadening occurs when the crystalline size becomes sufficiently small such that the typically delta-like reflections from a bulk crystal sample begin to broaden[24] according to,

$$\tau = \frac{K\lambda}{\beta_{size}cos(\theta)} \tag{2.2}$$

Here τ is the characteristic diameter of the diffracting domain (particle diameter), K is the shape factor, λ is the wavelength of the incident x-ray, β_{size} is the size related width of the peak, and ϑ is the Bragg angle. The shape factor is a constant with values from 0.6 to 2.04, 0.89 is commonly used for spherical particles.[25] The peak width needs to be treated with care considering that there are multiple contributions to the peak width. Instrumental broadening must always be removed from the peak width. Instrumental broadening is typically measured with a NIST traceable reference sample such as lanthanum hexaboride, such samples are carefully produced and tested to ensure that any peak broadening is a result of the instrument. To obtain the instrumental broadening profile measurement of the reference sample with the same conditions used for measurement of typical samples is conducted. The instrumental broadening is often related the sample broadening with the following relationship.

$$\beta^2 = \beta_i^2 + \beta_{sample}^2 \tag{2.3}$$

Here β is the width of the peak, β_i is the instrumental broadening width and β_{sample} is broadening from the sample. Strain can be accounted for with the methods described by Willliamson and Hall[26] or Warren and Averbach.[27] The computational method of Rietveld refinement is often used to create a calculated diffraction pattern that matches the measured pattern. From the model parameters such as size and strain can be extracted.[28] Samples were prepared for XRD by depositing samples onto glass slides. A Rigaku Smart Lab X-ray diffractometer was use to analyze samples. The diffractometer was operated in parallel beam mode with a Cu-kα x-ray source. The source arm angle (ω) was held slightly below (0.1 deg) the critical angle of the material being analyzed. This was done to increase the intensity from the samples. A 2ϑ scan was then performed with a step size of 0.0400 degrees with typical 2ϑ range of 20 to 80 degrees over the course of 30 minutes to 1 hour.

2.2 Microscopy

2.2.1 Transmission Electron Microscopy

Transmission electron microscopy (TEM) is a microscopy technique that utilizes an electron beam for imaging at ultra-high resolution. TEM images can be be constructed from the bright-field or the dark-field. These images correspond to measurement of different populations of electrons. The bright-field images are constructed from electrons that transmit through the sample thus areas of crystalline or high mass material will be dark. Dark-field images are constructed from scattered electrons this results in areas with sample to be bright and other areas to be dark. Combination of bright and dark field imaging is useful to examine the structure of nanoparticles. The bright field imaging allows for observation of crystal structure through observation of lattice fringes. It can also be used to identify if core-shell structures are present. Dark-field imaging provides an additional means to verify if particles are crystalline. The crystalline lattice will strongly scatter the electrons resulting in bright spots that readily allow for identification of crystalline material.

Lattice spacing measurements from TEM can be performed with the use of image processing software. Herein ImageJ was used to process TEM images and perform analysis. To measure lattice spacing the popular "dm3" file type was used which contains inforamtion related to scale of image. This helps remove user bias by eliminating the need to set the scale manually. An FFT of the image is then taken which effectively converts the image from real space to reciprocal space. Spots in the FFT are then marked and the inverse FFT is taken to return image to real space. This produces an image where only particles displaying crystalline features are present. A straight line is then drawn in parallel with the lattice and the angle tool is used to draw a line orthogonal to it. A profile plot of the gray scale value is then generated from which the number of peaks and distance is used to estimate the lattice spacing. This method is not perfect and can have errors that exceed 10%.[29–32]

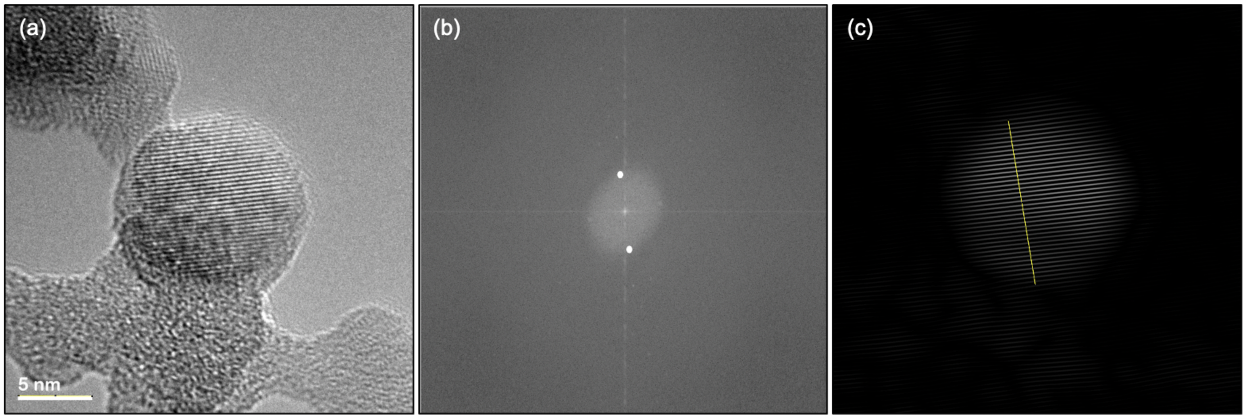

Figure 2.1: (a) Bright-field TEM image with crystalline particle near center of image. (b) FFT of image with spots marked with white circles. Inverse FFT of image with yellow line used to plot grayscale profile for lattice spacing measuremnt.

Several corollary techniques are often incorporated into a TEM instrument. These include selected-area electron diffraction (SAED) and electron dispersive spectroscopy (EDS). Copper TEM grids with lacy carbon were used for the aforementioned analysis.

Samples were prepared by depositing particles directly onto TEM grids with downstream of the plasma reactor by making a pass of the TEM grid under the reactor orifice with a pushrod. Samples were also prepared by transferring particles to TEM grids by abrasion of the collected powder with the TEM grid.

2.2.1.1 Selected Area Electron Diffraction

Selected Area Electron Diffraction (SAED) is a complementary technique often implemented with TEM instruments. SAED relies upon the particle-wave behavior of electrons; the wave behavior of electrons allows for a diffraction pattern to be observed as the electrons interact with the material. SAED analysis provides information about the crystal phases present in the imaging area during collection, and can be correlated with XRD patterns for cross-checking of results regarding crystallinity and/or material composition. Monocrystalline samples present with a periodic arrangement of bright spots in the pattern whereas polycrystalline samples produce rings due to the many crystals and their variable orientation.

2.2.1.2 Energy Dispersive X-Ray Spectroscopy

Energy dispersive X-Ray spectroscopy (EDS) is a technique that uses an electron beam to remove inner shell electrons. When higher shell electrons fill in the lower shell states X-rays of particular energy are emitted and can be used for elemental identification.

2.2.2 Scanning Electron Microscopy

Scanning electron microscopy (SEM) uses an electron beam that generates backscattered electrons, secondary electrons, and X-rays. Backscattered and secondary electrons are both used to generate SEM images. Samples for SEM were prepared by depositing particles onto flat substrates (wafers, glass slides). The samples were often coated with a thin layer of platinum to reduce charging and improve image quality. Samples were imaged on a Carl Zeiss Auriga Dual Column FIB SEM.

2.2.3 Optical Microscopy

Optical microscopy uses a combination of lenses and visible light to magnify images. A Keyence digital microscope was used to image samples.

2.3 Spectroscopy

2.3.1 Fourier Transform Infrared Spectroscopy

Fourier Transform Infrared Spectroscopy (FTIR) is a technique that can be used to probe the surfaces of materials. FTIR is used to observe the vibrational modes of chemical bonds originating at the interface between the surface of the sample and the environment (by contrast, Raman spectroscopy probes the internal vibrational modes, aka phonons). Depending on the chemical configurations at the surface of materials, infrared light will be absorbed as vibration modes are excited. For analysis of samples an Alpha DRIFTS Bruker spectrometer operated in refelctance mode was used to gather FTIR spectra. Samples were prepared by depositing samples directly from the reactor onto copper or stainless steel substrates.

2.3.2 Photoluminescence Spectroscopy

Photoluminescence (PL) is the phenomenon by which light is emitted from a material after the absorption of photons. When photons of sufficient energy are incident upon a semiconductor, electrons are promoted from the valence band to the conduction band of the material. The promoted electrons leave behind a hole in the valence band, when an electron relaxes back down to the valence band and then recombines with the hole, a photon is emitted. The emitted photons can then be monitored by a spectrometer and PL response can be measured.

Samples for PL were prepared with a number of methods. In the first samples were deposited directly onto a substrate and then illuminated with either a 325, 365, or 405 nm LED. Samples were also illuminated with a broadband deuterium lamp (200-1000 nm) with filters to select the appropriate portion of the spectrum for excitation, or with a 261 nm laser. Samples were also dispersed into hexane, ethanol, or toluene and the PL was then measured. PL was measured with either a Ocean Optics USB2000+ UV-VIS spectrometer or Ocean Optics USB2000+ VIS-NIR spectrometer.

2.3.3 X-Ray Photoelectron Spectroscopy

X-ray photoelectron spectroscopy (XPS) is used for elemental identification and chemical bonding present in a material. XPS relies upon the photoelectric effect and is described with the equation,

$$E_b = E_p - (E_k + \phi) \tag{2.4}$$

E_b is the binding energy, E_p is the incident photon energy, E_k is the kinetic energy of the emitted electron and ϕ is the corrected work function to take into consideration the contact potential of the instrument. X-ray photons result in electrons with some kinetic energy to be emitted which is measured by the instrument. With knowledge of the work function the binding energy can be calculated. The binding energy is used as the signature for the chemical species present in the material. The binding energy also responds to chemical shifts which allows for identification of different bonding in the material. XPS is a surface sensitive technique with a typical probe depth of

10 nm. Samples for XPS were prepared by depositing samples onto 1 cm by 1cm area of a copper substrate.

2.3.4 Electron Paramagnetic Resonance

Electron paramagnetic resonance (EPR) is a technique that utilizes the Zeeman effect. The Zeeman effect describes the splitting of degenerate spin energy levels of unpaired electrons. Electrons can exist in either a spin "up" or spin "down" state. In the absence of a magnetic field the spin up and down states have the same energy. When in the presence of a magnetic field these energy levels split. Under typical magnetic field strengths used in EPR these energy levels are split by energies on the order of microwaves. When unpaired electrons are present in a sample the absorption of the microwave energy can be measured and be related to the environment that the spin system is in. This information can be used to identify defects present in the material. The fundamental equation of EPR spectroscopy is,

$$h\nu = g\beta B \tag{2.5}$$

The left-hand side of equation is the energy of the incident microwaves where h is Planck's constant and ν is the frequency of the radiation used. On the right hand side, g is the proportionality factor used for the identification of the spin-system, β is the bohr-magneton constant.

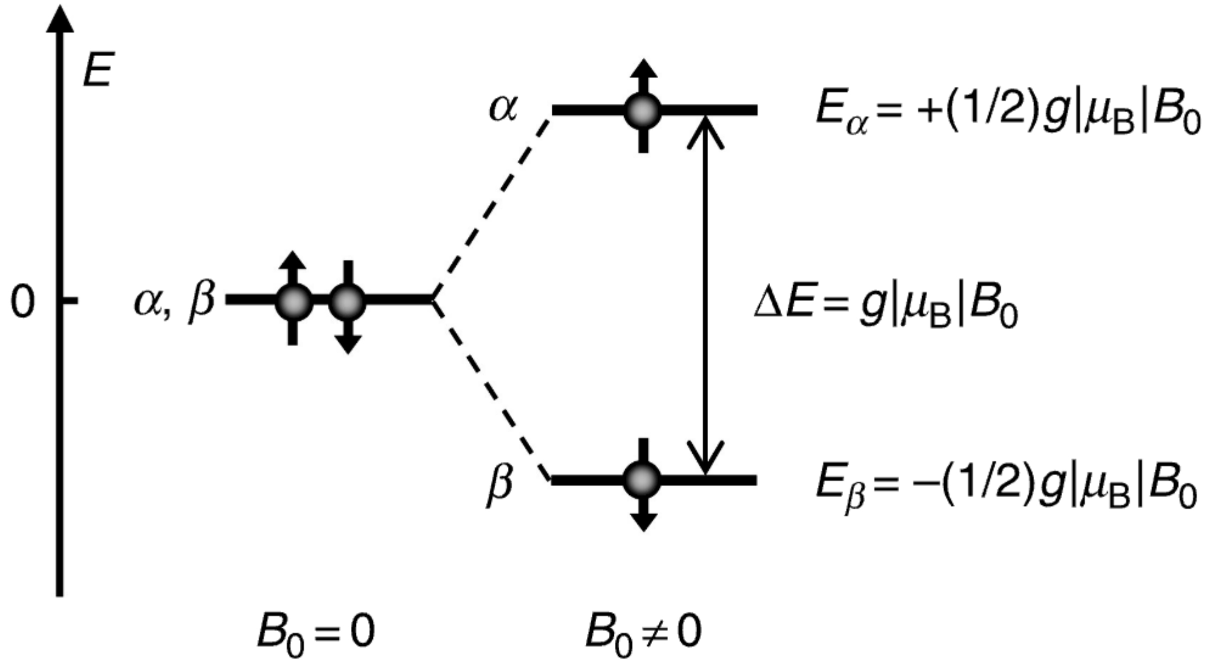

Figure 2.2: Energy diagram of electron spin states depicting energy level splitting with application of magnetic field.[2]

A Bruker ELEXSYS EPR insturment was used to collect spectra. Samples for EPR were prepared by transferring 3 to 4 mg of sample into a 4 mm EPR tube. Samples were then placed into the EPR microwave cavity where cavity was critically coupled to ensure all microwaves were absorbed in the cavity. Typical microwave frequency was 9.6 GHz and the magnetic had a maximum strength of 1.1 T. Samples were either collected at room temperature or at 4K, using liquid helium for the low-temperature experiments.

2.3.5 UV-VIS Absorption Spectroscopy

Absorption spectroscopy is used to measure the absorption of incident photons to a material. For semiconductors absorption scans can be used to estimate the bandgap of the material. From absorption data a Tauc plot can be generated to identify the bandgap. The Tauc relation is as follows,

$$(\alpha h\nu)^n = \beta(h\nu - E_g) \tag{2.6}$$

Here α is the absorption coefficient, hν is the incident photon energy, and n is constant based on the nature of the transitions (2 for direct transitions and 1/2 for indirect transitions). β is a proportionality constant and E$_g$ is the material bandgap. α is the related to the absorption (A) through the Beer-Lambert Law,

$$\alpha = \frac{1}{t} ln(T) \tag{2.7}$$

$$A = log_{10}(T) \tag{2.8}$$

Manipulation of the two equations yields the final form,

$$\alpha = \frac{2.303A}{t} \tag{2.9}$$

where t is the thickness of the sample or the path length of the cuevette. Often absorption data is collected at percent transmittance (%T) and is converted to absorbance with,

$$A = 2 - log_{10}(\%T) \tag{2.10}$$

A plot of $(\alpha h\nu)^n$ vs energy can then be made and the bandgap can be estimated by fitting a line to the linear portion of the plot and inspecting where the line intersects the abscissa. The method also assumes scattering, refractive, and reflection effects to be negligible. If such phenomena are present error will be introduced. Also note that the absorbance (A) is a log scale value and should not be confused with the absorbtance also commonly defined as "A" and typically defined as,

$$A = 1 - T - R \tag{2.11}$$

where T is the transmittance and R is the reflectance. Here A, T, and R represent the flux of each quantity normalized to the incident flux of photons to the surface.

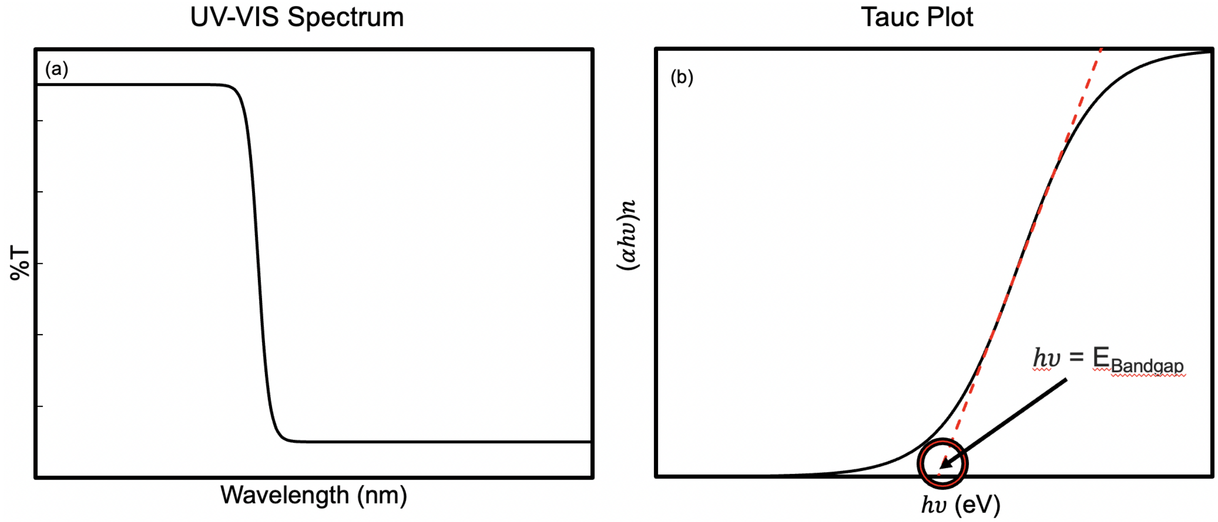

Figure 2.3: (a) Simulated absorption spectrum. (b) Resulting Tauc plot after conversion of data to absorption and then $(\alpha h\nu)^n$

CHAPTER 3

LOW-PRESSURE SYNTHESIS OF GaN, InN, AND $In_XGa_{1-X}N$ NANOPARTICLES

3.1 Introduction

Among the III-nitrides, Gallium Nitride (GaN) has been the focus of many researchers due to its suitable properties for applications that require high thermal and mechanical stability, high frequency, and wide direct bandgap of 3.4 eV. Notably the 2014 Nobel prize was awarded to I. Akasaki, H. Amano and S. Nakamura for their work to produce efficient blue LEDs based with GaN which has enabled production of white light LEDs.[33] GaN has also found use in UV lasers, LEDs, photodetectors, and photocatalysis.[34–36] Indium nitride (InN) does not posses the same level of thermal and mechanical stability as GaN but it is still suitable for solar cells,[37,38] sensors,[39] and many biological applications[40] due to its low toxicity and small bandgap of 0.7 eV.[41] The similar crystal structures of GaN and InN allow for the binary alloy of Indium Gallium nitride ($In_xGa_{1-x}N$) to be formed with a bandgap that spans from 0.7 eV to 3.4 eV, depending on the stoichiometry of the alloy. This wide range of possible bandgaps opens the applications space of $In_xGa_{1-x}N$ to span from the infrared to the UV range making its use in optoelectronics attractive.

Many methods have been explored for the synthesis of these nitride materials. Well-known techniques such as chemical vapor deposition (CVD),[42] atomic layer deposition (ALD), and metal organic chemical vapor deposition (MOCVD)[43] have all been used to synthesize thin films of the III-nitrides in the gas phase.[44] In the area of plasma synthesis there are few reports for synthesis of InN, GaN, and $In_xGa_{1-x}N$ nanoparticles. Anthony *et al*[45] have shown the use of a nonthermal plasma reactor with a metal organic precursor and ammonia the synthesis of GaN. Similarly, Uner *et al*[46,47] have also demonstrated synthesis of GaN and InN using a solid metal source and molecular nitrogen. Shimada *et al*[48] demonstrated the use of a microwave plasma for the synthesis of GaN. InN and $In_xGa_{1-x}N$ nanoparticle synthesis in the gas-phase has been far less studied in comparison to GaN many of the reports focus on liquid based methods but early success was limited by the

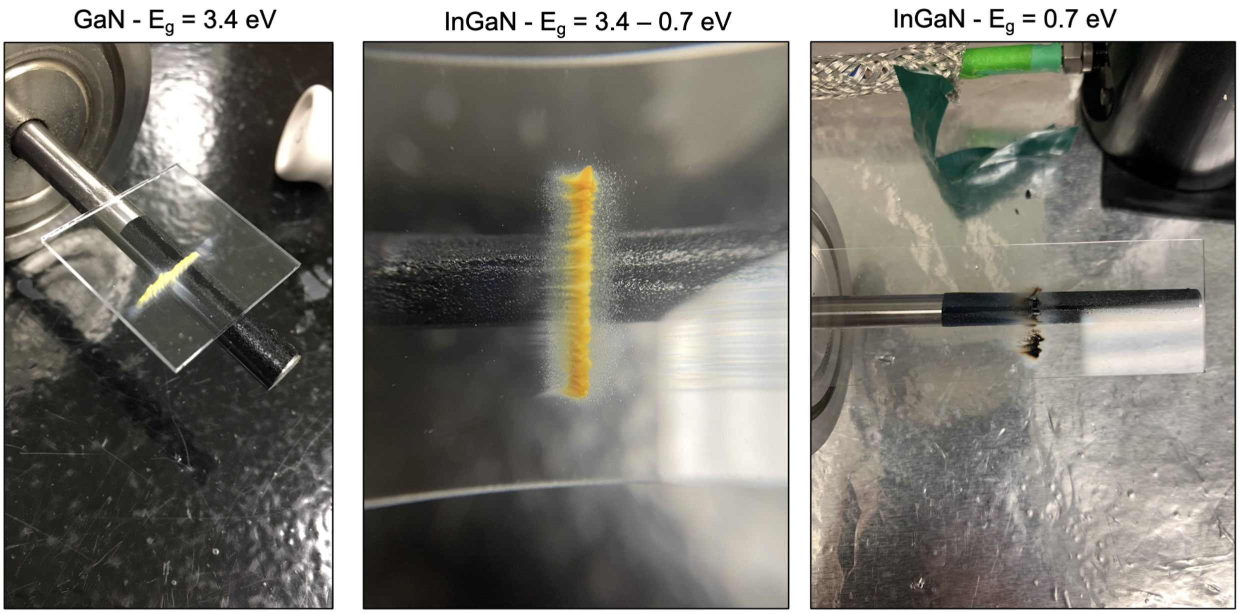

Figure 3.1: Comparison of GaN, $In_xGa_{1-x}N$, and InN nanoparticles.

developing nature of the synthesis methods.[49] In the liquid phase, successful demonstrations of $In_xGa_{1-x}N$ nanoparticle synthesis[50] have been made but to the best of my knowledge there exists no reports of nanoparticle synthesis of $In_xGa_{1-x}N$ in the gas phase. In this chapter an all-gas-phase approach for the synthesis of GaN, InN, and $In_xGa_{1-x}N$ is presented. A description of the reactor used for synthesis for each material is provided followed by a discussion of the nanoparticle characteristics and properties.

3.2 Experimental Methods

3.2.1 Low-Pressure Plasma Reactor

Gallium nitride nanoparticles were synthesized with a nonthermal plasma reactor. The reactor is composed of two basic elements: a quartz tube and cylindrical electrodes placed around the tube. Multiple configurations of electrodes and tube sizes were used to modulate synthesis parameters. The relevant geometry and arrangements are noted when specific experiments are addressed. In general the inner diameter of the tube varied from 3.5 to 10.5 mm, and a two or three electrode configuration was used to vary plasma length from 63 to 145 mm. Between the electrodes a plasma was ignited through the use of a handheld Tesla coil, 13.56 MHz RF power generator, and an impedance matching network. The power generator served as the power source for the plasma and since there exists an impedance mismatch between the generator and the plasma, a matching network was used to match the impedance of the generator to the plasma. This impedance matching reduces unwanted dissipation of power between the power source and load (plasma reactor). A Tesla coil was used when the plasma was not readily ignited by the RF generator alone; when this occurred the coil would be turned on and held in close proximity to the reactor to increase the strength of the electric field between the electrodes and ignite the plasma.

Flown to the reactor was a mixture of precursor and background gases. The precursor gases were trimethylgallium (TMG), trimethylindium (TMI) and ammonia (NH_3) serving as the sources for gallium, indium, and nitrogen respectively. Argon was flown to the reactor as an inert background gas to aid in both sustaining the plasma and to provide an additional parameter to affect synthesis conditions. At ambient conditions TMI is a solid and does not exhibit the necessary vapor pressure to provide reliable flow unless heated. Thus when synthesizing particles with indium content electrical heaters were used to keep the TMI source and process lines surface at a temperature of 80 degrees Celsius to ensure sufficient flow of vapor and avoid condensation of the precursor. To control flow of the TMI a heated MKS 1152C mass flow controller (MFC) was used. All other gases were left at room temperature and each flow was regulated with typical MFCs from MKS.

The reactor was operated at pressures in the range of 3 to 10 Torr as measured by a MKS 626 Baratron gauge just upstream of the reactor. Operation at low pressure was selected based upon previous reports of nanoparticle synthesis at low pressure and benefits such as reduced breakdown voltage for plasma discharge, greater nanoparticle charge accumulation aiding in agglomeration suppression, reduced ion densities for particle crystallization, etc.[51] Prior to synthesis the reactor was purged with argon to reduce concentration of any gas species not desired during synthesis; a typical purge cycle was performed three times before introducing process gases.

To collect samples during deposition two methods were employed. Both methods rely upon inertial impaction of the nanoparticles onto substrates. Downstream of the reactor an orifice is

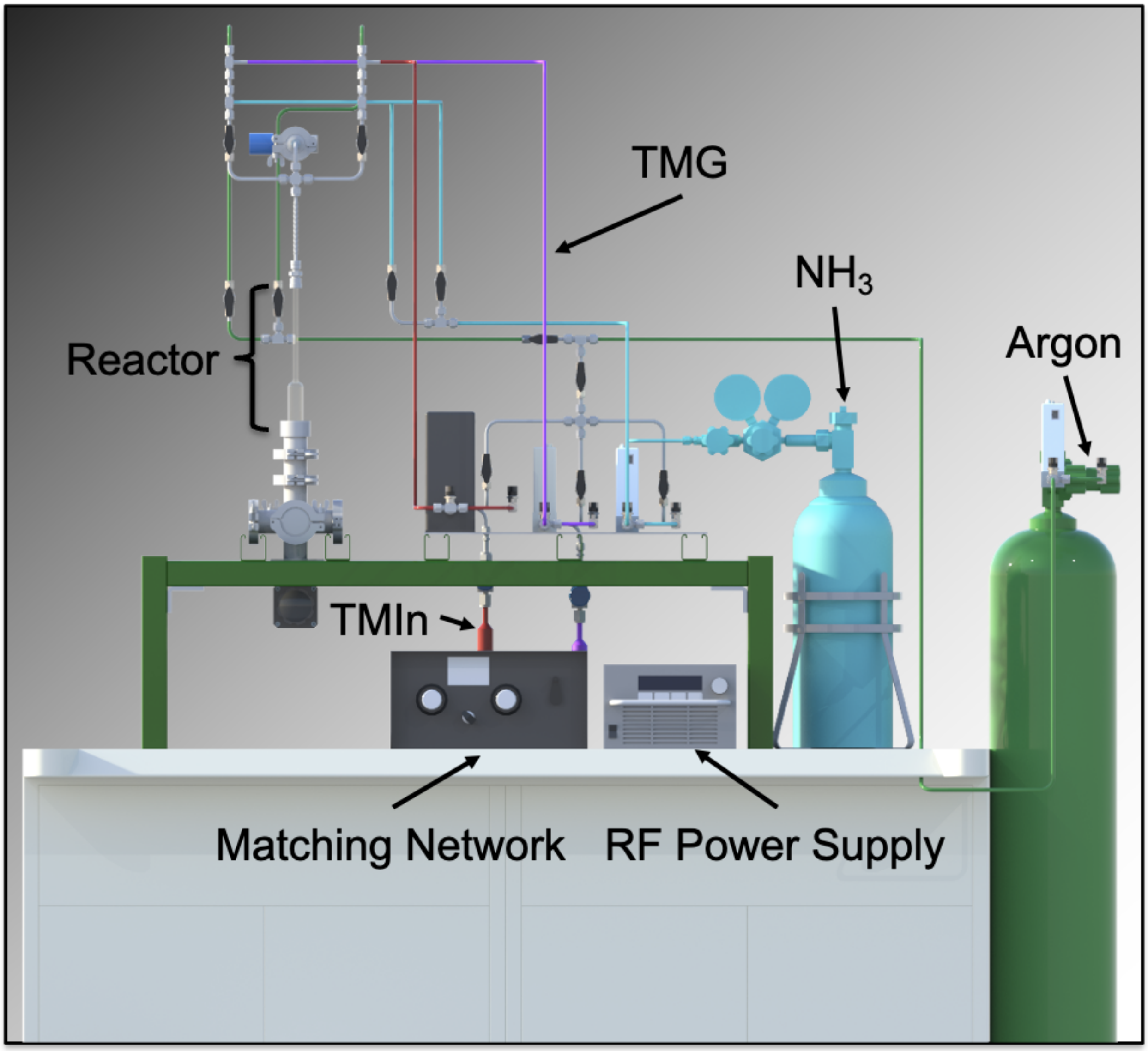

Figure 3.2: Rendering of experimental setup used to synthesize nitride materials. Not shown here are two heaters used to heat TMI lines to reduce risk of condensation of TMI in the process

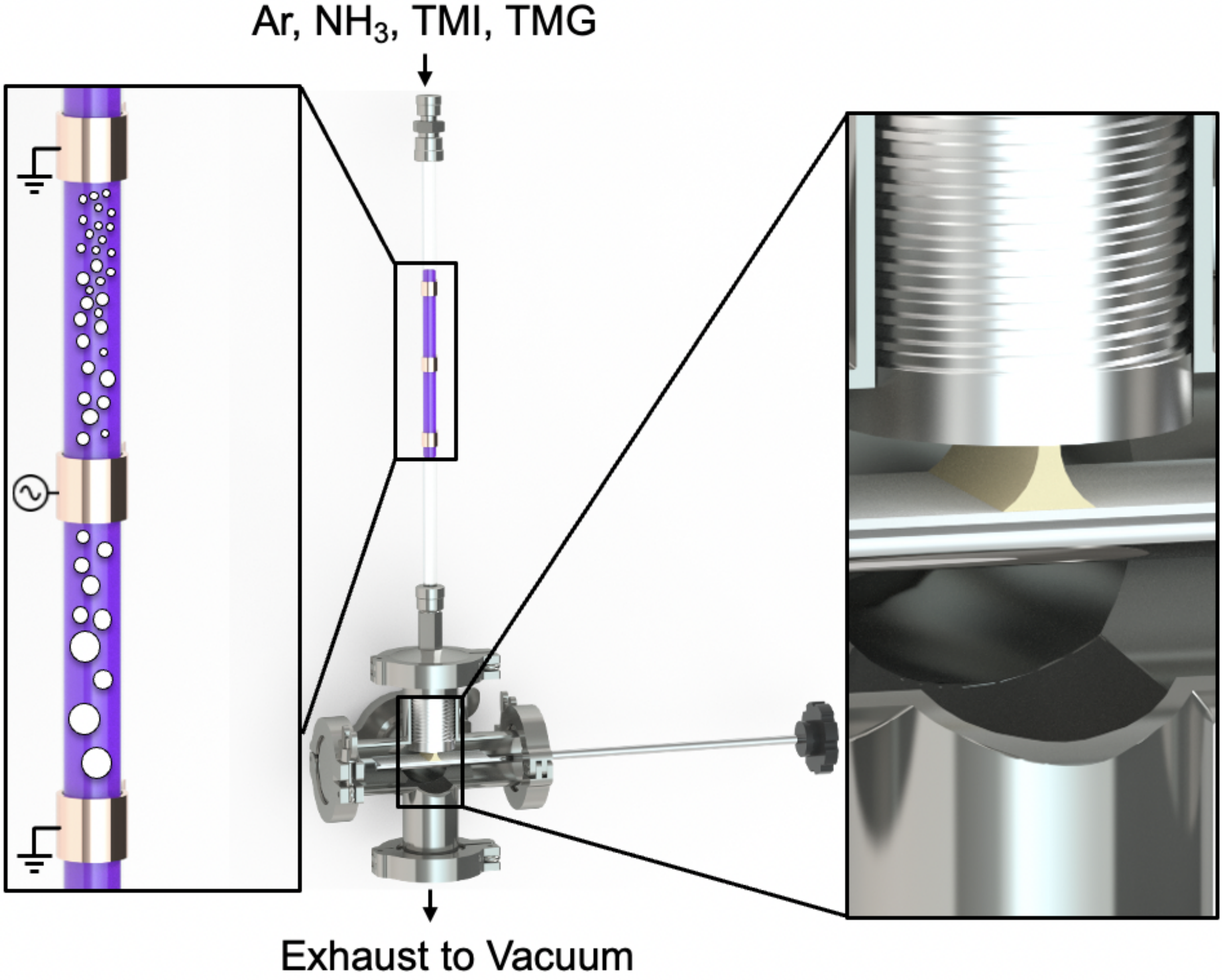

Figure 3.3: Typical reactor configuration used for synthesis of nitride materials. Background and precursor gases enter from the top of the reactor, enter the reaction zone where particles are synthesized, particles are then carried by the gas flow and collected on substrates beneath the orifice.

placed that results in choked flow. As the jet expands after the orifice particles and the flow are accelerated to supersonic speeds until the mach disk is reached at which point he flow field experiences a near instantaneous decrease in velocity while particles maintain a high velocity this results in highly efficient impaction of particles onto the substrate.[52] Substrates were either mounted on a push-rod or in-line to an o-ring downstream of the orifice. Following synthesis the substrates were removed and the samples were then analyzed.

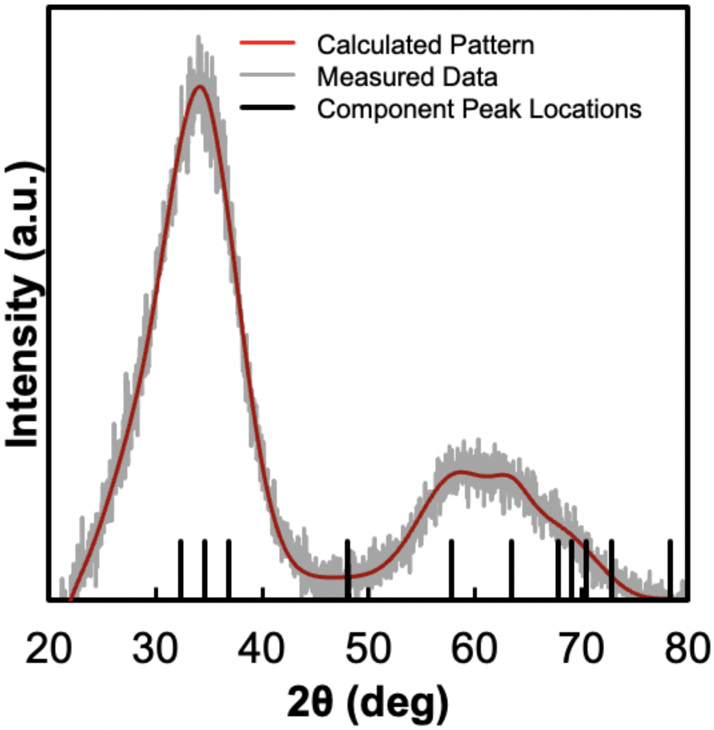

Figure 3.4: Diffraction pattern obtained for particles synthesized with residence time of 51 ms. Long tick marks denote the central locations of peaks obtained from Rietveld refinement of diffraction pattern.

3.3 Results and Discussion

3.3.1 Gallium Nitride Nanoparticle Synthesis

3.3.1.1 Size and Crystallinty Analysis

GaN may crystallize in either a wurtzite (hexagonal), zinc-blende (cubic), or rock salt phase. The wurtzite structure is the stable phase at ambient conditions, the zinc-blende phase is metastable at ambient conditions and often requires a cubic substrate to initiate growth,[53, 54] and the rock-salt phase forms only under conditions of extreme pressure and temperature. To identify the crystal phase present in the synthesized GaN nanoparticles, XRD and TEM were used. For the XRD analysis Rietveld refinement was used to recreate the measured diffraction pattern. It is often assumed that the gas temperature is in equilibrium with the gas rotational temperature but often the conditions for this assumption to hold are not met in nonthermal plasmas.[56] This is further evidenced by zinc-blende phases forming in nonthermal plasmas despite the phase being less thermodynamically likely at ambient conditions.[57] For this reason iterations of the Rietveld refinement were performed for both the wurtzite and zinc-blende phases. The refinement yielded the closest agreement to the experimental data when the hexagonal phase was used. The refinement also yielded an ellipsoidal particle shape with characteristic radii of 1.7, 1.7 and 2.9 nm. TEM was used to support the findings of the XRD by measurement of lattice spacing using image processing software (ImageJ)from the TEM images. The measurements provided a spacing of 2.38±0.5 angstroms, corresponding with the <1010> family of planes.

XRD and TEM were also used to establish the threshold for the production of crystalline particles. It has been shown that the heating of nanoparticles and their resulting temperature is dependent upon the power supplied to the plasma.[51] Consistent with the previous report there is a power threshold at which particle crystallization is observed. At the low power condition of 130 W there was no clear presence of lattice fringes in the TEM nor was there signal present in the diffraction patterns. When power was increased to 150 W presence of lattice fringes in the TEM was present and peaks in the diffraction pattern were observed both of which are indicative of crystalline material. At higher power of 175 W there is a return to the amorphous structure which may be explained by competing growth and breakdown of particles at high power densities.

It has been established that nanoparticle size is dependent upon the particle residence time. The residence time is defined as the amount of time that a particle is present in the plasma volume. The equation for residence time is derived from the ideal gas law and takes the following form,

$$\tau = \frac{P_2}{P_1}\frac{T_1}{T_2}\frac{V}{Q} \tag{3.1}$$

Here τ is the residence time, P is pressure, T is temperature, V is plasma volume in cubic cm, and Q is the flow rate in sccm. The subscript 1 refers to the standard or reference conditions for which the MFC was calibrated, and the subscript 2 refers to the process conditions when the particles were synthesized. For the data presented here the residence time was shifted by changing the argon flow rate. To estimate the particle diameter TEM images were inspected and particles were identified. Traces of the particle boundaries were made and then the area was calculated

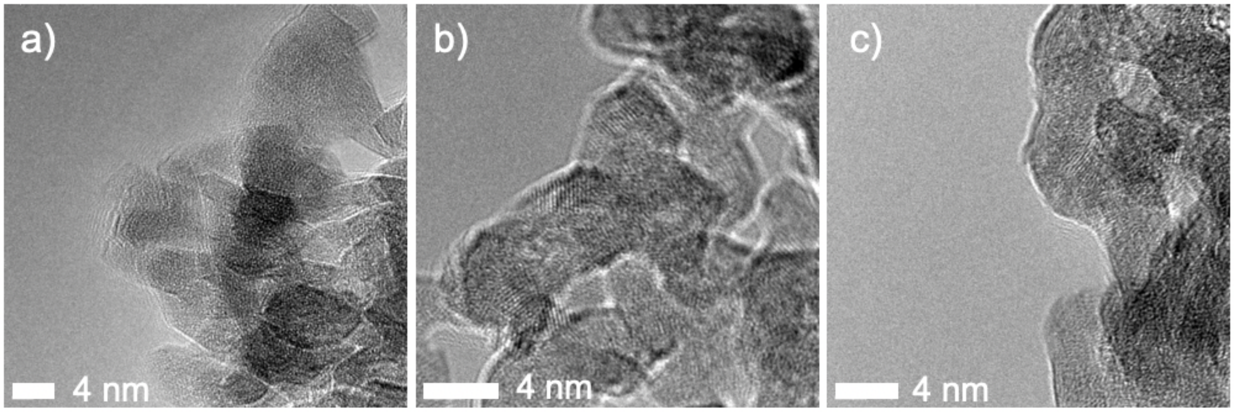

Figure 3.5: Representative TEM images of GaN nanoparticles synthesized at different powers. (a) Particles synthesized at 130 W. (b) Particles synthesized at 150 W. (c) Particles synthesized at 175 W.

numerically, a effective diameter was then calculated by making the simplification that the particles were spherical. The analysis shows that the size is normally distributed and that the particle size deceases with deceasing residence time. This analysis method introduces error through user bias and assumption of particle shape which means that the calculated value of the particle diameter should no be taken to represent the actual diameter but rather should be used as an indicator that the particle size trends in the appropriate direction.

Considering the overall size of the particles which are fairly small, the size distribution is narrow with an average coefficient of variation (division of standard deviation by the mean) equal to 0.23. The width of the size distribution is comparable to other synthesis methods of particles near this size.[46,58,59] The XRD analysis presented earlier was for samples synthesized at a residence time of 51 ms. Comparison of the characteristic radii found from Rietveld refinement to the characteristic diameter calculated from the TEM analysis yields values of 4.2 and 3.2 nm respectively. Considering the ambiguity introduced from the overlap of the component peaks that compose the diffraction pattern and the error in the TEM image analysis, these values are within reasonable proximity to each other.

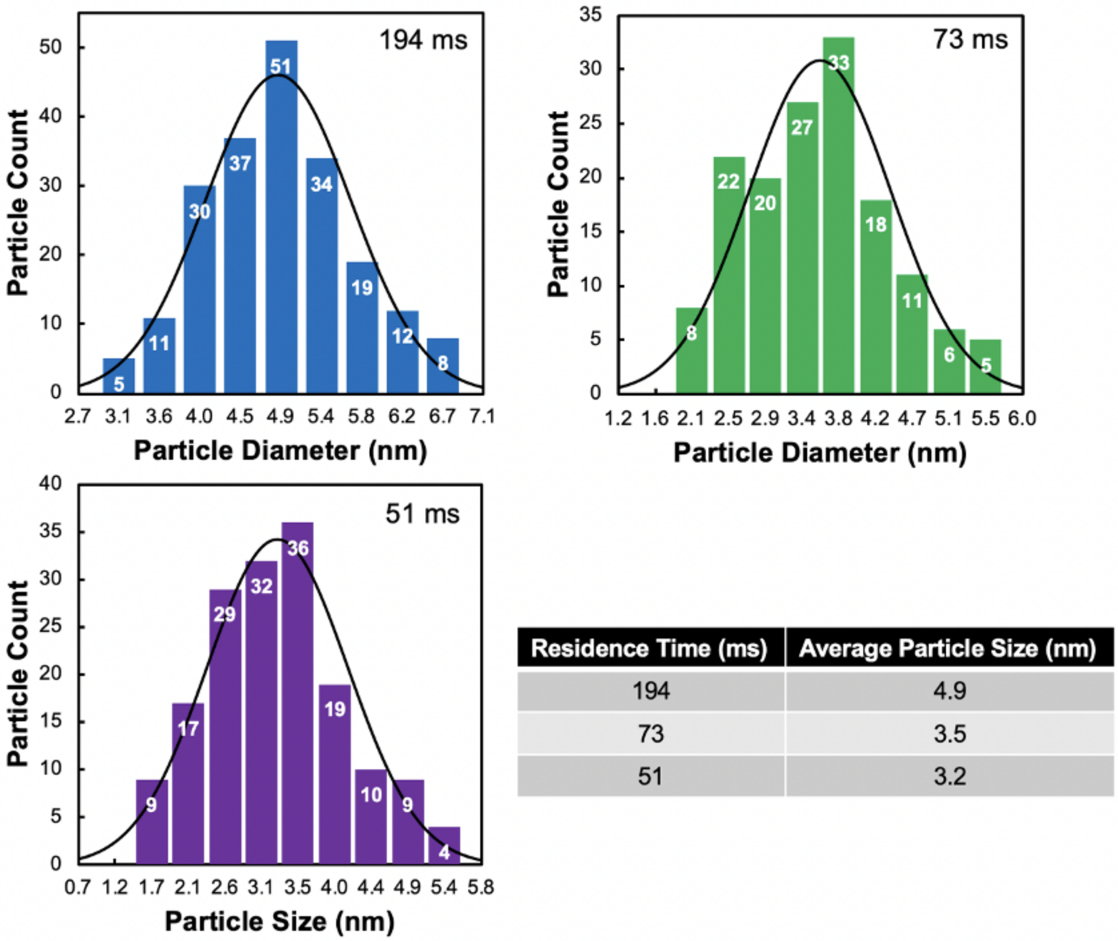

Residence Time (ms)	Average Particle Size (nm)
194	4.9
73	3.5
51	3.2

Figure 3.6: Nanoparticle size distributions synthesized at different residence times. Black curves are normal distribution overlays. Number at the top of each bin denotes the number of particles counted in each bin

3.3.1.2 Composition and Surface Analysis

To gain insight to the chemistry of the particles XPS was used to identify the bonding present in the nanoparticles as well as the relative ratios of constituent atoms. The XPS spectra indicated the presence of gallium, nitrogen, carbon, oxygen, and hydrogen. In the Ga 2p3/2 peak there is a large contribution from Ga-N bonding as well as smaller contributions from metallic Ga-Ga and Ga-O. The Ga-O bonding likely occurred due to air exposure between synthesis and measurement with dangling bonds at the particle surface or through possible back-bonding. In the C1s peak the presence of C-C bonding may be attributed the adventitious carbon layer that forms on most materials following air exposure, it is also possible that short carbon chain molecules bonded to the

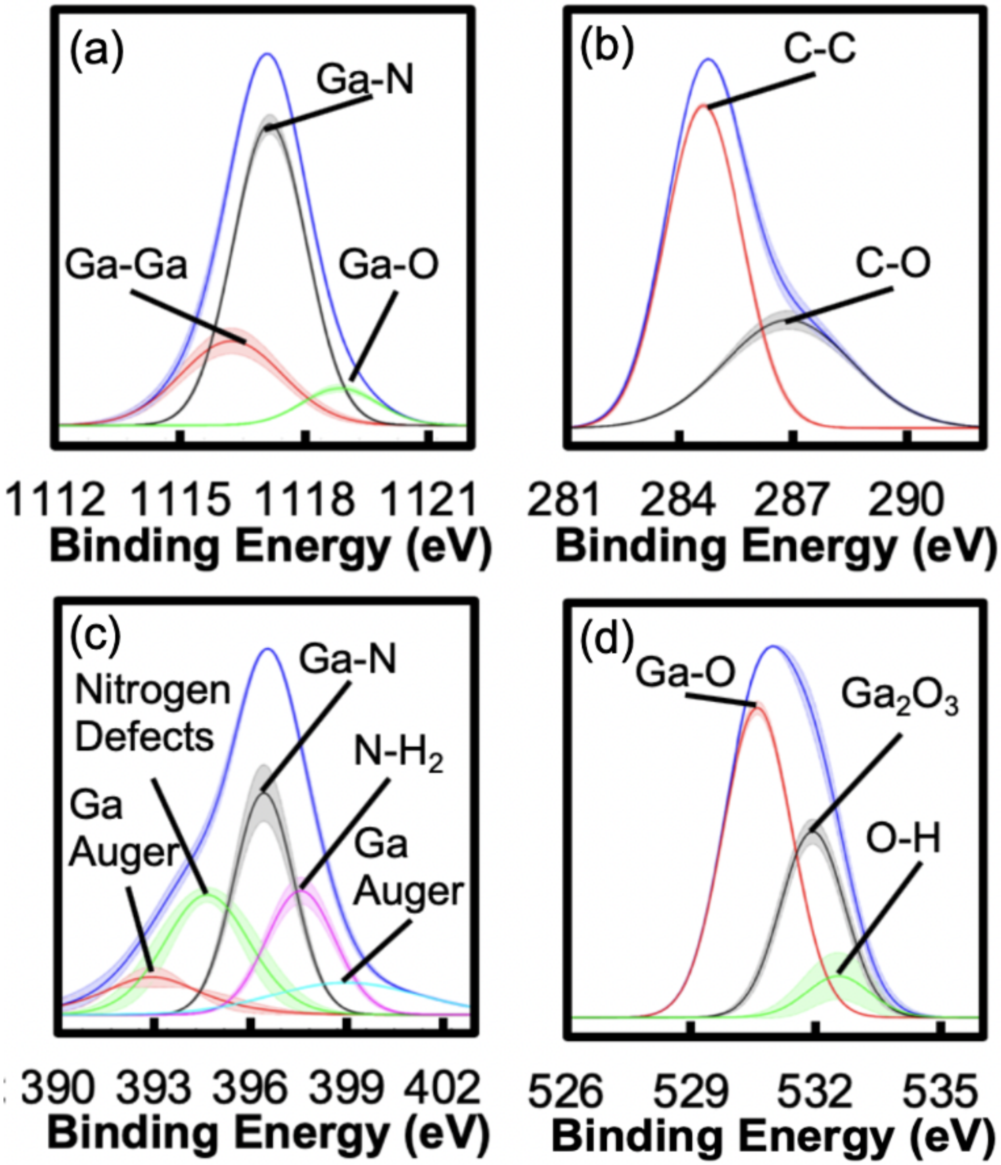

Figure 3.7: XPS spectra of the (a) Ga 2p3/2, (b) C 1s, (c) N 1s, and (d) O 1s peaks. Each peak is an average of three samples with the standard deviation denoted by the shaded region

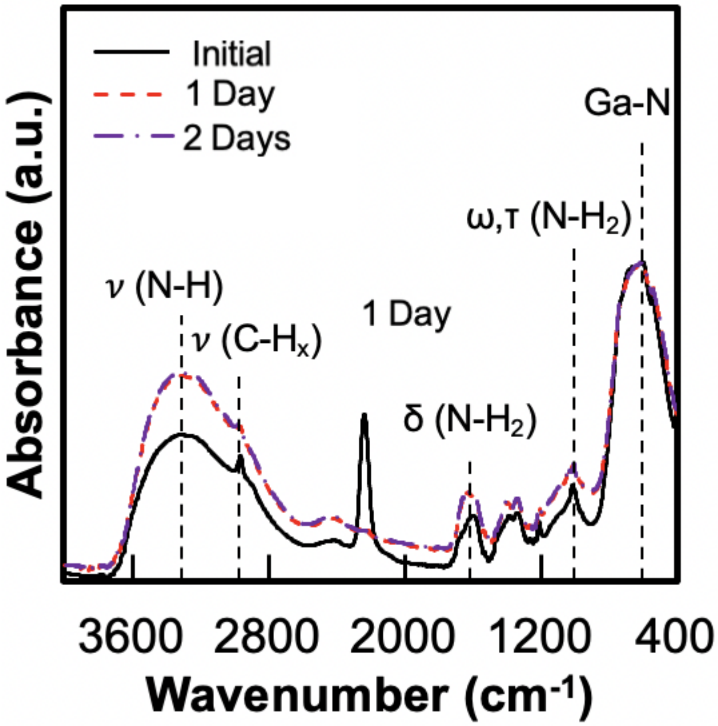

Figure 3.8: FTIR spectra of GaN nanoparticles that displays change in particle surface with time.

particle surface during synthesis, there also exists the potential for contamination from aerosolized pump oil reaching the reactor.[60] The air exposure can be extended to explain the C-O bonding since oxidation of the carbon species could concomitantly occurred with the formation of the carbon layer. The N1s peak has contributions from Ga-N, N-H_2, Ga Auger, and potential nitrogen defects.[61] The O1s peak shows the presence of various gallium oxide species which again likely formed due to air exposure. Overall elemental analysis yielded a 1:3 ratio of gallium to nitrogen. This ratio is contraindicated by the presence of Ga-Ga bonding but it is possible that there is larger presence of nitrogen at the surface of the particles than in the core of the particle. XPS is a surface sensitive technique with a probe depth of roughly 5 to 10 nm further the intensity decays exponentially with depth thus the surface plays the most significant role in the signal intensity.[62]

FITR was used to probe the surface chemistry of the nanoparticles. Scans were taken immediately after synthesis and multiple days following synthesis. Approximately 10 minutes of air exposure occurred between synthesis and the collection of the initial spectrum as this was the time required to transfer the sample from the reactor to the FTIR instrument.

In the wavenumber range from 400-850 cm^{-1} exists a multitude of vibrations that may be attributed to different vibration modes of either Ga-N and Ga-O.[63,64] Direct assignment of vibration modes without ambiguity is complicated by the convolution of the peaks. The representative fitting of the FTIR spectrum shows that the experimental data agrees well with the expected peak positions of Ga-N and Ga-O. From 800-1600 cm^{-1} there exists many possibilities for the vibrational modes present as bonding between gallium carbon, nitrogen, oxygen, and hydrogen all produce signatures in this range.[65,66] Likely groups to form at the particle surface are N-H, N-H_2, C-H, C-H_2, and due to the air exposure, oxygen containing variations of theses groups could form.

The sharp feature near 2100 cm^{-1} is short lived and diminishes greatly 1 day after synthesis. We have assigned this to feature to be a combination of molecular nitrogen complexed with gallium and gallium azide both of which have been shown to form on GaN films when a metal organic precursor and ammonia is used.[65,67]

In the wavenumber range from 2800-3600 cm^{-1} there exists overlap between the O-H and N-H stretching vibrations. Also in this region are C-H bending modes corresponding to the alkane, alkene, or alkyne species at the surface.[66] The FTIR spectra differ modestly as time progresses. The most notable changes are the decrease in absorbance at 2100 cm^{-1} and the growth of the N-H and O-H in the 2800 to 3600 cm^{-1} range. This implies that the majority of oxidation occurred rapidly following deposition. Increases in absorption from O-H would result in increased absorbance in both the 2800-3600 cm^{-1} and 1000-1500 cm^{-1} range. This increase may result from the combined effects of oxidation and water adsorption.[68] Figures 3.9,3.10, and 3.11 show sections of a representative FTIR spectrum from as-produced GaN nanoparticles in selected spectral ranges, together with bonding assignments based on deconvolution of the spectrum.

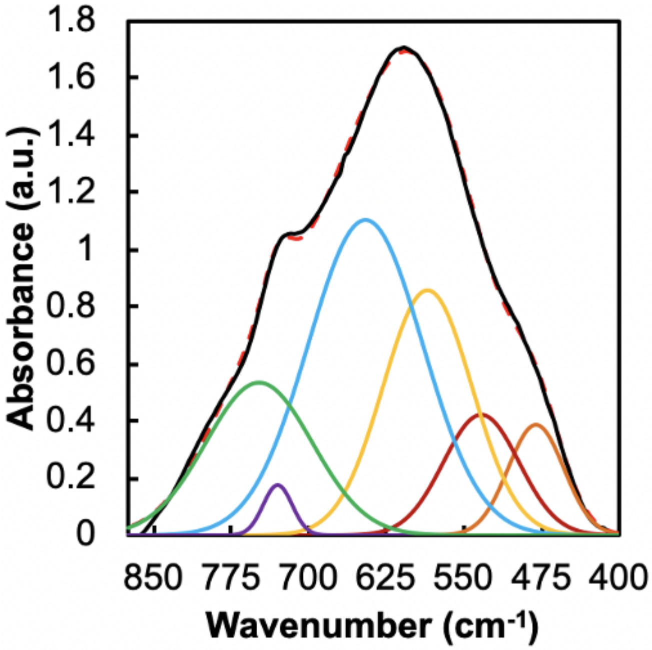

GROUP	Wavenumber (cm^{-1})
Ga-O	480
Ga-N	553
Ga-N	567
Ga-O	645
Ga-N	730
Ga-N	748

Figure 3.9: Reduced range of FTIR spectrum from 400-850 cm^{-1} where deconvolution of the spectrum has yielded component peaks corresponding to a variety of vibrational modes at the particle surface.

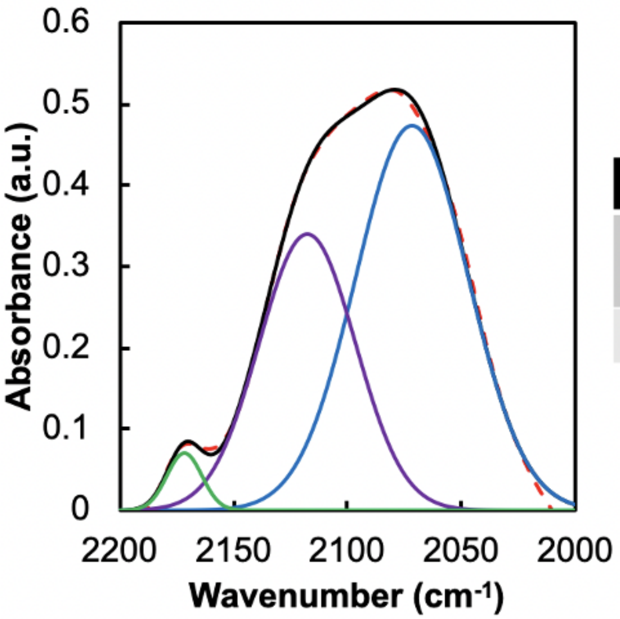

GROUP	Wavenumber (cm^{-1})
N_2 complexed with Ga	2118
$N^-=N^+=N^-$	2072

Figure 3.10: Reduced range of FTIR spectrum from 2000-2200 cm^{-1}where deconvolution of the spectrum has yielded component peaks corresponding to a variety of vibrational modes at the particle surface.

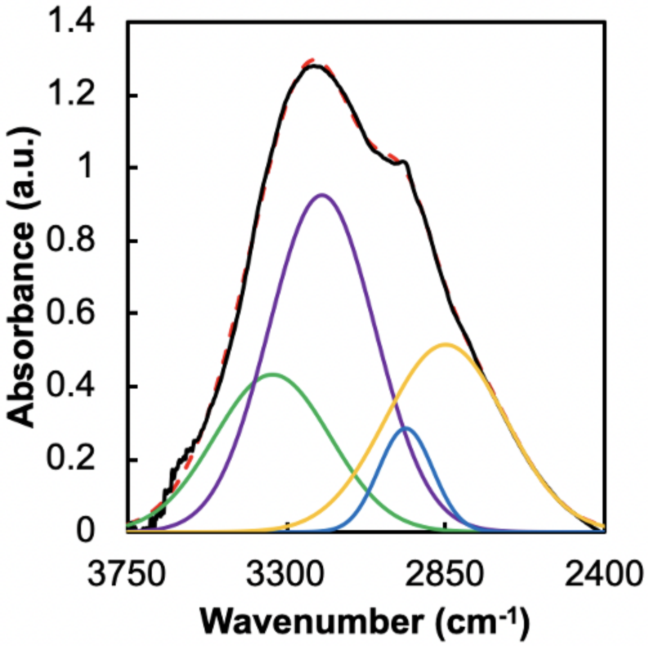

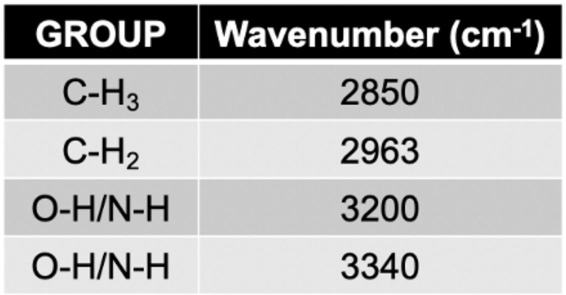

GROUP	Wavenumber (cm^{-1})
C-H_3	2850
C-H_2	2963
O-H/N-H	3200
O-H/N-H	3340

Figure 3.11: Reduced range of FTIR spectrum from 2400-3750 cm^{-1}where deconvolution of spectrum has yielded component peaks corresponding to a variety of vibrational modes at the particle surface.

3.3.1.3 Optical Properties and Defect Characterization

UV-VIS spectroscopy was used to gain insight into the optical properties of the GaN nanoparticles synthesized with a residence time of 51 ms. Onset of absorption began near 500 nm and increased as the wavelength decreased. Estimation of the bandgap was made from conversion of the absorption data to the Tauc plot. The bandgap was then be evaluated by fitting a tangent line to the linear portion of the plot and inspecting where the tangent intersects the abscissa. This analysis yielded a band gap of 5.4 eV which represents a blue shift of 2 eV from the bulk bandgap of GaN. A shift of the bandgap to higher energy is expected if the material is quantum confined, with a material-specific dependence of bandgap widening on nanoparticle dimension. Within in the literature there is disagreement on the Bohr-exciton radius which is the dimension used to describe the onset of quantum confinement. Values of the Bohr-exciton radius range from 3 to 10 nm.[54, 60, 69] Particles synthesized at a residence time of 51 ms have an average diameter of 3.2 nm. Based upon reports by other groups it is not unreasonable to see a shift to higher energies at this particle size.[54, 70, 71]

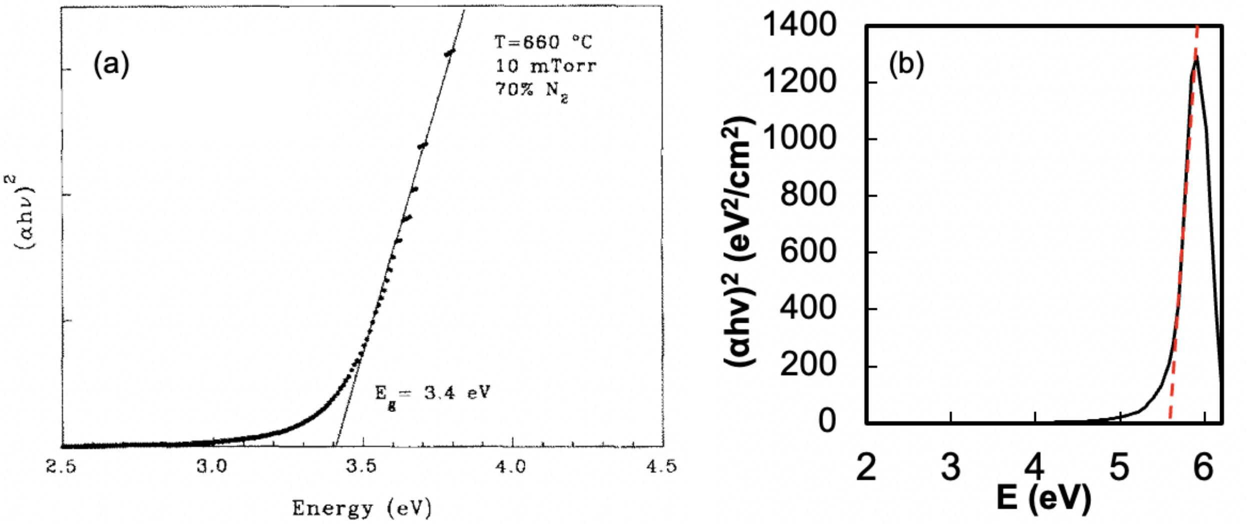

Figure 3.12: (a)Tauc plot of bulk GaN.[3] (b)Tauc plot with fitted line to linear portion of the plot. Intersection of dashed red line with the absiccca corresponds to the estimated bandgap.

Many attempts were made to synthesize luminescent GaN with limited success. A single case of luminescent material was made after dispersion of particles into oleylamine. The PL was centered near 365 nm which is representative of band-edge emission in non-quantum confined particles. The single case of luminescence at 365 nm and the general lack of luminescence otherwise indicates that non-radiative recombination is the predominant relaxation mechanism. Because of the large surface area to volume ratio the particle surface plays an integral role in the luminescence of nanoparticles. There can exist a large number of defects at the particle surface that may quench luminescence.[72] Within the GaN crystal there also exists an internal electric field which results in prolonged lifetime of charge carriers providing greater opportunity for these carriers to interact with a defect present in the particle leading to decreased luminescence. From the XPS analysis there exists a non-stoichiometric ratio of gallium to nitrogen which would indicate the possibility for vacancy sites in the lattice, nitrogen vacancies have been shown to act as non-radiative recombination centers GaN.[72] To further probe the defect states room temperature EPR of GaN samples were performed. A single feature was identified in the EPR spectra at a g-value of 2.008 this value is slightly shifted from the free electron g-value of 2.0023 and is commonly associated with both nitrogen and gallium vacancies. This result supports the claim that there is a non-stoichiometric ratio of gallium to nitrogen present which may be a contributing factor to the lack of luminescence.

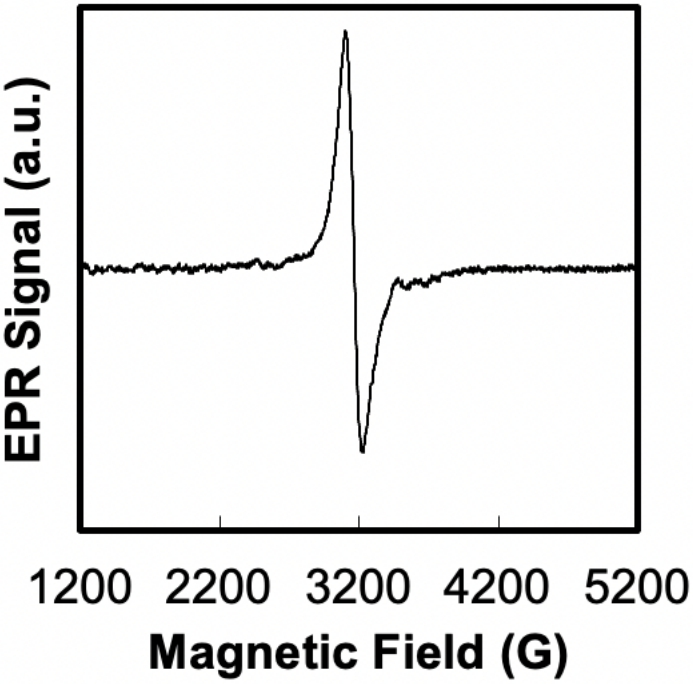

Figure 3.13: Representative EPR spectrum of GaN nanoparticles.

3.3.2 Indium Nitride Nanoparticle Synthesis

3.3.2.1 Size and Crystallinty Analysis

Similar to GaN, InN may crystallize in a wurtzite, zinc-blende, or rock salt structure. The wurtzite structure is the stable phase at ambient conditions. A combination of XRD, SAED, and TEM were used to examine the structure of particles synthesized at 50 W. Deconvolution of the XRD pattern and fitting to a hexagonal structure yielded the highest agreement between the measured diffraction pattern and calculated diffraction pattern. Similar to the XRD pattern the SAED pattern shows wide rings at two locations. The SAED image was mapped into the 2ϑ space by measuring the radial intensity of the rings and making the appropriate conversion from reciprocal space to 2ϑ space. This analysis yielded a pattern that closely agrees with that of the XRD pattern. TEM was used to further verify the presence of the wurtzite structure. Measurement of lattice spacing in TEM images yielded a spacing of 2.7 angstroms consistent with the spacing of the (101) direction in the wurtzite crystal. TEM was also used to estimate the particle size using the method described

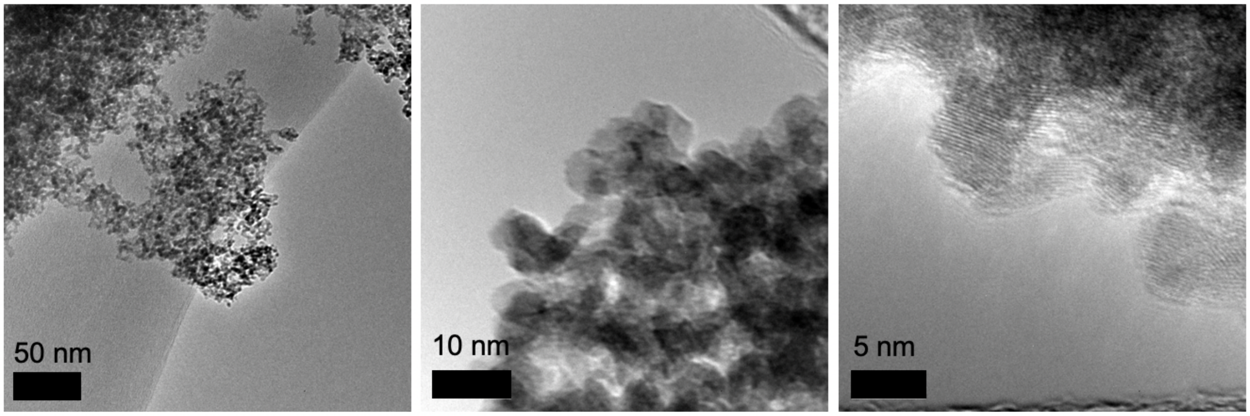

Figure 3.14: TEM images of InN nanoparticles at different magnifications.

previously in the GaN section. This analysis yield an average diameter of 6.7±1.7 nm for particles synthesized with a residence time of 51 ms.

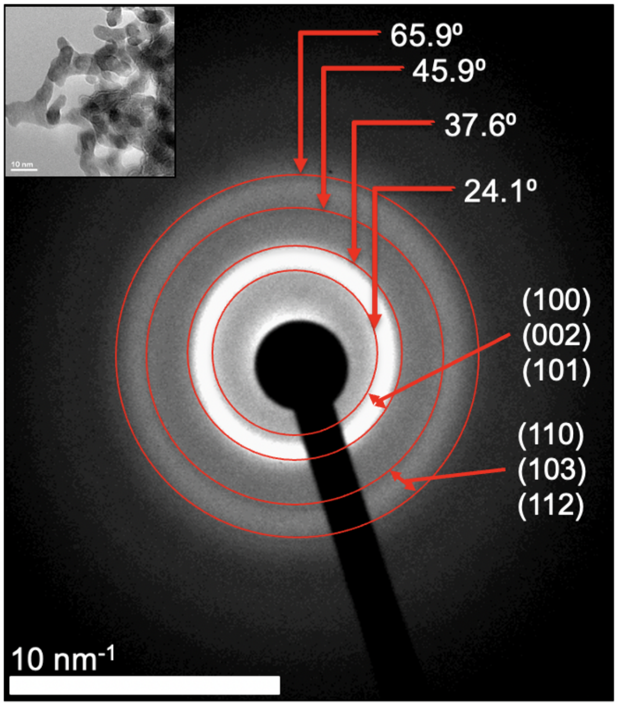

Figure 3.15: SAED pattern of InN nanoparticles. With equivalent 2ϑ values denoted at the extrema of the rings.

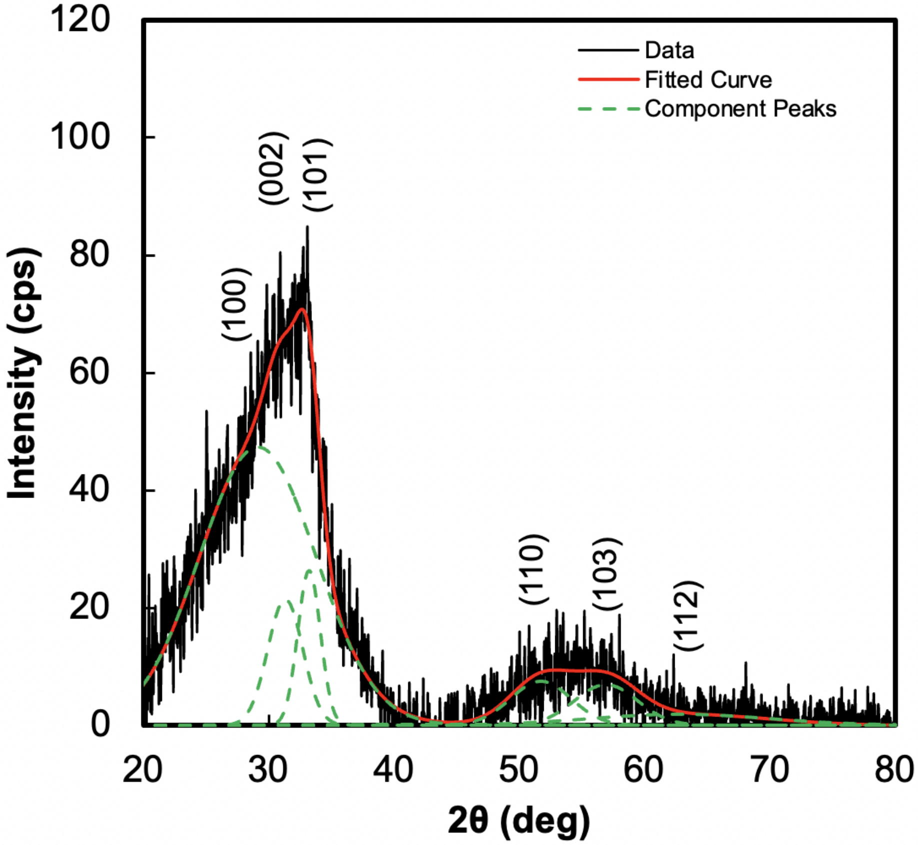

Figure 3.16: XRD pattern fitted to hexagonal InN. Diffraction pattern is a convolution of the component peaks.

3.3.2.2 Composition and Surface Analysis

FTIR was used to examine the vibrational modes that were present at the particle's surface. Measurements were taken immediately after synthesis and at 24 hour intervals following synthesis. Approximately 10 minutes of air exposure occurred between synthesis and initial measurement. The FTIR spectra of InN nanoparticles revealed a surface with predominantly features related to complexes of In with N, O, H, and combinations of the three, similar to the GaN nanoparticles. In the wavenumber range from 400-650 cm^{-1} there exists a multitude of vibrations that may be attributed to either In-N and In-O. Possible vibrations include the In-N stretching mode at 510 cm^{-1} and the InN phonon mode at 486 cm^{-1}.[73,74] Further In-O has a vibration that presents at 565 cm^{-1} with phonon modes at 429 and 600 cm^{-1}.[75]

In the wavenumber range from 750-1150 cm^{-1} there exists many vibrations that can be attributed to InN. These include In-N stretch at 824, 902, 972, 1112, and 1164cm^{-1}.[76–78] A In=N vibration at 968 cm^{-1} is also possible.[76] Shifts from these positions could also occur if there exist various InN_xO_y species. In the wavenumber range from 1250-1750 cm^{-1} possible attributions include In-NO_3 at 1380 cm^{-1}, broad bending modes of In-OH occur in the vicinity of 1400 and 1600 cm^{-1}, and In-CO_3 has a vibration at 1451 cm^{-1}.[79–82] As seen with GaN there was a absorption near 2100 cm-1 which may arise from indium azide and nitrogen complexes. In the wavenumber range from 2800-3600 cm^{-1} there exists overlap between the O-H and N-H vibrations. Also in this region are C-H bending modes corresponding that arise from alkane, alkene, or alkyne species.

With increasing duration of air exposure following synthesis, the ranges from 2800-3600 cm^{-1} and from 1250-1750 cm^{-1} exhibit a growth in absorbance. This may result from water adsorption and continued oxidation of the particle surface. In the low wavenumber range from 400-650 cm^{-1} there is a decrease in absorbance which may result from the growing thickness of an oxide layer at the surface. This layer would make the detection of vibration modes closer to the core of the particle less sensitive and since this region is composed of In-N bonding a decrease in absorbance may manifest as a result.

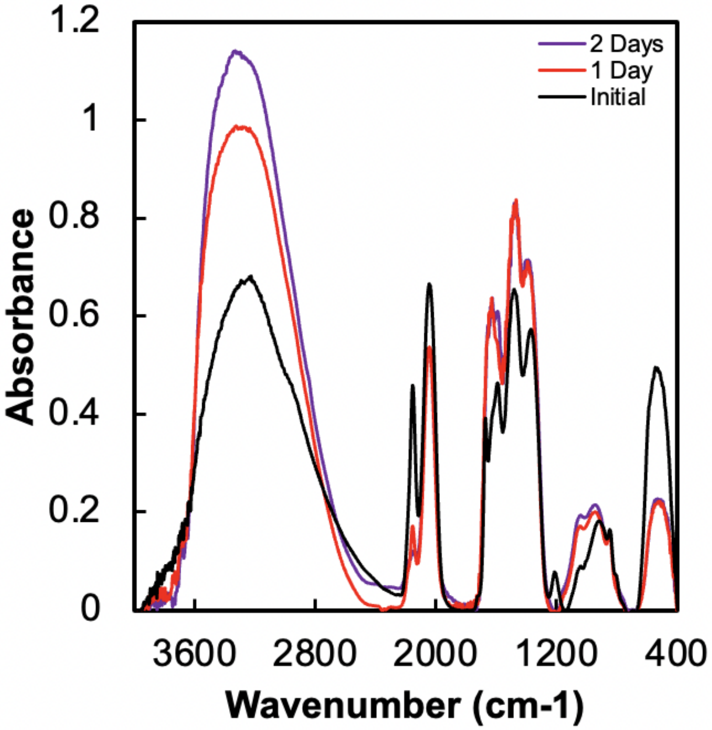

Figure 3.17: Representative FTIR spectrum of InN nanoaprticles.

3.3.2.3 Optical Properties

Absorption spectroscopy was used to measure the optical response of the InN nanoparticles. Multiple detectors were used to measure the absorption spectra of the InN nanoparticles. The absorption spectrum displays a feature at 1660 nm but this is an artifact that manifests from the NIR detector. The absorption data was transformed to form the Tauc penot which shows that the onset of absorption occurs near 775 nm. The extrapolation of the linear portion of the plot provided an estimate for the bandgap of 3.0 eV. This represents nearly a 2.3 eV shift of the bandgap from its bulk scale value - considering the small size of the particles as compared to the Bohr-exciton radius of InN (13.8 nm) such a shift is not unreasonable.[83] PL was not observed from the InN samples.

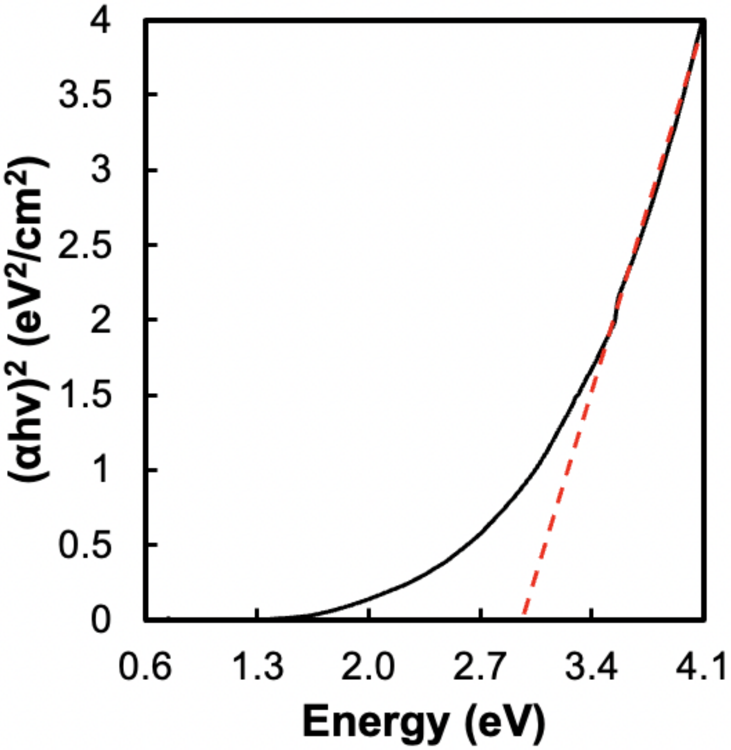

Figure 3.18: Tauc plot obtained from UV-VIS-NIR absorption spectrum of InN nanoparticles.

3.3.3 Indium$_x$ Gallium$_{1-x}$ Nirtide Synthesis

3.3.3.1 Size and Crystallinty Analysis

Synthesis of $In_xGa_{1-x}N$ presented many challenges, first of which was determining the set of conditions necessary to reliably produce particles. In order to determine the set of conditions that produced particles, weight measurements were conducted and correlated with several synthesis parameters to determine the appropriate range of conditions for synthesizing material. Parameters that were tracked include: residence time, power density, relative flow rates, and pressure. A wide range of residence times were used ranging from 3 ms to 66 ms with no clear relationship to the quantity of collected material. Similarly for power density which ranged over three orders of magnitude no relationship existed to the amount of collected particles (see appendix for methodology and calculation of power density). The same outcome existed for pressures between 3.8 and 9.0 Torr. The important parameters for consistently collecting deposition were the relative flow rates of

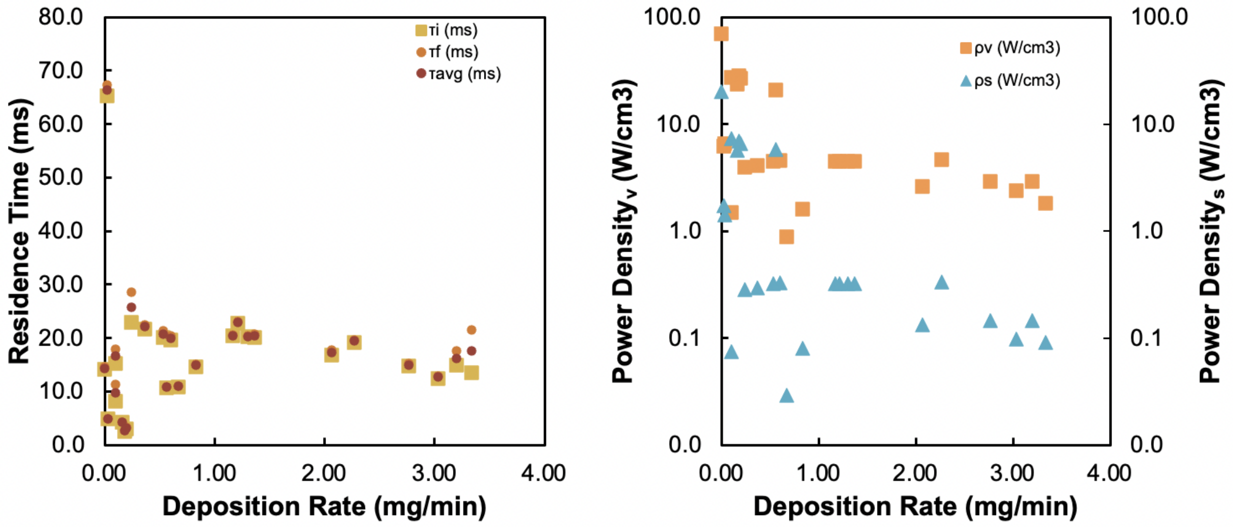

Figure 3.19: (a) Plot displaying the various residence times used to synthesize In$_x$Ga$_{1-x}$N nanoparticles and the rate of deposition.(b) Plot comparing the power density as measured using a voltage proxy (v) method or subtractive method (s) against the rate of deposition.

gases. To bring the deposition rate near 1 mg/min the ammonia flow rate composed 50% or more of the total flow and the TMG flow rate was in the range of 0.8 to 3.8 times the TMI flow rate.

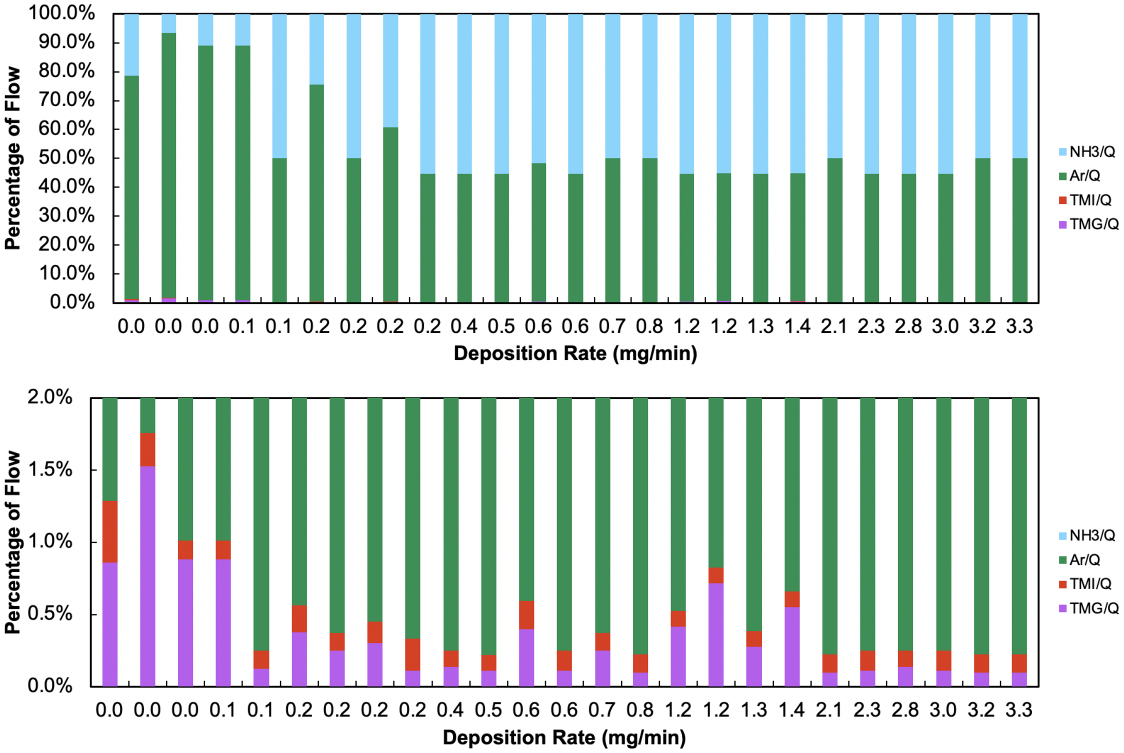

Figure 3.20: Bar charts that depict the relationship between the deposition rate and the relative flowrates (Q denotes the sum of all flows). The charts display the same data differing only by the scale of the "Percentage of Flow" axis.

XRD diffraction patterns showed the clear presence of peaks in the appropriate locations to suggest the formation of crystalline $In_xGa_{1-x}N$ nanoparticles. Small shifts in the maximum peak intensity occurred as compared to either InN nanoparticles or GaN nanoparticles. From the SAED and XRD patterns there is clearly the presence of crystalline nanoparticles. Assignment of the crystal structure is complicated due to size related peak broadening and the mixed composition of the particles. The component peak positions in the diffraction pattern will be dependent upon the concentration of indium and gallium in the lattice and the crystal phase. Often Vegard's law is used to estimate composition based off of this data.[84, 85] However due to the breadth of the peaks it is not possible to ascertain those individual components with certainty. Qualitatively the XRD spectra of $In_xGa_{1-x}N$ is positioned between that of InN and GaN which would be consistent with Vegards's law and thus the formation of an alloy consisting of indium and gallium is expected.

TEM and SAED were performed together to provide more structural information about the

Sample	TMG (sccm)	TMI (sccm)	τ (ms)	Diameter (nm)	Standard Deviation (nm)
1	1.30	0.20	22.9	3.9	1.4
2	1.00	0.20	20.4	5.3	1.5
3	0.75	0.20	20.5	4.7	1.4
4	0.50	0.20	20.3	4.8	1.7

Table 3.1: Table listing average diameter of particle synthesized at different TMG flowrates.

particles. Inspection of the TEM images showed that lattice fringes are present. Concordantly the SAED pattern contained two broad rings. The SAED image was mapped into the 2ϑ space by measuring the radial intensity of the rings and making the appropriate conversion from reciprocal space to 2ϑ space and revealed a similar shape to the pattern obtained using XRD. The peak intensity occurs at 32.6 degrees instead of 33.2 degrees but considering the error introduced in the conversion these values are in reasonable agreement. TEM was further used to obtain the size distribution of particles synthesized at several TMG flowrates (Table 3.1). Residence times were different for each sample but varied by maximum of 2.6 ms. Similar sized particles were found for each sample with a maximum difference in size of 1.4 nm was found.

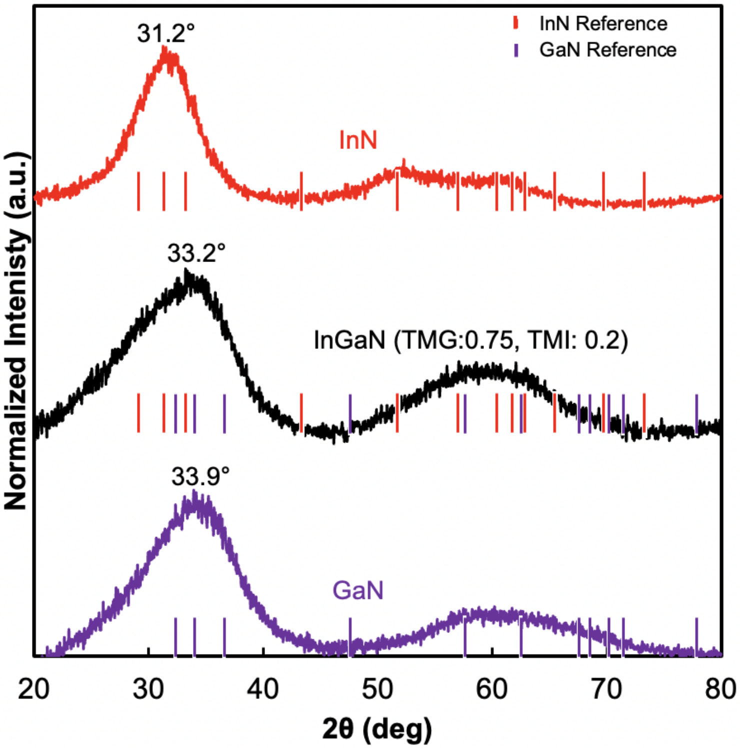

Figure 3.21: Comparison of XRD patterns for InN, $In_xGa_{1-x}N$, and GaN nanoparticles. The tick marks denote location of either InN or GaN peak positions from ICSD

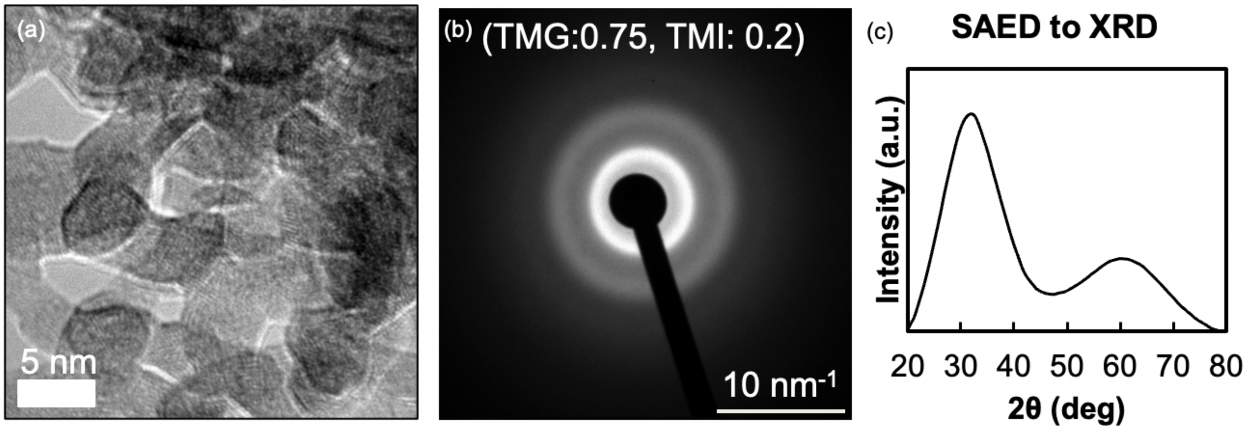

Figure 3.22: (a) TEM image of $In_xGa_{1-x}N$ nanoparticles. (b) SAED pattern of $In_xGa_{1-x}N$ nanoparticles. (c) Conversion of SAED pattern to XRD using radial intensity of SAED and conversion from reciprocal space to 2ϑ space.

3.3.3.2 Composition and Surface Analysis

In the case of a ternary compound gaining insight into the relative amounts of the constituent species is useful. As stated earlier the use of Vegard's law for accurate compositional analysis is made difficult by the convolution of the diffraction pattern. A qualitative approach can still be used to interpret Vegard's law as it provides an expected direction for the shift in data. From Vegard's law it would be expected as the amount of gallium in the lattice increases that the diffraction pattern would approach that of pure GaN. To observe this XRD was conducted on several $In_xGa_{1-x}N$ samples. The XRD data compared a baseline case where equal amounts of TMG and TMI were used during synthesis. The amount of TMG or TMI was then increased and samples were collected and measured to observe shifts in the diffraction patterns. GaN diffraction peaks occur at higher 2ϑ values than that of InN. In general the data presents modest shifts towards higher 2ϑ as the TMG flowrate was increased. There was not clear movement towards lower 2ϑ values of the diffraction with increasing TMI flowrate. A more clear progression may occur at higher TMI flowrates, but experiments were limited to a maximum flowrate of 0.4 sccm of TMI. At higher flowrate setpoints it was not possible to maintain the flow long enough to collect sufficient deposition for analysis. To further explore the composition of the $In_xGa_{1-x}N$ nanoparticles EDS was used. EDS was performed alongside TEM imaging of the particles. Atomic percentages were taken from the EDS spectra and used to determine the ratio of indium to gallium present in each sample. Samples 2, 3, and 4 from Table 3.2 have approximately the same ratio of In to Ga as the ratio of TMI to TMG. Sample 5 has a 1.25 to 1 ratio of TMI to TMG and a similar In to Ga ratio of 2:1. The outlier is sample 1 whose TMI to TMG ratio is 1 to 2.5 but In to Ga ratio is 1 to 17. Differences in ratio between metallic precursors and ratio between the metallic components in the alloy may arise from miscibility gaps in the $In_xGa_{1-x}N$ alloy,[86] incomplete utilization of the precursor, formation of metallic bonding in the particles, or to film growth on reactor walls. Further it should be noted that although EDS provides quantitative analysis it is prone to large errors especially when a standardless procedure.[87] For that reason the exact proportions of indium and gallium reported here by EDS should be treated with some skepticism and taken to be nominal values only.

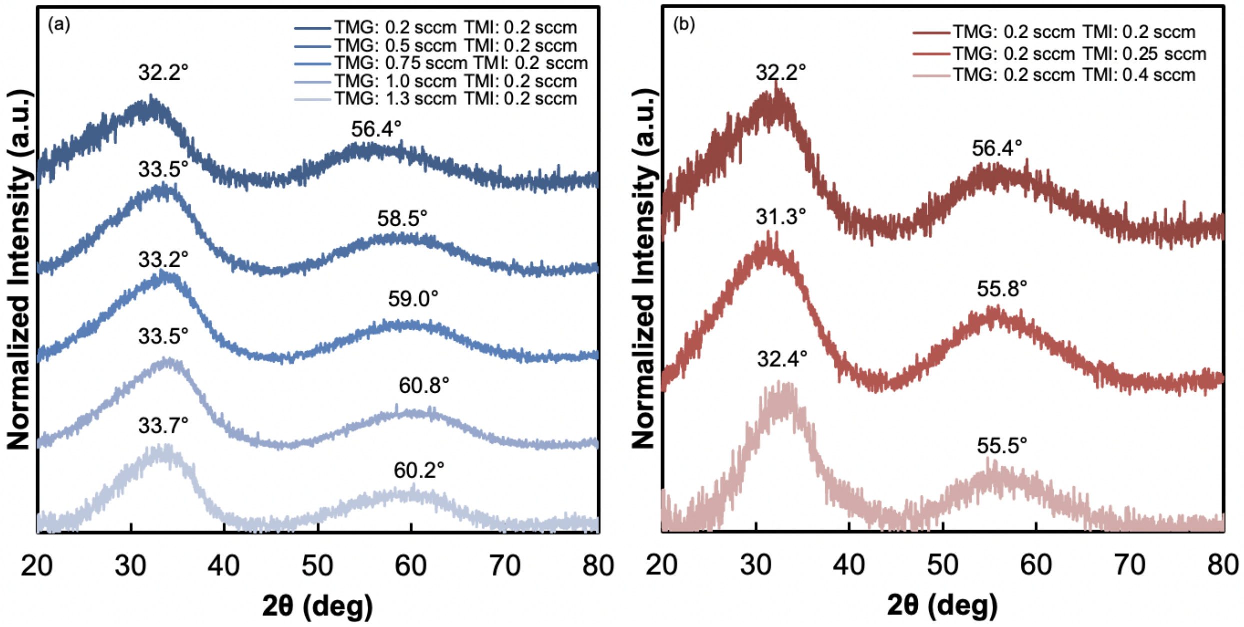

Figure 3.23: (a) XRD pattern of $In_xGa_{1-x}N$ nanoparticles synthesized with increasing TMG flowrate and constant TMI flowrate. (b) XRD pattern of $In_xGa_{1-x}N$ nanoparticles synthesized with increasing TMI flowrate and constant TMG flowrate.

Sample	TMG (sccm)	TMI (sccm)	In:Ga
1	0.50	0.20	1:17
2	0.75	0.20	1:3
3	1.00	0.20	1:5
4	1.30	0.20	1:10
5	0.20	0.25	2:1

Table 3.2: Table listing flowrates of metallic precursor gases and the resulting ratio of observed metallic species as measured by EDS.

FTIR was used to investigate the surface of the nanoparticles and provide corollary evidence for the formation of $In_xGa_{1-x}N$. If particles contained both metallic species, peaks would be expected that relate to both GaN and InN. In the wavenumber range from 400 to 800 cm^{-1} the $In_xGa_{1-x}N$ spectrum has peaks at 477 cm^{-1}, 524 cm^{-1}, 577 cm^{-1}, and 727 cm^{-1}. These peaks respectively are Ga-O, In-N, Ga-N, and Ga-N. The band at this wavenumber range is also broad and weaker absorptions may have occurred from other gallium and indium vibrations. As disccussed in previous sections from 800 to 1600 cm^{-1} a wide variety of absorptions may occur from groups that contain carbon, hydrogen, and nitrogen. As discussed from the InN section, in this range there exist vibration

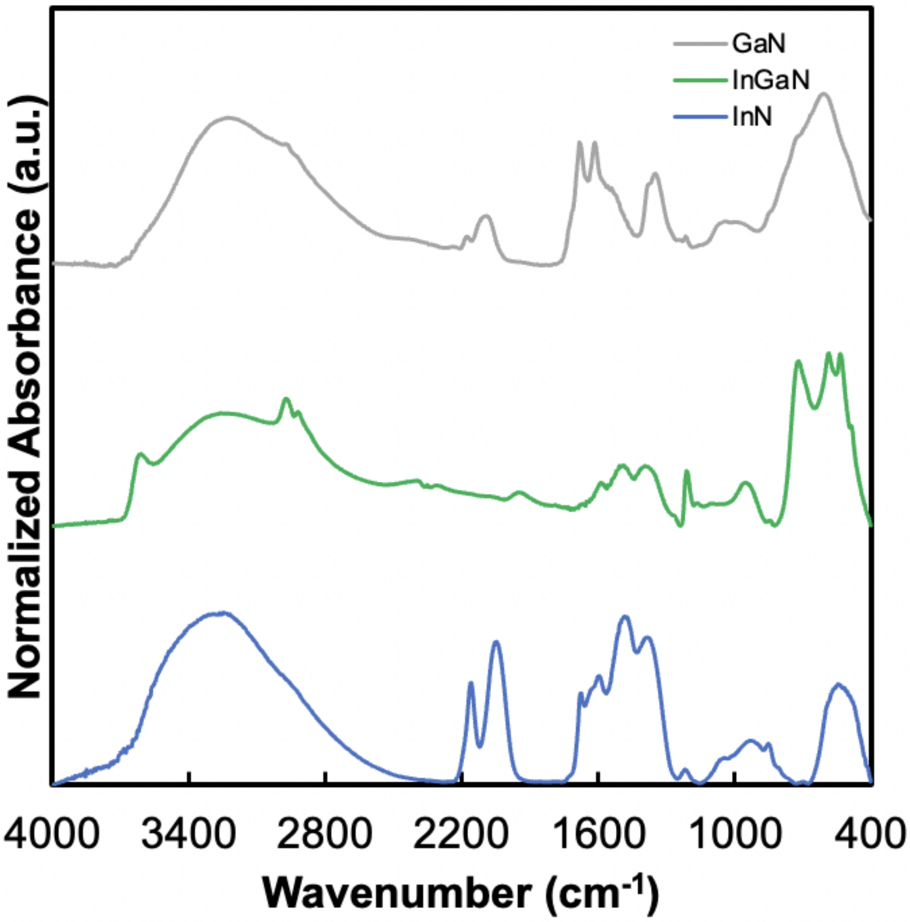

Figure 3.24: FTIR spectra of GaN, $In_xGa_{1-x}N$, and InN nanoparticles.

modes for In-N, In=N, In-OH, In-NO_3. Unlike in the GaN and InN there is no feature present near 2100 cm^{-1}. The small dip at 2300 cm^{-1} is from differences in the CO^2 between the background and measurement scan. In the 2800-3600 cm^{-1} range there is again the presence of N-H, O-H, and C-H_x with an additional O-H band at 3580cm^{-1}.

3.3.3.3 Optical Properties

$In_xGa_{1-x}N$ has the capability to emit from the infrared to the UV depending on the relative concentration of indium and gallium present in the material. Further modification of PL can arise from quantum confinement of the particles. To examine the emissive properties of the $In_xGa_{1-x}N$ particles PL spectra were collected immediately following synthesis and for days after synthesis

TMG (sccm)	TMI (sccm)	$PL_{0\ \text{Days (nm)}}$	$PL_{1\ \text{Day (nm)}}$	$PL_{3\ \text{Days (nm)}}$	$PL_{6\ \text{Days (nm)}}$
0.20	0.25	603	-	-	-
0.20	0.20	614	-	-	-
0.25	0.20	613	-	-	-
0.50	0.20	676	-	566	563
0.75	0.20	-	555	529	-
1.00	0.20	-	552	524	-
1.30	0.20	-	551	531	-

Table 3.3: Table listing TMG and TMI flowrates and peak PL emission for $In_xGa_{1-x}N$ samples.

using a 405 nm wavelength excitation source. In table 3.2 the results of the PL experiments are compiled. For TMG to TMI ratios of 0.8 to 1.25 the initial peak PL emission was between 603 and 613 nm. An increase of the ratio up to 2.5 corresponded with an increase in the initial peak emssion to 676 nm. The PL was measured again at 3 and 6 days post synthesis with PL shifts to 566 and 563 nm respectivley. This trend is in the opposite direction of the expected shift in PL. At higher TMG to TMI ratios between 3.75 and 6.5 the peak PL emission was recorded at 1 and 3 days post synthesis. At the 1 day mark peak emission was between 551 and 555 nm. At 3 days the PL shifted to between 524 and 531 nm. From this data it is clear PL shifts to higher energy with time with the majority of shifting occuring within the first few days after synthesis which is consistent with previous reports of PL from nanoparticles.[88, 89] There does not appear to be a trend of PL emission with precursor flowrate. This may result because changes in the precursor concentrations do not scale directly with changes in concentration of indium and gallium in the particles, or because shifts in composition come with commensurate shifts in bandgap widening due to quantum confinement - meaning that the correlation between composition, size, and optical bandgap is a complicated and yet-to-be elucidated map.

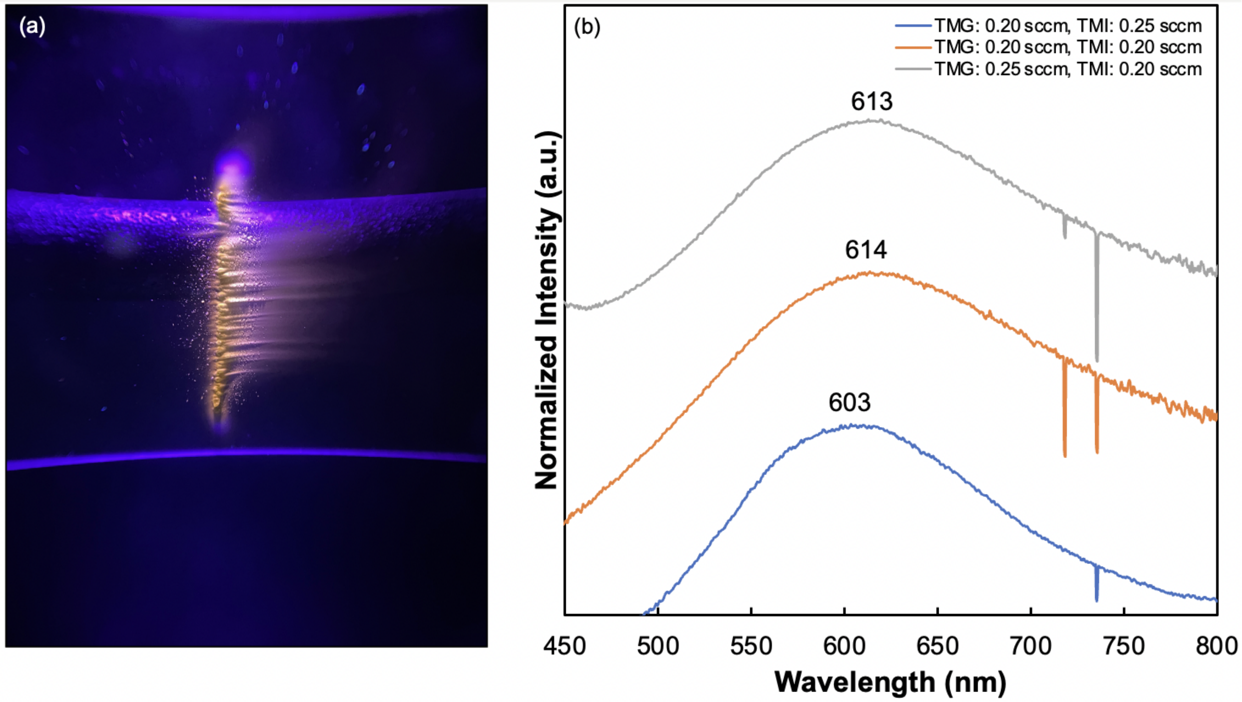

Figure 3.25: (a) Image of PL from $In_xGa_{1-x}N$ sample with 405 nm LED. (b) PL spectra of $In_xGa_{1-x}N$ nanoaprticles excited with 405 nm LED

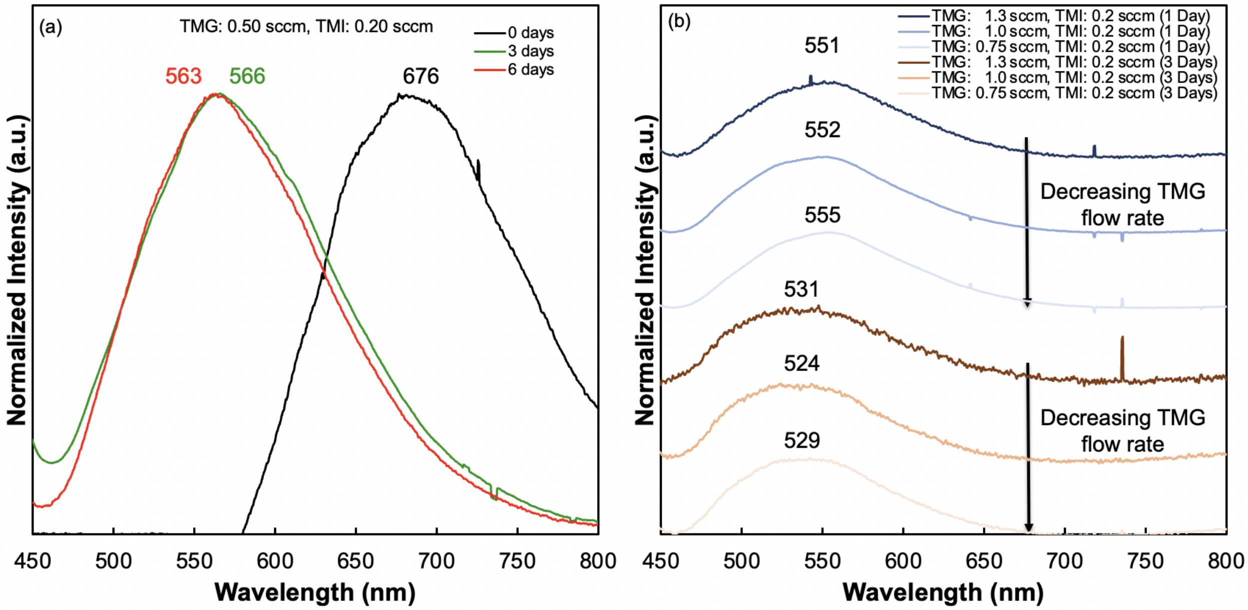

Figure 3.26: (a) PL emitted from $In_xGa_{1-x}N$ sample immediatley ater synthesis, 3 days, and 6 days post synthesis.(b) PL emitted from $In_xGa_{1-x}N$ samples at 1 and 3 days post synthesis.

Absorption spectra were collected for $In_xGa_{1-x}N$ samples. Samples were dispersed in toluene and the absorption spectra were then measured.

3.4 Conclusions

In this chapter a plasma based method to synthesize GaN, InN, and $In_xGa_{1-x}N$ nanoparticles was presented. Demonstrated was the ability to tune particle size through control of the residence time. Control over crystallinty was shown by meeting the power threshold necessary to heat particles to their crystallization temperature. The IR spectra showed the presence of fairly stable surfaces that contain bonding consistent with the chemical environment during and following synthesis. Emission from GaN and InN nanoparticles is an area of future research that will require detailed analysis of defects and composition of the nanoparticles. PL from $In_xGa_{1-x}N$ nanoparticles was readily observed without any surface functionalization and the emission was found to shift to higher energies with increasing time after deposition.

CHAPTER 4

ATMOSPHERIC PRESSURE SYNTHESIS OF SILICON NANOPARTICLES

4.1 Introduction

Atmospheric pressure synthesis of nanoparticles is motivated by a number of factors. The first is the reduction of cost through the elimination of the vacuum equipment required for operation at low pressure. Operation at atmospheric pressure eliminates the need for a pump, enclosures, vacuum gauges, etc. Several groups have demonstrated synthesis of nanoparticles at atmospheric pressure using plasma methods.[90,91] These include Askari *et al.*[92] who used a silane plasma to generate luminescent silicon nanoparticles. Ivanov *et al.*[93] used a spark discharge generator to synthesize silver nanoaprticles.To fully realize the promise of atmospheric pressure synthesis and eliminate the need for vacuum equipment it is necessary to be able to synthesize nanoparticles with a ambient air environment. In this chapter a method for the synthesis of crystalline silicon nanoparticles without the need for an inert environment is presented.

4.2 Experimental Setup

4.2.1 Atmospheric Pressure Reactor

Synthesis at atmospheric pressure requires higher power densities than those at lower-pressures in order to satisfy discharge conditions.[94] The power density requirement can be satisfied by miniaturization of the reactor, and several other groups have explored DC microplasma synthesis of silicon nanoparticles.[90,95,96] Here, a miniaturized RF plasma is used instead. Similar to the other reactor setups described earlier a glass tube and cylindrical electrodes were used to form the reactor. For this reactor the tube's inner diameter was between 1 and 0.9 mm and a two electrode configuration was used. The typical plasma length was between 10 and 20 mm. A Tesla coil, 13.56 MHz RF power generator, and impedance matching network were used to ignite and sustain the plasma. Flown to the reactor was a precursor gas of silane and background gas of argon. The silane cylinder contained a gas mixture of 1% silane and 99% argon, when disscussed later silane flowrate refers to this specific gas mixture. Gas flowrates were controlled with Alicat mass flow controllers. Prior to initial introduction of silane a purge cycle was implemented to remove air from the gas lines. Prior to each synthesis experiment an argon plasma was ignited before introduction of silane to reduce the risk of reaction of silane with the air.

Unlike the experiments described previously samples were synthesized at or near atmospheric pressure and samples were collected directly downstream of reactor onto various substrates with the reactor outlet left open to the atmosphere. Substrates were placed 1 mm downstream from the reactor outlet. To investigate the difference between an inert and an air atmosphere a stainless steel vacuum chamber (IdealVac) was used to purge the air from the enclosure and replace the air with argon. Pressures near atmospheric pressure were measured with a a standard pressure gauge just upstream of the reactor. Low pressures were measured with a MKS 626 Baratron gauge or Granville-Phillips convectron gauge mounted to the vacuum enclosure. The higher pressure environment for these experiments always required the use of a Tesla coil to ignite the plasma. The design of the stainless steel enclosure was such that the electric field could not pass into the enclosure. To strike the plasma a glass tube with a central wire conductor was capped at one end with a stainless steel ultra-Torr fitting. The tube was then mounted to a linear motion feedthrough so that the tip of the wire could be placed in close proximity to the reactor. The assembly was then coupled to the Tesla coil and used to ignite the plasma.

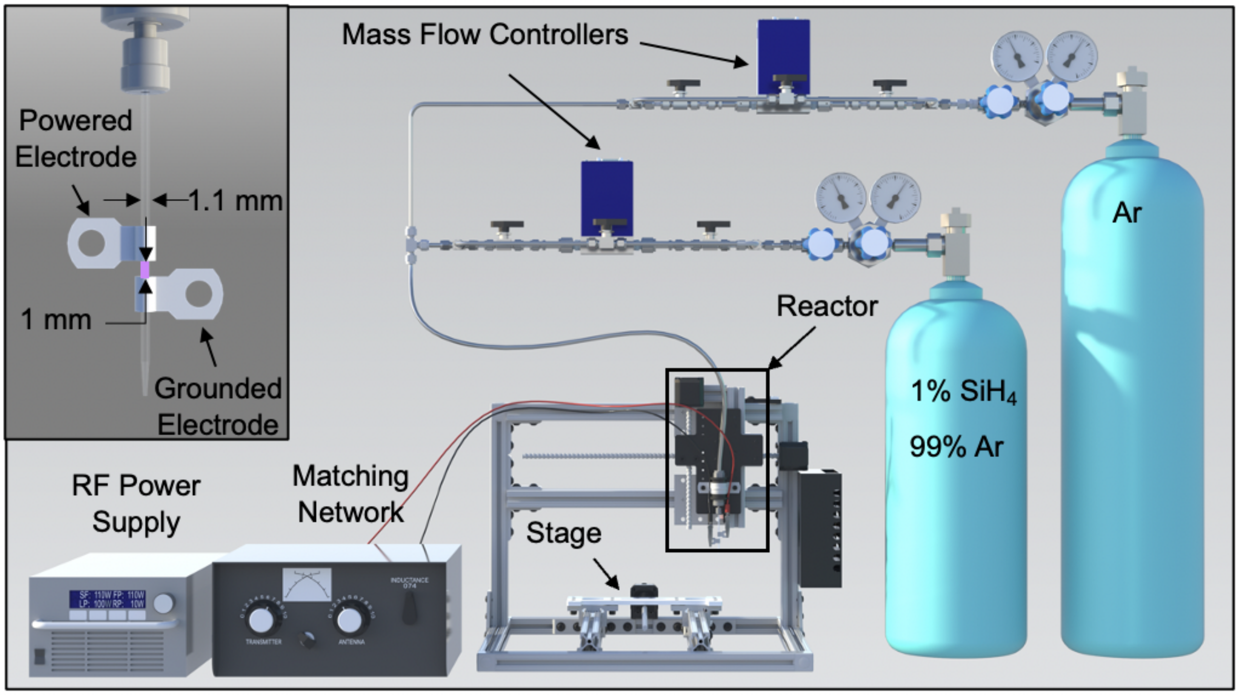

Figure 4.1: Rendering of components used to synthesize silicon nanoparticles at atmospheric pressure. Not depicted here is stainless steel enclosure used to create air-free environment for synthesis. Enclosure contained the reactor, stage, and associated components used to move the stage and reactor.

4.3 Results and Discussion

4.3.1 Process and Structural Characterization

XRD and TEM were used in conjunction to examine the crystallinty of the silicon nanoparticles. Samples were synthesized with a power of 90 W, argon flowrate of 250 sccm, and silane flowrate of 5 sccm. The diffraction pattern contained the characteristic peaks of crystalline nanoparticles at 28.8, 47.4, and 56.4 degrees which represent the (111), (220), and (311) directions of the silicon lattice. TEM bright-field imaging revealed that the particles contain a crystalline core with an amorphous edge suggesting the formation of a core shell structure. Similarly the dark-field images present numerous bright spots throughout the sample, indicative of crystalline nanoparticles. Exposure of the nanoparticles to air allows for the formation of an amorphous oxide layer at the surface (see section on surface oxidation for further discussion). TEM image analysis of the core yielded a

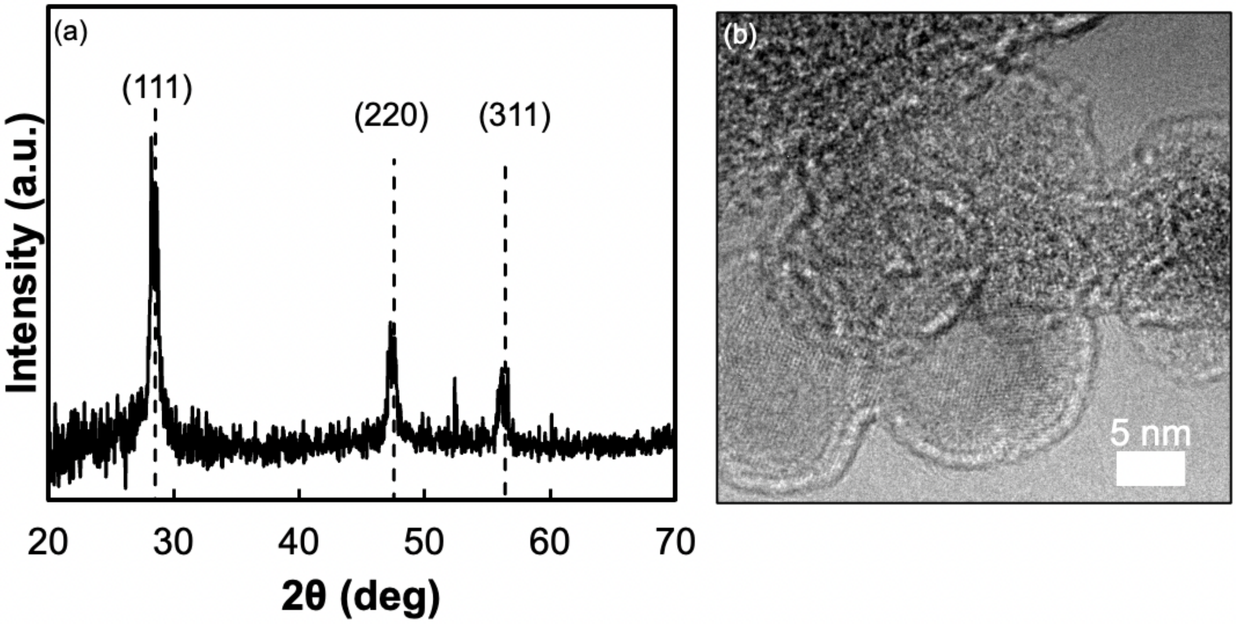

Figure 4.2: (a) XRD of silicon nanoparticles synthesized at 90W with diffraction peaks in positions typical of silicon nanoparticles. (b) TEM image of silicon nanoparticles synthesized at 90 W with lattice fringes present.

lattice spacing of 3.0 angstroms which is within 3% of the 3.1 angstroms spacing that corresponds with the (111) crystallographic direction.

TEM and XRD were further used to estimate the particle size and distribution. For the conditions above Scherrer analysis of the XRD pattern yielded a value of 7.1 nm. TEM image analysis yielded an average particle size of 7.5±0.6 nm. Close agreement between the TEM and Scherrer analysis was found.

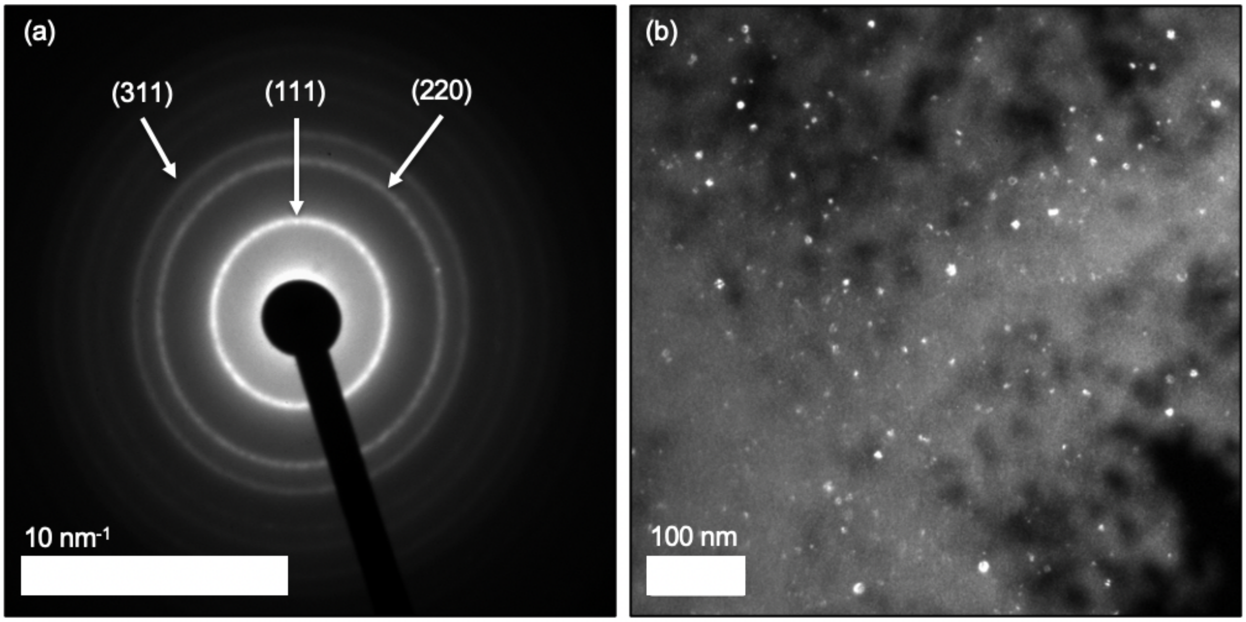

Figure 4.3: (a) Indexed SAED pattern of silicon nanoparticles. (b) Dark-Field TEM image of silicon nanoparticles.

TEM analysis was used again on samples synthesized at different flowrates. The silane flowrate and argon flowrate were adjusted such that similar silane concentrations and residence times could be compared; details of parameters are listed in table 4.1. The general trend is as residence time decreases the average nanoparticle diameter decreases. Consider the sample pairs of 1-3 and 2-4. The sample pairs allow for the effect of concentration to be ignored and demonstrate that the residence time alone decreases the particle size. Comparison of samples 3 and 4 shows that despite sample 4 having a smaller residence time than sample 3, the increased silane concentration is sufficient to push the nanoparticles to a higher average diameter. The behavior between concentration and residence time has been observed in low pressure plasma synthesis and is replicated here at atmospheric pressure.[18] The particle diameter coefficient of variation varied from 0.04 to 0.10, which is similar to other reports of nanoparticle synthesis at atmospheric pressure.[97]

Sample	Ar (sccm)	SiH_4 (sccm)	SiH_4 (PPM)	τ μs
1	250	5	196	144
2	300	5	164	120
3	400	5	123	90
4	500	10	196	72
5	600	10	164	60
6	700	10	141	52

Table 4.1: Table listing parameters for silicon nanoparticles and the resulting silane concentration and residence time.

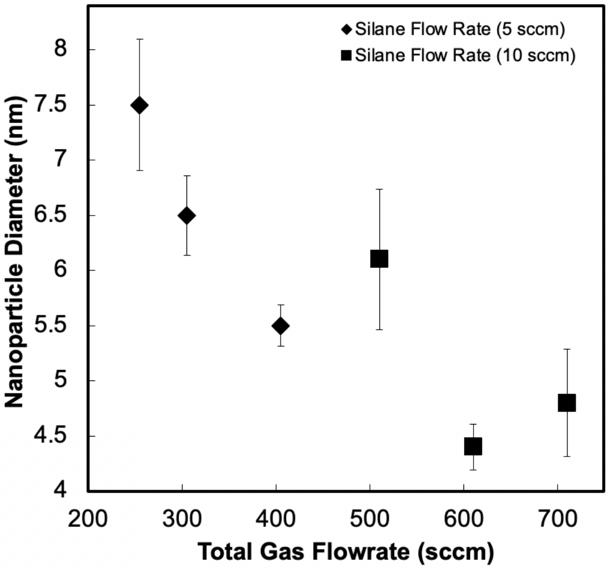

Figure 4.4: Change in nanoparticle diameter at various combinations of argon and silane flowrates.

The absolute throughput of the reactor is important to consider. Mass measurements were made to identify the amount of material synthesized. The mass deposited onto both the substrate and reactor walls was measured to compare the amount of useful deposition to waste deposition. The amount of deposition was measured for 30 and 60 min time intervals. For these measurements a argon flowrate of 250 sccm and silane flowrate of 5 sccm was used. This was done to examine if the film growth on the reactor walls would significantly inhibit the deposition rate. In the box and whisker plots the "x" marks the average rate of deposition, the horizontal lines of the "box" denote the fist and third quartiles, and the horizontal lines at the end of the "whiskers" denote the range of the data. The measurements demonstrate that on average 20% of deposition occurs on the substrate

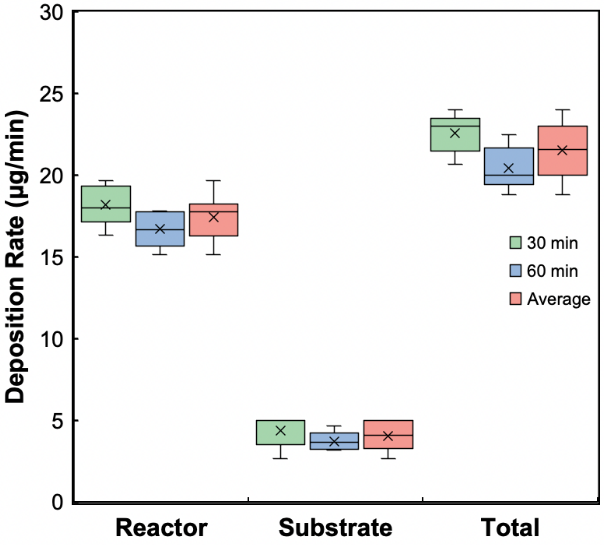

Figure 4.5: Depositon rate of silicon nanoparticles onto the reactor walls and substrate.

while the reaming is lost to the reactor walls or is not collected. Deposition rates onto the reactor walls and substrate at 30 and 60 minutes had relative differences of 8% and 15% respectively.

To estimate yield of the reaction a calculation was performed to estimate the maximum amount of material that could be obtained assuming all of the silane was dissociated and reacted to form silicon. This was then compared against the total mass collected on both the substrate and walls to estimate the yield. This analysis found a yield of approximately 50%. At low pressure it has been estimated that nearly 100% of silane is utilized.[18,98] This value indicates either a significant amount of silane does not react to form solid material or a large fraction of particles were not collected. A potential mechanism for particle loss is related to the impaction efficiency of the particles. Since the particle momentum is small in comparison to the drag force, the tendency is for particles to be carried away by the flow instead of impacting. This is discussed in detail in the following chapter.

4.3.2 Surface Oxidation

The matter of oxidation of the particles is important to consider in this application as particle synthesis occurred with an ambient air environment. To study this a combination of OES, FTIR, and TEM were used. OES was used to examine if air was diffusing into the reactor and producing

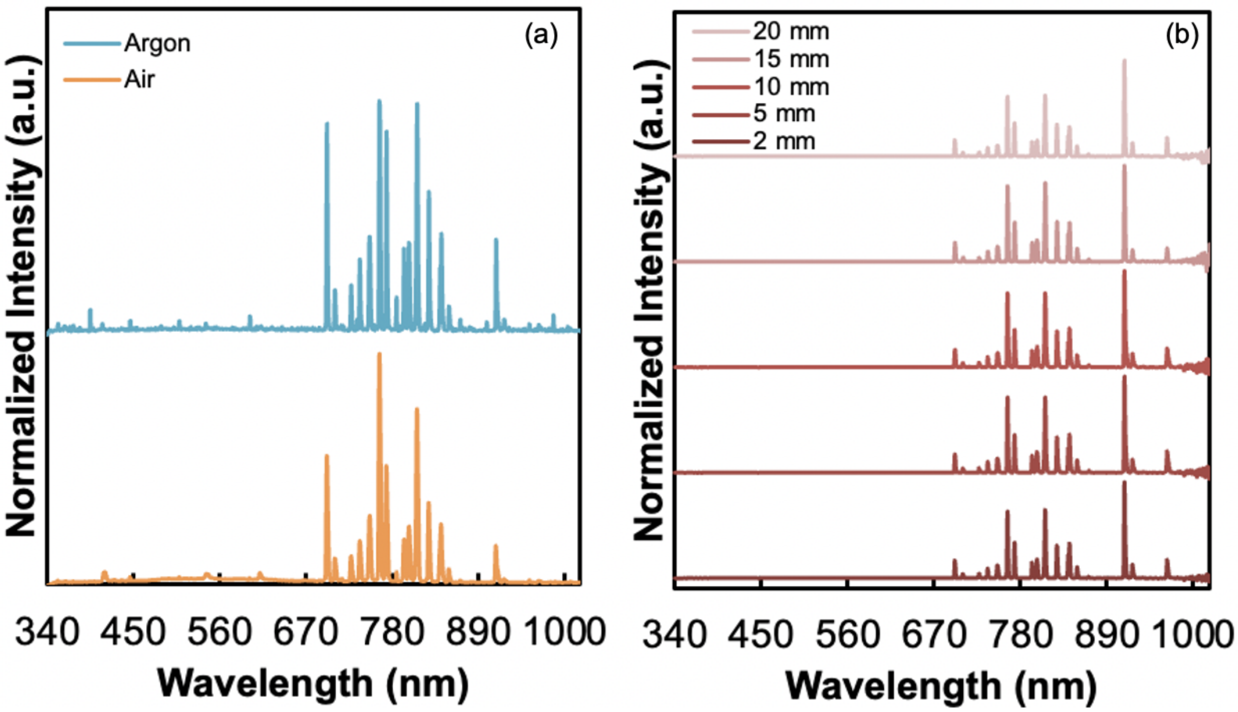

Figure 4.6: (a)Comparison of OES spectra collected with a surrounding argon atmosphere and an air atmosphere.(b) OES spectra collected at various distances from the reactor outlet with a surrounding air atmosphere

reactive air species in the plasma volume. In the first OES experiment, the optical fiber was aligned at 2 mm from the outlet of the reactor and the spectrum was collected. The optical fiber was then progressively translated up the reactor to several positions and spectra were collected to identify if air was present in the reactor. Analysis of these spectra shows no presence of peaks corresponding to either nitrogen or oxygen. Many of the peaks present in the spectra were attributed to the strong lines of Argon. In the second OES experiment spectra were collected with either a surrounding ambient air atmosphere or an argon atmosphere. The argon atmosphere was established by placing the reactor into the stainless steel vacuum enclosure and performing a purging procedure to minimize the concentration of air species and fill the volume with argon. The resulting OES spectra showed no difference in peak locations and the lines in the spectrum were all attributed to argon.

FTIR was used to further examine the effects of oxidation. To do so FTIR spectra were collected from samples at multiple times following synthesis. Initial FTIR spectrum was collected 20 minutes after deposition began. Delay between deposition and spectrum collection was needed

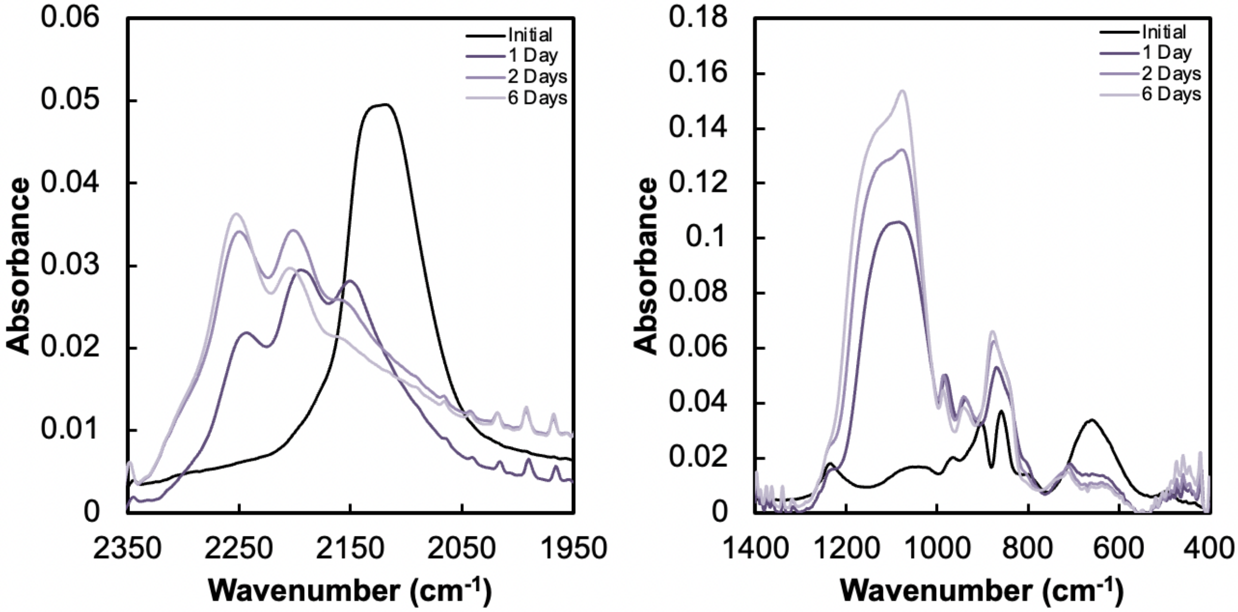

Figure 4.7: FTIR spectra of silicon nanoparticles taken at time several intervals post synthesis.

for the deposition of particles and transfer of substrate to the FTIR instrument. Silicon nanoparticle oxidation can be observed with FTIR in the ranges of 400-1400 cm^{-1} and 2000-2300 cm^{-1}. From 1000 to 1250 cm^{-1} are the characteristic Si-O-Si vibrations.[99] At the time of the initial scan there is a small amount of absorption present from this mode. As time increases from deposition the Si-O-Si region peak absorbance increases by nearly an order of magnitude.

In the region from 2000-2300 cm^{-1} exists a mixture of vibration for SiH_x and SiO_yH_x. The SiH_x vibrations occur at wavenumbers below 2150 cm^{-1} whereas the SiO_yH_x modes are at wavenumbers greater than 2150 cm^{-1}.[100] From the inital FTIR spectrum the peak centered at 2120 cm^{-1}, the peak is composed of Si-H, Si-H_2, Si-H_3 at 2086, 2112, and 2136 cm^{-1} respectively.[101] Also present at the initial scan are weak contributions from oxidized forms of the silicon hydrides .As time progresses and oxidation proceeds the vibrations shift to higher wavenumbers with peaks corresponding to 2155, 2206, and 2255 cm^{-1} which are related to oxidized hydride species.

In the high wavenumber range of 3300-3900 cm^{-1} are where characteristic O-H and N-H vibrations tend to present. At the initial scan there is little to no absorption in this region. As time progresses small peaks through the range being to develop likely from water adsorption and O-H species. If large amounts of N-H and O-H were present at the surface a broad and pronounced

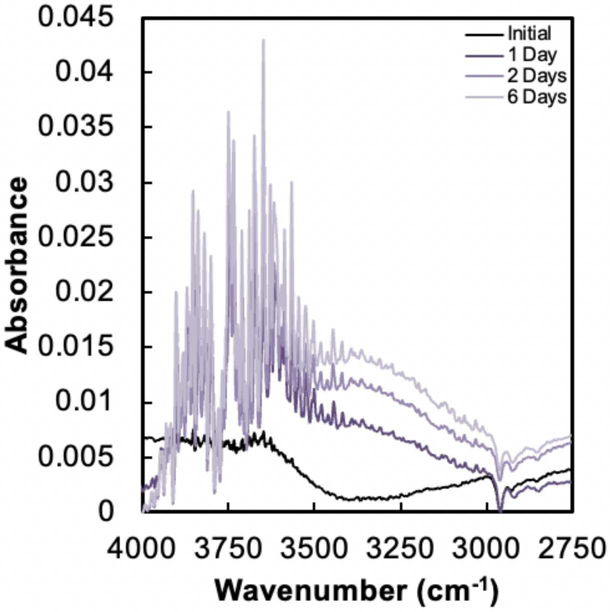

Figure 4.8: FTIR spectra of silicon nanoparticles taken at time several intervals post synthesis.

absorption band would be expected in this range as evidenced by the FTIR of the III-nitrides and studies of silicon nitride.[102] In the range from 750-1000 cm^{-1} there are a number of features in the initial spectrum that could be assigned to Si-H, or Si-N. However the characteristic Si-N mode typically presents as a broad feature near 850 cm^{-1},[103–105] in this spectra a sharp feature at 856 cm^{-1} is present. Furthermore the features at 856 and 899 cm^{-1} are a doublet often associated with the bending and wagging mode of silicon hydride species.[101, 106] In addition the change in spectra with increasing time is consistent with previous reports of silicon nanoparticle oxidation.[107]

The lack of silicon nitride related adsorptions and the growth of oxide absorptions in the IR and lack of oxygen or nitrogen peaks in the OES indicate that little to no air is present during synthesis. The presence of lattice fringes in the TEM and the corresponding XRD data provide additional evidence for oxide free particles at the time of synthesis. The combination of these measurements supports the claim for a plasma environment with minimal air contamination.

4.3.3 Optical Properties

Absorption spectroscopy and PL were utilized to investigate the optical properties of the silicon nanoparticles. Samples were synthesized with an argon flowrate of 250 sccm, silane flowrate of 5 sccm, and a power of 80 W. From Scherrer analysis particles have a diameter of 3.5 nm. Debate exist about the nature of the transitions that result in PL from silicon nanoparticles. Silicon has an indirect bandgap and in its bulk form does not exhibit PL. This is because indirect transitions (combination of momentum and energy, as opposed to energy alone for direct transitions) occur when electrons relax back to the valence band. However nanocrystalline silicon can exhibit PL. It is argued that when the particle size is made sufficiently small that the interplay between Heisenberg's uncertainty principle and the excited-state electron's momentum becomes important. The uncertainty in electron momentum from the confinement of the electron results in direct-like transitions to occur[108–111] For this reason two Tauc plots were constructed with a 1/2 and 2 exponent for the indirect and direct transitions respectively. The Tauc plot with indirect transitions yielded a value of 1.0 eV which would indicate a decrease in bandgap energy. A decrease in bandgap energy would not be expected for particles with a diameter smaller then the Bohr-exciton radius of 5 nm. Transformation of absorption data for direct transitions to a Tauc plot indicates an onset of absorption at 1.4 eV and an bandgap estimate of 2.8 eV. This estimate represents a shift of 1.7 eV from the bulk bandgap of silicon. PL was not typically observed from silicon nanoparticle samples produced using the atmospheric pressure reactor described here. PL *was* observed when the method for particle collection was modified. Typical samples were collected with the placement of a substrate underneath the reactor outlet. In the scheme where PL was detected a 6kV bias was applied to the substrate. PL was then observed around the edges of the deposition at 680 nm with the use 405 nm excitation source. Nanoparticles tend to accumulate charge while in the plasma. The interaction between the charged particle and the substrate may result in increased impaction efficiency of the nanoparticles allowing for PL to be observed. As noted earlier a more detailed description of the impaction efficiency will be presented in the following chapter.

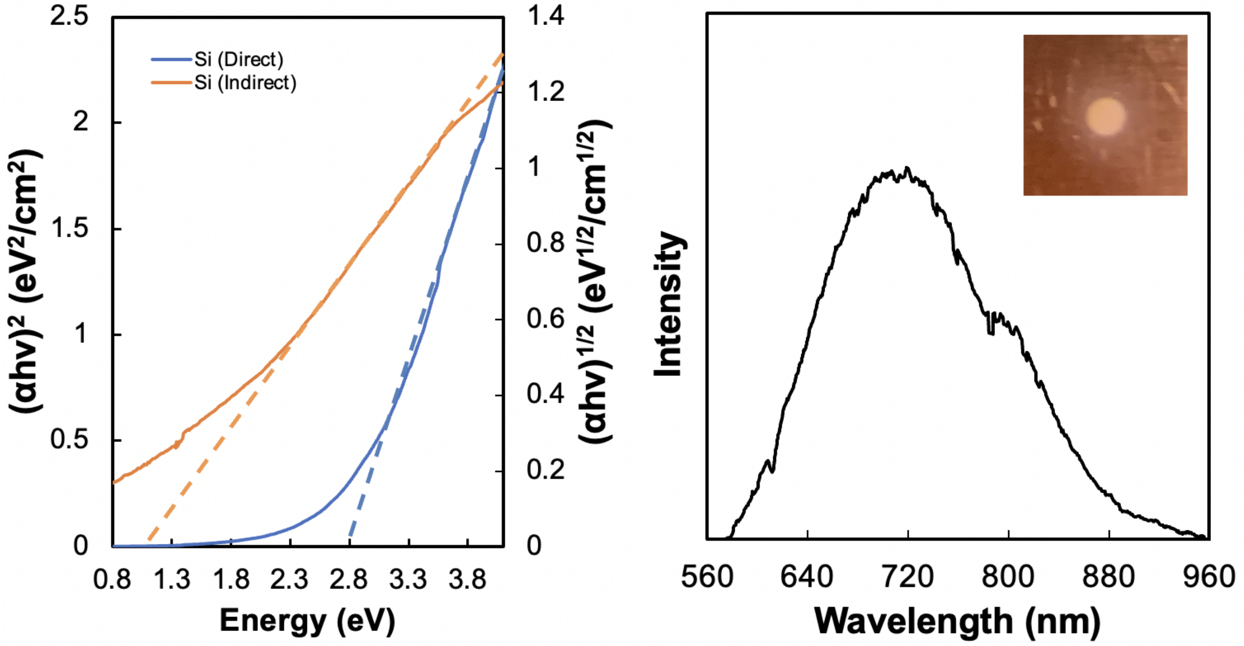

Figure 4.9: (a) Tauc plot of silicon nanoparticles. (b) PL spectrum of nanoparticles. Inset is deposition of particles onto a copper substrate, the central portion did not exhibit PL while the outer edge had visible PL.

4.4 Conclusion

This work demonstrated the ability to synthesize crystalline silicon nanoparticles at atmospheric pressure. This method eliminated the need for a vacuum system, while still allowing the production of high quality nanoparticles. Nanoparticles exhibit desirable characteristics such as narrow size distribution, particle sizes below 5 nm, and crystalline structure. Particles are also synthesized with minimal oxide content despite the surrounding air atmosphere. The typical low pressure methods for size control through variation of residence time and precursor concentration were shown to be suitable at atmospheric pressure. PL was also demonstrated to occur but with limited success leaving opportunity to further explore synthesis conditions to obtain nanoparticles with functional qualities.

CHAPTER 5

DRY AEROSOL JET PRINTING OF SILICON NANOPARTICLES

5.1 Introduction

Dry aerosol jet printing is similar to typical aerosol jet printing - the difference being that no liquid solvent is used in the process. Motivation for removal of solvent is to reduce contamination and processing issues associated with the use of a solvent. While the removal of the solvent provides benefit there are number or problems that need to be addressed. The solvent provides benefit for the efficient deposition of particles through the increased inertia of the droplet. When particles are dispersed into liquid droplets, line widths of 20 microns have been achieved.[23] The Stokes number (Stk) is used to quantify the ratio between particle momentum and the fluid drag force acting upon that particle.[112]

Outcomes such as resolution, reduction of overspray, and particle collection are influenced by the impaction efficiency. Many factors modulate the impaction efficiency including many particle surface phenomena such as particle bounce, particle loading, particle blow off, and selection of substrate.[113–115] From a particle-flow perspective the impaction efficiency is best described by the Stokes number.The Stk is defined as,

$$Stk = \frac{\rho_p d_p^2 C_c U}{9 \mu_f D} \tag{5.1}$$

Here ρ_p is the material density of the particulate phase, d_p is the particle diameter, C_c is the Cunningham slip correction factor, μ_f is the viscosity of the fluid, D is the diameter or characteristic length of the flow outlet. This number compares the particle's momentum to the drag force acting upon the particle. Thus when the StK is small the drag force dominates and particle trajectories closely trace the flow streamlines. Whereas when the Stk is large the particles momentum dominates and detachment from the flow occurs resulting in impaction. Ideally at some Stk there would be a step function response where all particles of a given size and larger are collected. However typical collection curves have an S-shape where a small fraction of particles smaller than a given size are collected and small fraction of particles large than the given size are lost. For this reason a Stk_{50} is defined to denote when 50% collection efficiency occurs for a particular sized particle.[113, 116]

5.2 Experimental Setup

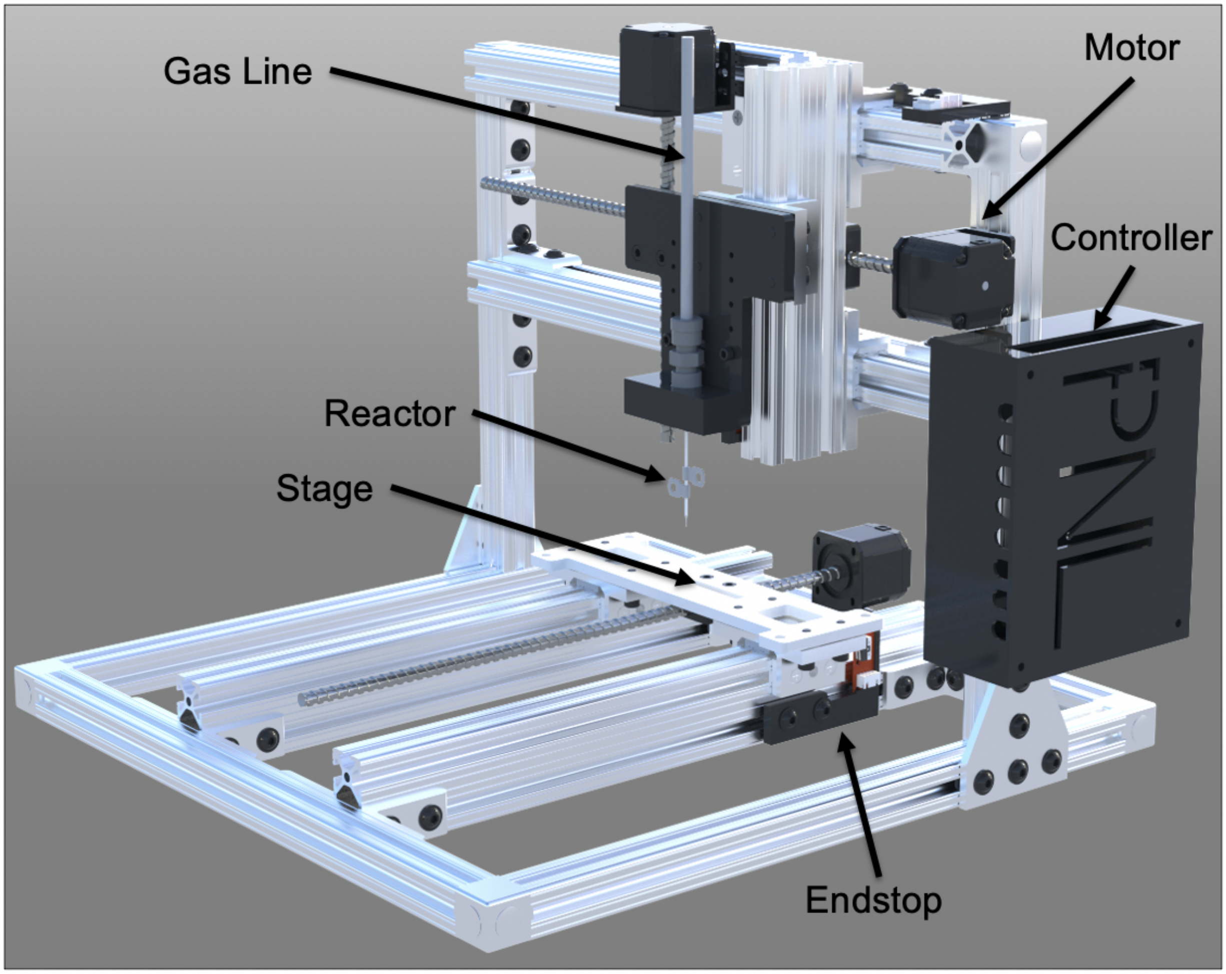

Figure 5.1: Rendering of components used to deposit silicon nanoparticles with inkless aerosol jet printing approach.

The experimental setup for the printing of particles consisted of two systems. The first is the reactor described in section 4.2.1 and the second was a motorized stage and gantry. The reactor and motorized components were used in tandem to synthesize and deposit particles in pre-determined geometries. The structural elements were constructed from extruded T-slot aluminum. Three stepper motors (Pololu NEMA 17) were used to either drive the stage, gantry, and reactor along independent axes. Attached to each stepper motor was a 8 mm leadscrew, around each leadscrew was an anti-backlash travel nut to prevent step losses during printing. Mounted to the travel nut were linear bearings that translated on the T-slot aluminum. The reactor and z-axis motor were mounted to the gantry and the stage translated along a single axis underneath the gantry. On each axis were mounted mechanical endstops (Pololu) to provide reference positions to the controller (Deut Wifi3D). To create toolpaths CAD software was used to generate desired geometries. The CAD file was then used in slicing software to generate toolpaths that were then executed by the controller.

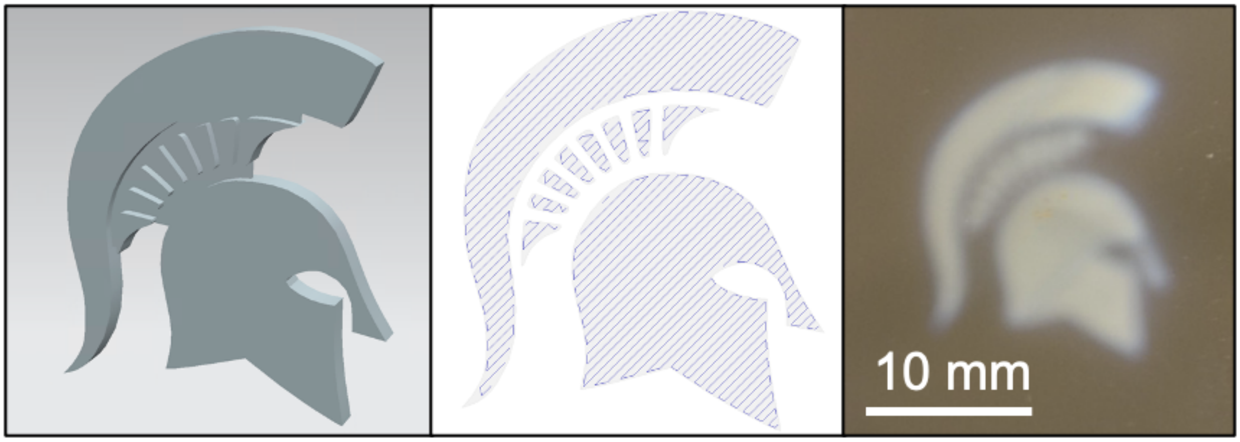

Figure 5.2: From left to right: CAD model, software generated tool path, and sample.

Several sets of experiments used drawn capillary tubes to create nozzles or constrictions. A Sutter P30 capillary tube puller was used to create these geometries. When the capillary tube puller was used for nozzle formation the tubes would be pulled until separation. Because the puller uses a heated filament to melt the tube during the pulling process, the ends become sealed after separating. Following separation the end were mechanically opened and outlet diameters were measured with a digital microscope. Aerodynamic lenses with a converging-diverging sections were also constructed by pulling on sections of the tube to a diameter of 0.3 mm.

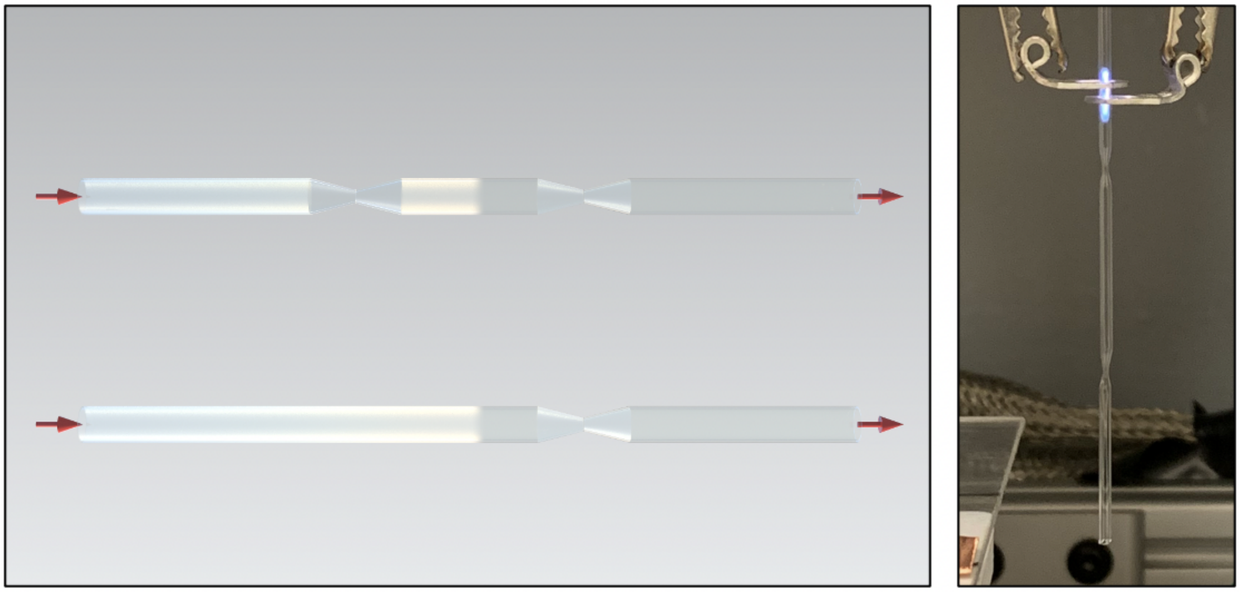

Figure 5.3: Rendering and Image of tubes used for aerodynamic lenses.

A high voltage power supply capable of supplying up to 15 kV was used in experiments to bias conductive substrates. The substrates were biased by attaching the electrodes to two plates separated by a dielectric material of quartz.

5.3 Results and Discussion

5.3.1 Printing Resolution

The printing resolution that the system is capable of printing is important to characterize as it relates to the types of structures and application spaces that this process can be used for. The resolution was evaluated by measuring the linewidth of deposited nanoparticles. Samples were deposited onto glass or copper substrates with an argon flowrate of 250 sccm and a silane flowrate of 5 sccm. Samples were deposited in straight lines with a print head speed of 1 mm/s. Reactor tubes were pulled to form nozzle whose outlet diameters are specified in table 5.1. Samples were then imaged and measured with a digital optical microscope. A minimum linewidth of 100 μm was achieved. Inspection of images demonstrated a significant area of overspray as is common in aerosol jet printing techniques.[117–119] A rough estimation of the overspray was made by plotting

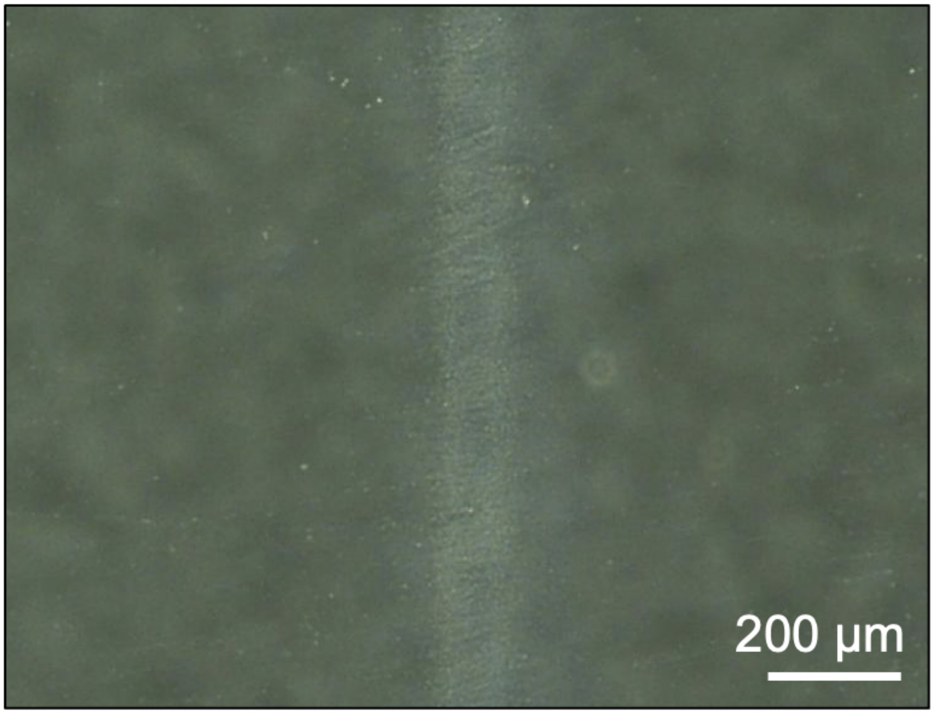

Figure 5.4: Optical image of silicon nanoparticles deposited in a line.

the gray value vs distance and comparing the FWHM to the width at which the gray value returned to baseline. This estimated the overspray to be 2.3 times the width of the line, for a line to be considered of good quality the width of the overspray should be less than the FWHM of the line.[117]

To evaluate layer thickness a combination of SEM and FIB were used to expose the cross section of the deposition and allow for measurements of the layer thickness. Samples were deposited onto a silicon wafer, the reactor was passed over the wafer twice, the FIB was then used to mill away a section of the material, and SEM was used to image the exposed section. The reactor tube was not pulled and had an outlet diameter of 0.9 mm. An argon flowrate of 250 sccm, silane flowrate of 5 sccm, and print head speed of 1 mm/s were used. Several sections were milled from the sample which yielded an average layer thickness of 1.4 µm.

Sample	Outlet Diameter	Linewidth (μm)
1	569	1087
2	292	504
3	208	327
4	151	134
5	85	100

Table 5.1: Table linewidths of deposits from different nozzle diameters.

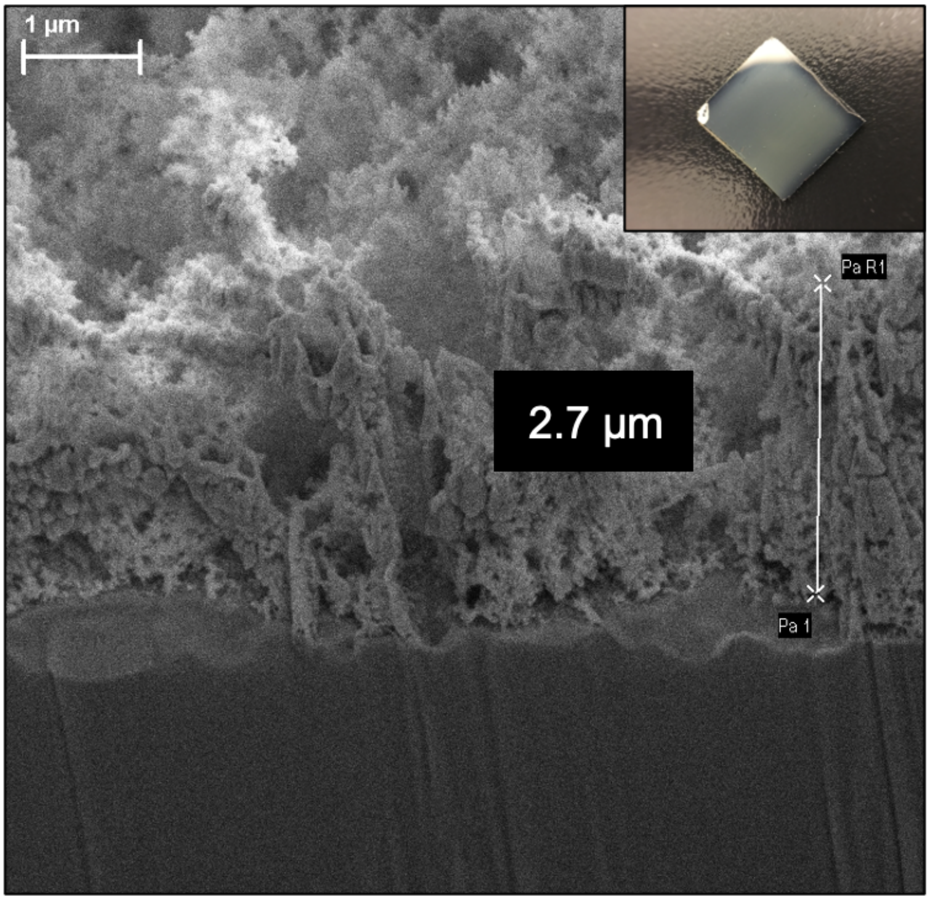

Figure 5.5: SEM image of nanoparticles deposited onto silicon wafer. Exposed section was milled with FIB.

5.3.2 Impaction Efficiency

Calculations of Stk were performed for several flowrates, pressures, and nozzle diameters to gain insight into the likelihood of particle deposition of sub 10 nm particles. From the plots of StK vs particle diameter it is clear in all cases as pressure decreases the Stk increases. This occurs because of the increased velocity slip between the nanoparticles and the flow as the pressure decreases. Also clear from the analysis is that at atmospheric pressure for any of the examined flowrates the likelihood of particle impaction for particles is quite small as the Stk is in the range of 10^{-5} to 10^{-2}.

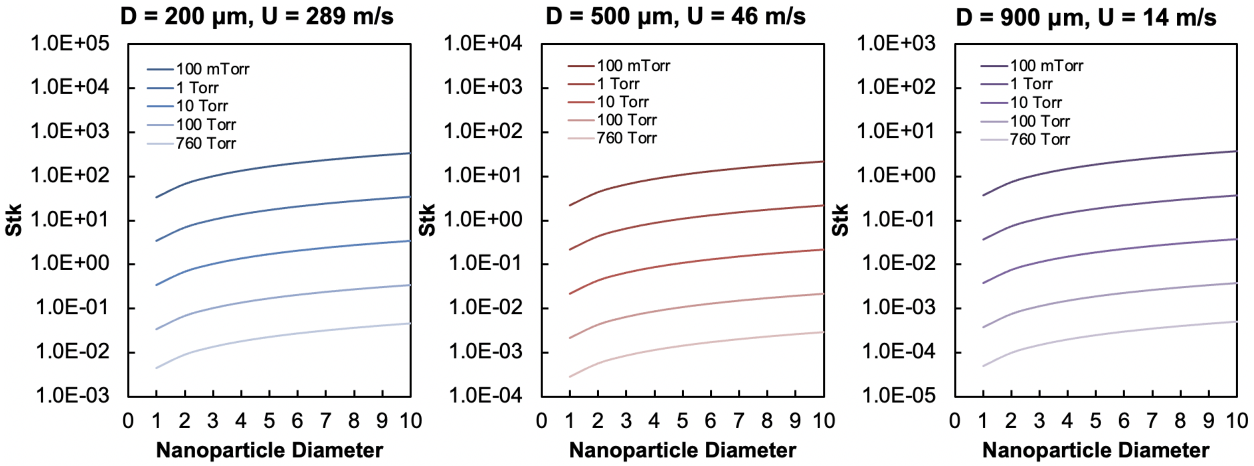

Figure 5.6: Plot displaying the interplay between nozzle diameter, flow velocity, pressure, and nanoparticle diameter on the Stokes number.

Qualitative verification of the Stk analysis was conducted through comparison of deposition at chamber pressures of 4 Torr and 760 Torr. The particle synthesis occurred at atmospheric pressure with argon flowrate of 250 sccm and silane flowrate of 5 sccm. Samples were collected on copper substrates with the reactor left stationary. Inspection of the image at 4 Torr shows that the impaction is sufficient to form tower-like structure with minimal spreading of deposition to other areas of the substrate. Increase of pressure to 760 Torr results in a flat spot with deposition scattered widely about the substrate indicating impaction does not occur as efficiently at higher pressure. The previous treatment of the Stk does not account for the pressure ratio between the upstream and downstream condtions, in the analysis the pressure reflects the change in the C_c as the mean free path changes. The pressure ratio is important because above a certain threshold ratio compressiblity effects become important to describe the drag force. The typical formulation of the Stokes number assumes that the Reynold's number is sufficiently small such that the drag force is Stokesian. When fluid speeds approach Mach (Ma) numbers of unity or greater, departure from the Stokes description of drag force occurs due to fluid compressibility. In general the typical form

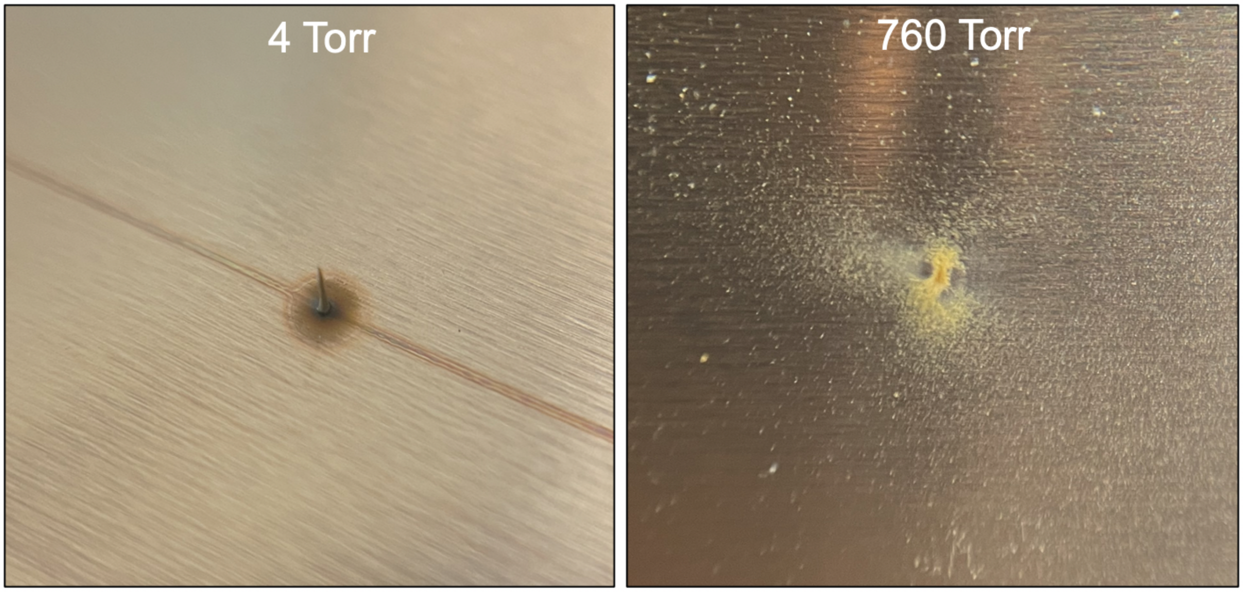

Figure 5.7: Difference in deposition of particles synthesized at the same conditions but deposited at chamber pressures of 4 Torr and 760 Torr.

of stokes drag underestimates the drag force as Ma increases. This indicates that for any given particle size the Stk of a particle will be decreased for a greater Ma. However there is a competing mechanism that can enhance impaction at Ma>1. When the flow is accelerated to the sonic limit within (Ma=1) the nozzle, the flow will expand upon exiting the nozzle this expansion results in further acceleration of the flow to Ma>1, downstream of the nozzle a Mach disk forms where the fluid velocity experiences a near instantaneous decrease in velocity to Ma<1. This phenomenon results in particles with speeds exceeding that of the fluid allowing for efficient impaction of small particles to occur due to the increased ratio of inertia to drag force.[120–122]

Improvements to impaction efficiency were also explored through the use of aerodynamic lenses. Such lenses have been described for use in low pressure systems for the collimation of the particulate phase in aerosol.[123, 124] Many geometries exist for lenses including single and multi stage thin plate orifices and converging-diverging nozzles. In either case the apparatus relies upon the Stk of the particles near the orifice or nozzle. When the flow is constricted and then allowed to expand it will do so more rapidly than the particles in the flow. This results in particles whose radial position is closer to the flow centerline after passing the constriction. In addition he Saffman force is important

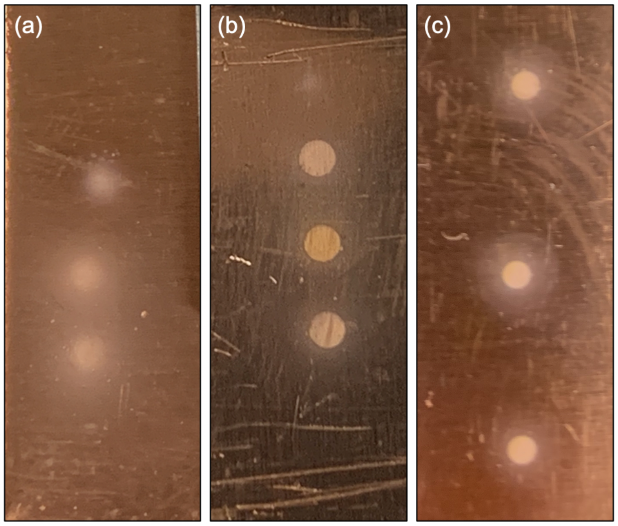

Figure 5.8: (a) Deposition of particles from straight ended tube with no intervention.(b) Deposition from straight ended tube with two aerodynamic lenses.(c) Deposition from straight ended tube with substrate biased by high voltage power supply.

to consider for flows constrained to sub-millimeter dimensions, this force results in migration of particles towards the centerline of the flow.[55, 125, 126] To examine such effects FLUENT was used to model the aerodynamic lenses described in the experimental section of this chapter. The simulation tracked particle positions as a function of radius from the centerline. Simplifications to the model were made by assuming flow was symmetric about the centerline of the tube. From the simulation it can be seen that particles final radial position is less than the initial position. Indicating that lensing effect is sufficient to aid in beam collimation.

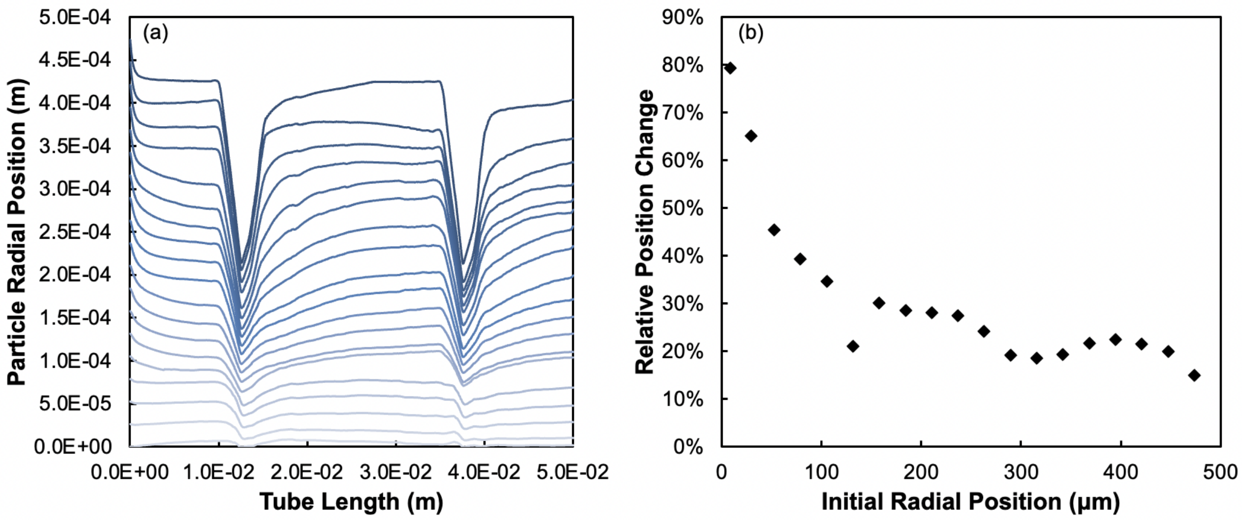

Figure 5.9: (a) Radial position of particles released at different initial radial positions as a function of the tube length.(b) Relative change between the initial and final radial position for each particle.

To corroborate the model samples were collected that recreated the model conditions. Samples were deposited with 250 sccm of argon, 5 sccm of silane with lenses created by pulling sections of a capillary tube. Samples were then collected onto copper substrates and imaged optically and with SEM. From the images it was observed that the deposition appeared less diffuse and the diameter of deposition decreased as the number of lenses increased. From inspection of SEM images there appeared to be little to no overspray with the lens approach.

The impaction of nanoparticles may also be modified by considering charge effects. Nanoparticles were deposited with a straight tube onto a biased copper substrate. Samples were deposited with 250 sccm of argon and 5 sccm of silane. The substrate voltage was varied from 6kV to 15 kV. Spots were deposited onto the substrate and then imaged and measured with SEM. A decreasing trend in spot diameter was observed from 1.33 to 1.24 mm as the voltage was increased. In

Sample	Lenses	Spot Diameter (mm)
1	0	1.37
2	1	1.35
3	2	1.28

Table 5.2: Table listing the number of aerodynamic lenses and associated diameter of spot deposition.

Sample	Voltage (kV)	Spot Diameter (mm)	Es
1	6	1.33	6.1
2	7	1.32	7.1
3	8	1.31	8.1
4	9	1.31	9.2
5	10	1.30	10.2
6	11	1.29	11.2
7	12	1.28	12.2
8	13	1.27	13.2
9	14	1.24	14.3

Table 5.3: Table listing the magnitude of the applied voltage and associated diameter of spot deposition.

comparison to the aerodynamic lens approach the region of overspray appeared much larger. From these samples the overspray region exhibited PL. For silicon nanoparticles to exhibit effecient PL it is necessary for quantum confinement to occur which requires the particle size to be below 5 nm. This suggests that the high voltage aided in capture of small nanoparticles. The use of an electric field on the substrate to capture particles is predicated upon the charge accumulation experienced by nanoparticles while in the plasma.[127] The accumulation of charge allows for electrical force to be exhibited onto the particles this increases the effective inertia of the particles by introducing a competing forcing to the fluid drag. Similar to the Stk number an electrostatic number[128] (Es) is defined as,

$$Es = \frac{\rho_p d_p^2 C_c U}{9\mu_f D} \tag{5.2}$$

which compares the electric force acting on the particle to the drag force. This number was calculated for the applied voltages and is listed in table 5.2.

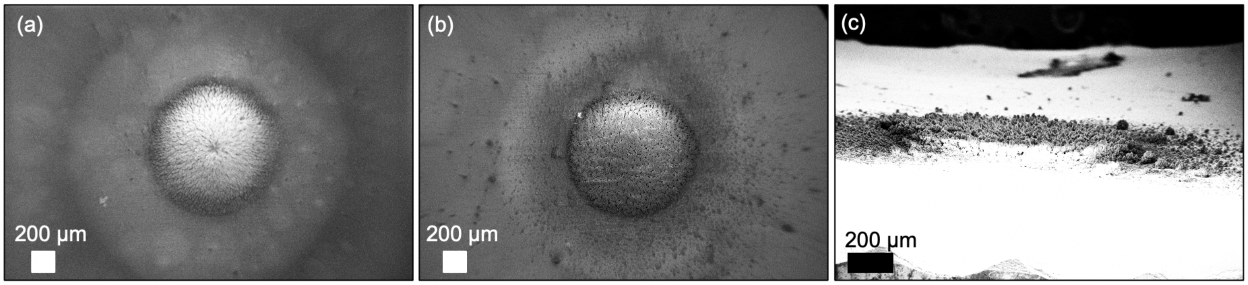

Figure 5.10: (a) SEM image of nanoparticles deposited with two aerodynamic lenses.(b) SEM image of nanoparticles deposited with substrate biased by high voltage power supply.(c) Cross sectional SEM image of nanoparticles deposited with substrate biased by high voltage power supply.

5.3.3 Spatially Varied Particle Printing

To examine the ability to control nanoparticle properties at the time of deposition a spatial study of particle crystallnity was performed. Synthesis conditions were 250 sccm of argon, 5 sccm of silane, and power was incremented by 20 W from 20 W to 80W. Particles were deposited onto a glass substrate in a 10 mm by 60 mm area. Every 15 mm the power was incremented by 20 W to create 4 sections with a unique synthesis power. The section were then analyzed with TEM, SAED, and XRD. Examination of the bright-field TEM images indicated an incresinga presence of crystalline particles. This was supported by dark-field images which showed an increasing number of bright spots as power was increased.

At 20 W of power SAED patterns indicated a small presence of crystalline material as evidenced by the presence of weak rings in the pattern. As power was increased the formation of more intense rings occurred in the SAED suggesting more crystalline particles were synthesized. The XRD pattern demonstrated the same trend as the SAED with power. At 20 W of power no diffraction peaks were present, as power was increased the intensity of the diffraction peaks increased indicating the presence of crystalline particles.

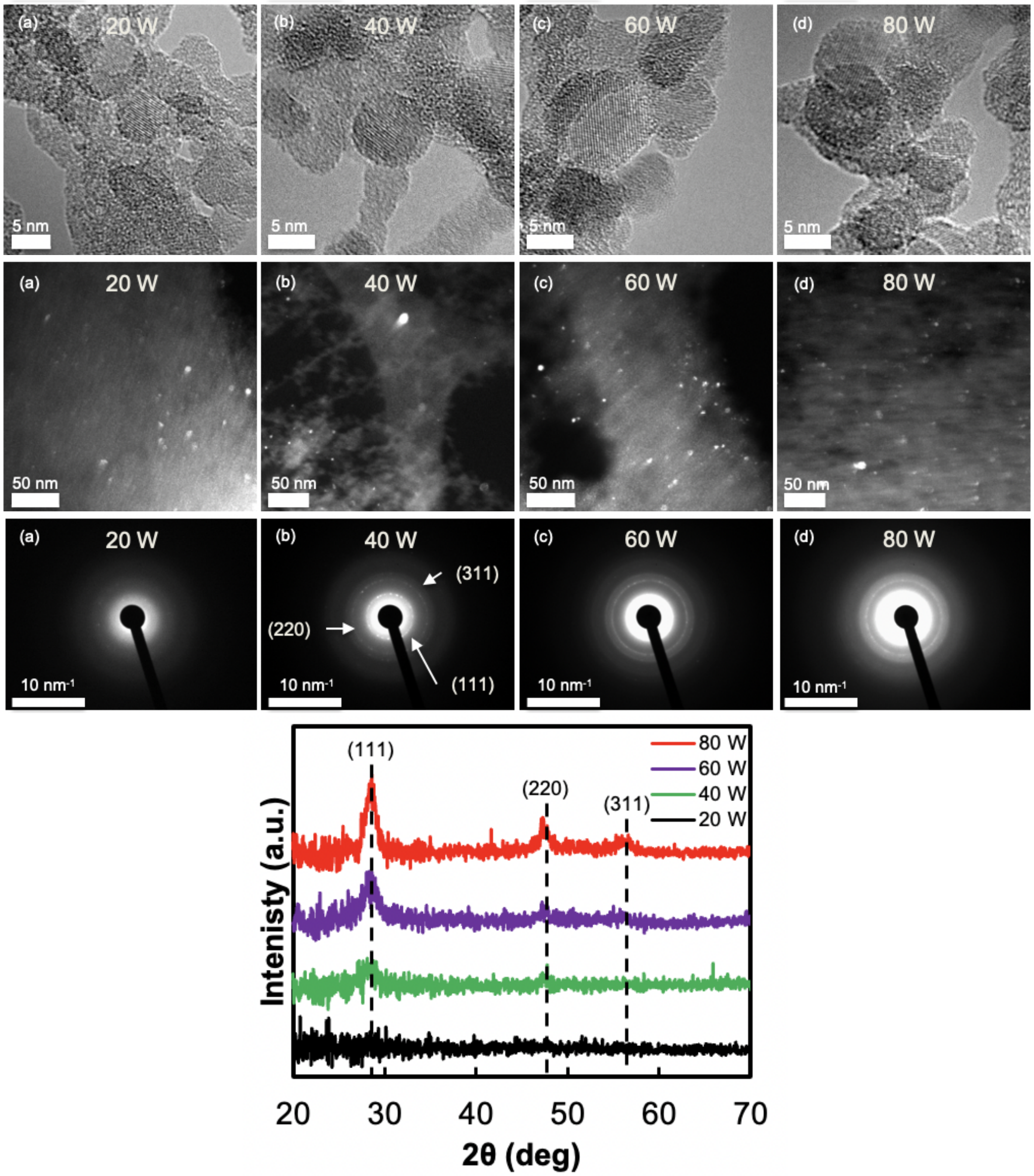

Figure 5.11: (Row 1) Bright-field TEM images of silicon nanoparticles synthesized at different powers.(Row 2) Dark-field TEM images of silicon nanoparticles synthesized at different powers.(Row 3) SAED patterns of silicon nanoparticles synthesized at different powers.(Row 4) XRD patterns of silicon nanoparticles synthesized at different powers.

5.4 Conclusions

The integrated process of atmospheric pressure plasma synthesis and aerosol jet printing without the use of solvent was demonstrated to be capable of depositing nanoparticles. The properties of the particles can be controlled in real time with corresponding spatial control of deposition. Resolution is on the order of 100 μm and overspray can be reduced with the use of aerodynamic lenses. Because of the high pressure, impaction efficiency of small particles is reduced. Impaction efficiency may be improved through further modification of the aerodynamics or by exploring electrical trapping of the particles.

CHAPTER 6

CONCLUSIONS AND FUTURE WORK

In this thesis methods for plasma based synthesis of nanoparticles were explored. Demonstrations of synthesis at both low pressure and atmospheric pressure were made. In both pressure regimes it was shown that nanoparticle size and crystallinity were modified through variation of synthesis parameters. While synthesis of GaN, InN, $In_xGa_{1-x}N$, and Si were directly explored the methods are not limited to these materials. Provided a vapor form of the appropriate precursor species can be utilized the methods can be extended to most materials. Integrated atmospheric pressure synthesis and dry aerosol jet printing of nanoparticles was also presented. This method allowed for real time control over nanoparticle properties and subsequent spatial control over the deposition properties.

6.1 Nitrides Synthesis

In this work successful demonstrations GaN, InN, and $In_xGa_{1-x}N$ have been made. Because these materials span from the UV to IR range of the spectrum they have potential to be used in optoelectronics. However there are number of issues that need to be addressed for the application space. First is the lack of PL from both GaN and InN. The absence of emission from the particle suggests that there are defects in the particles leading to non-radiative recombination. Since particles exhibit a crystalline core and they have a direct bandgap, defects at or near the particle surface may play a key role for PL. As described earlier EPR can be used for defect identification. EPR can be further used to quantify the relative change in defect concentration by comparison of the twice integrated EPR signal. From XPS data it was shown there exists an imbalance in the ratio of gallium to nitrogen and EPR indicated signal associated with nitrogen or gallium vacancies. Process conditions of precursor concentration or flowrate could be modified then with XPS and EPR could be used in conjunction to identify if changing stoichiometry effects the defect signal. Defects could arise from insufficient surface passivization, the use of hydrogen or ligands to passivate nanoparticle surfaces is a well established technique and could be attempted with a simple ligand exchange procedure. Another hypothesis for the suppressed PL is related to the crystal structure. The hexagonal crystal structure results in an internal electric field that increases the life time of charge carriers in the material, increasing the potential for interaction with defects. Synthesis of the cubic lattice would eliminate this internal electric field and may reduce the interaction of charge carriers with any defects. This would require detailed study of the relationship between the synthesis parameters, reaction environment, and resulting crystal structure. The study would also provide valuable information for general understating for selection of phase formation in RF plasmas.

Unlike InN and GaN, $In_xGa_{1-x}N$ exhibits PL - however identification of the relative amounts of gallium and indium in the lattice has been difficult to ascertain. This issue is complicated by the methods of detection. To allow identification of composition with Vegard's law and XRD; experiments where particle size is made sufficiently large to reduce size broadening of the diffraction peaks would allow for the law to be applied with far less ambiguity. To increase particle size longer residences times or pulsed power could be used. Composition can also be estimated with Vegard's law by measuring the bandgap.

6.2 Atmospheric Pressure Synthesis

Atmospheric pressure synthesis was used to successfully synthesize silicon nanoparticles with ambient air surroundings. The particles developed an oxide shell while maintaining a crystalline silicon core. The current process has a throughput on the order of micrograms per minute whereas low pressure synthesis is capable of throughput at milligrams per minute.To increase throughput it would be beneficial to determine methods to mitigate film formation on the reactor walls. Such methods may include the introduction of a sheath flow. Throughput could be increased through parallel operation of reactors or scaling to larger reactors.

6.3 Nanoparticle Printing

Nanoaprticle printing was achieved by combining atmospheric pressure plasma synthesis and aerosol jet printing into a single process. The technique while functional requires further improvement. The primary objective that should be met is raising the impaction efficiency of small nanoparticles. A simple method would be to decrease the pressure around the reactor outlet and substrate however this reintroduces the need for pumps and associated vacuum equipment. Further Brownian motion of small nanoparticles at low pressure limits the resolution of the printing process. Alternatively performing synthesis at pressures 2 to 3 times atmospheric pressure would enable sonic flow at the nozzle throat leading to supersonic flow speeds upon flow expansion. Such flows possess the ability to deposit nanoparticles and because of the high pressure diffusion is greatly suppressed.

APPENDICES

APPENDIX A

POWER DENSITY MEASUREMENT AND CALCULATION

Measurement of the power absorbed by the plasma discharge is not a trivial task. Because the circuit used to power an RF plasma has a complex impedance large amounts of power can be reflected in the circuit and not reach the load (plasma). For a typical RF plasma configuration the circuit is composed of a power supply, impedance matching network, the plasma, transmission lines, and associated connectors and adaptors. Contact losses between transmission lines (typically coaxial cable) and circuit elements are unavoidable but the number of connections should be minimized to avoid unnecessary power losses. Transmission lines should be kept as short as possible less than 1/4 of the power signal's wavelength to avoid the impedance of the line acting in a deleterious manner and to reduce resistive losses. The impedance matching network is a critical element of the circuit that "matches" the impedance impedance of the source to the load through capacitors and inductors. Often matching networks are termed lossless because they use circuit elements that store energy (capacitors and inductors) but not elements that dissipate energy (resistors) in reality all elements in the circuit will dissipate some energy. Many matching networks for capacitively coupled plasmas (CCP) inlcude an inductor coil. This coil is often cited as the element that causes the most power dissipation in the matcher. To minimize losses from the inductor the smallest amount of inductance necessary should be used. The output of the matching network is often followed by another section of transmission line connected to electrodes for the plasma discharge. Power measurements are divided into forward power and reflected power. Forward power is the amount of power delivered to the load whereas reflected power is the power reflected back to the supply. Power measurements are often taken at the power supply this however can lead to errors in the actual power delivered to the plasma in particular when the current and voltage are out of phase with each other. For a capacitive discharge the power absorbed by the plasma may be evaluated with the following subtractive method.

1. Measure voltage across the discharge electrodes (V_{RF}) with a plasma present and measure the source power (P_{on}).
2. Extinguish the plasma and adjust the source power (P_{off})until the voltage V_{RF} measured in step 1 is reached.
3. The power absorbed by the plasma (P_{plasma}) is in the difference in between the power measurements of step 1 and 2.

$$P_{plasma} = P_{on} - P_{off} \tag{A.1}$$

For further description please refer to the work of Godyak.[129, 130]

Often when operating plasmas for nanoparticle synthesis accurate estimation of the power density is often not needed rather maximal power transfer is desired to avoid extinguishing of plasma during or heating of reactor tube. In this case a voltage proxy measurement may be used to provide directional information related to power transfer. Consider the simple case of two charged parallel plates the electric field strength is proportional to the voltage between the electrodes. Recall that the nonthermal plasma is driven by the strength of the electric field. Thus maximizing the voltage across the electrodes will aid in ignition and sustained operation of the plasma. The voltage proxy method can be used by comparing the source voltage to the voltage across the plasma electrodes. While the proxy method overestimates the power transfer it has the same directional relationship of power transfer as the subtractive method.

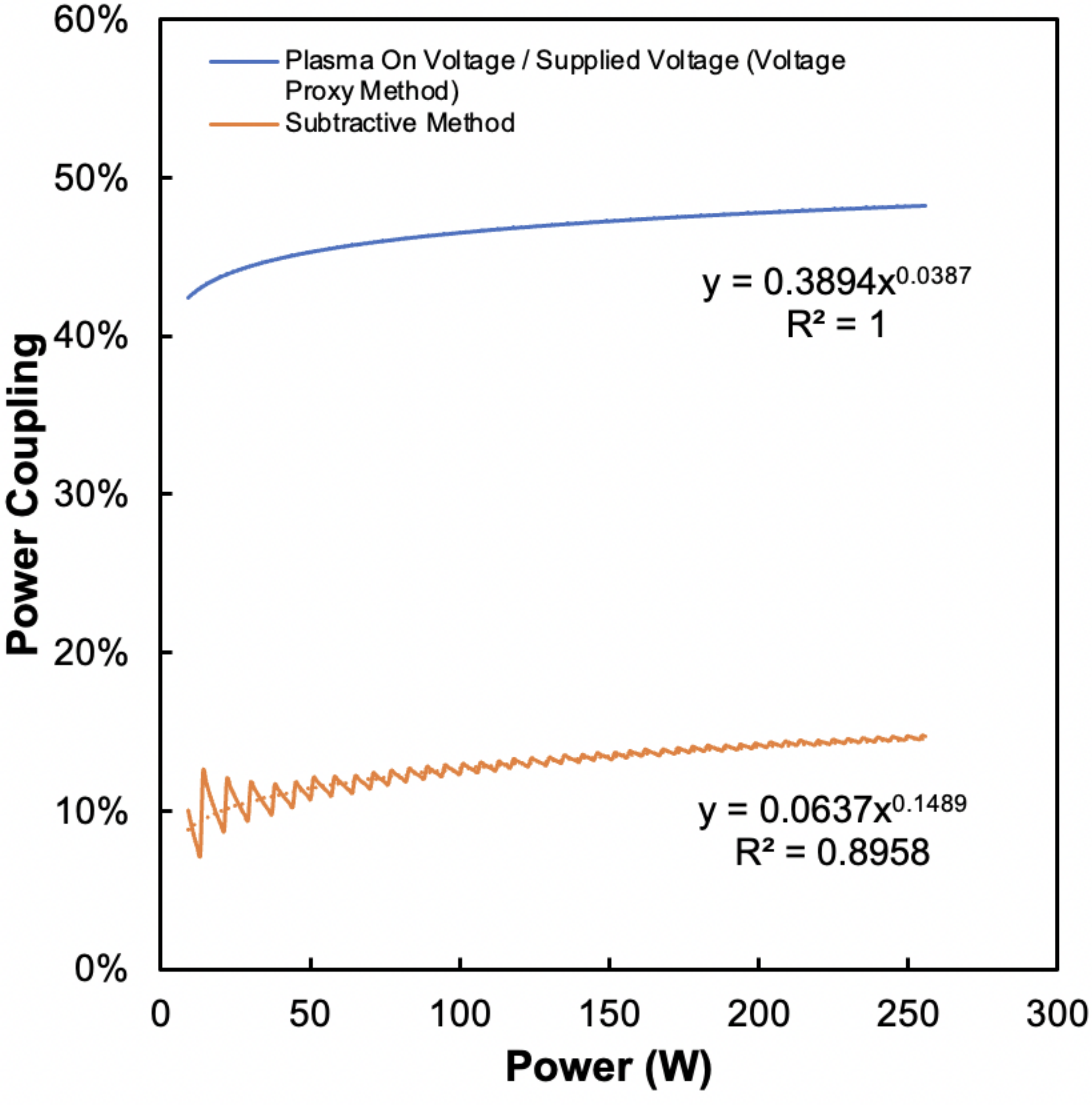

Figure A.1: Comparison of voltage proxy and subtractive method for power transfer estimation.

APPENDIX B

FLOW ANALYSIS

Nanoparticle transport and impaction is influenced by many parameters here basic equations and relevant non-dimensional numbers are described. For an introduction to the fundamentals of nanoaprticle transport refer to the work of Madler and Friedander.[131] As disscused in the main body of the text the Stk is an important number for describing the likelihood of particle impaction. Recall that the Stk is defined as the ratio of the particle inertia to the drag force acting upon the particle.

$$Stk = \frac{F_i}{F_D} = \frac{\rho_p d_p^2 C_c U_m}{9\mu_f D} \tag{B.1}$$

- F_i Particle Inertia
- F_D Drag Force
- ρ_p Mass density of particle
- d_p Particle diameter
- C_c Cunningham slip correction factor
- U_m Mean speed of flow
- μ_f Dynamic viscosity of fluid
- D Characteristic length (Nozzle diameter)

C_c is defined by the following equation,

$$C_c = 1 + \frac{2\lambda}{d_p}[A_1 + A_2 e^{\frac{-A_3 d_p}{\lambda}}] \tag{B.2}$$

The equation can be simplified fromd efeintion of the particle Knudsen number,

$$Kn_p = \frac{2\lambda}{r_p} \tag{B.3}$$

Where r_p is the particle radius. This results in the following expression for C_c,

$$C_c = 1 + Kn(A_1 + A_2 e^{\frac{-2A_3}{Kn}}) \tag{B.4}$$

The coefficients A_1, A_2, and A_3 are empirically.[132] λ is the gas mean free path which is given by the following relationship.

$$\lambda = \frac{\mu_f}{P}(\frac{\pi RT}{2M})^{1/2} \tag{B.5}$$

- μ_f Gas dynamic viscosity
- P Pressure
- R Universal gas constant
- T Gas temperature
- M Molecular weight

Nanoparticle transport may also be influenced by diffusion. The Peclet number (Pe) is used to describe the ratio of advection to diffusion. When the Pe is large effects of diffusion are limited whereas when the Pe is small diffusion should be considered. For background again refer to Madler and Friednder.[131]

$$Pe = \frac{Lu}{D} \tag{B.6}$$

- L Characteristic length
- u Local flow velocity
- D Mass diffusion coefficient

The mass diffusion is obtained from the following,

$$D = \frac{\kappa T}{\zeta} \tag{B.7}$$

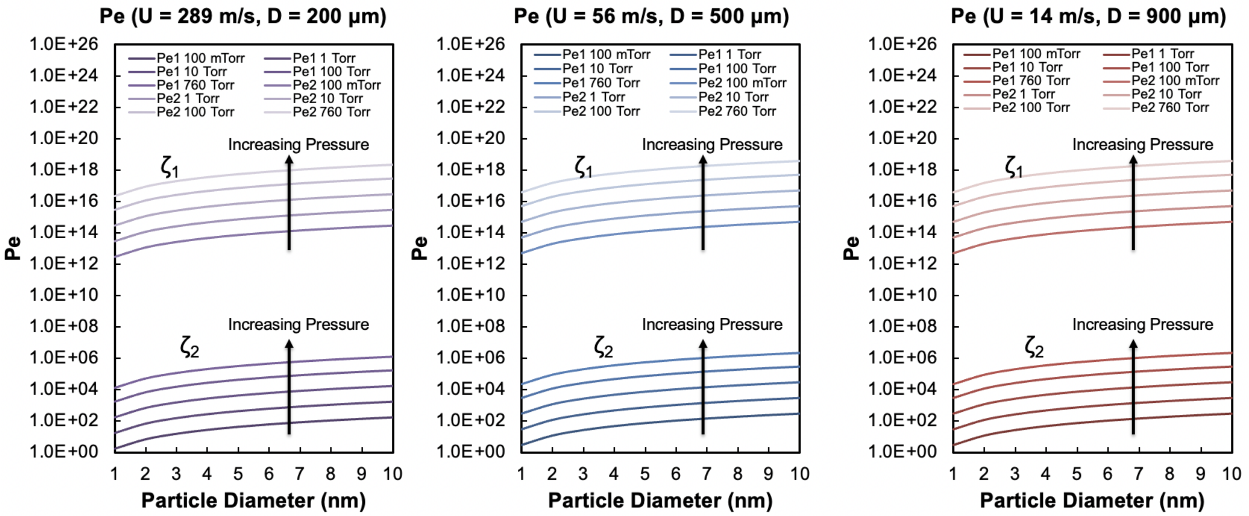

Figure B.1: Plots of Pe for different gas flow velocities and pressures. Pe is plotted for both calculations of the friction coefficient.

- k Boltzmann constant
- T Temperature
- ζ Friction coefficient

The friction coefficient for large particles can be found from the following relationship.

$$\zeta_1 = \frac{3\pi\mu_f d_p}{C_c} \tag{B.8}$$

The friction coefficient for small particles (Kn»1) can be found from the following relationship.

$$\zeta_2 = \frac{2}{3} d_p^2 \rho_f \sqrt{\frac{2\pi\kappa T}{m_f}} \left(1 + \frac{\pi\alpha}{8}\right) \tag{B.9}$$

- α Accommodation coefficient
- ρ_f Gas density
- m_f Mass of gas molecule

The accommodation coefficient is experimentally determined but is often near 0.9.[131]

Discussion of transport would be incomplete without considering effects of compressible flow, such effects include changes to calculation of drag force and changes in the flow field. The previous analysis considers the flow to be incompressible however deviation from this assumption can easily be encountered. Incompressible flow relies upon the assumption that the density of the fluid remains constant. This assumption breaks down for Mach numbers (Ma) on the order of or greater than unity (often Ma greater than 0.3 is considered the onset of compressible flow). The Ma expresses the ratio of the fluid speed (U) to the speed of sound of the fluid (U_s).

$$Ma = U/U_s \tag{B.10}$$

An important compressiblity effect is choked flow. Choked flow describes the limiting of flow velocity when passing through an orifice plate or throat of a nozzle. The flow is limited to a Ma of 1 at the location of the flow constriction. There exists a minimum pressure ratio at which choked flow will occur, increases of the pressure ratio result in change of mass flow rate but not a change in flow velocity. This pressure ratio is calculated with the following equation.

$$\frac{P_d}{P_u} = \frac{2}{\gamma + 1}^{\frac{\gamma}{\gamma - 1}} \tag{B.11}$$

- P_d Pressure downstream of constriction
- P_u Pressure upstream of constriction
- γ Heat capacity ratio of fluid

When the pressure ratio is sufficiently high the flow will expand after passing the flow constriction and a resulting acceleration of the flow will occur as the density of the fluid changes. The expansion of the jet results in a flow field that may allows for efficient impaction of nanoparticles.[133] At the nozzle throat the velocity of the flow will be limited to a Ma of 1, after the flow passes the nozzle throat the jet expands and there will exist a Mach disk downstream of the nozzle where the gas velocity experiences a near step function decrease in flow velocity. The decrease in velocity is accompanied by a decease of the drag force on the particles. Particles may experience far less deceleration than the gas when passing through the Mach disk because of the small time interval. The location of the Mach disk may shift if flow impinges upon a surface downstream of the nozzle.

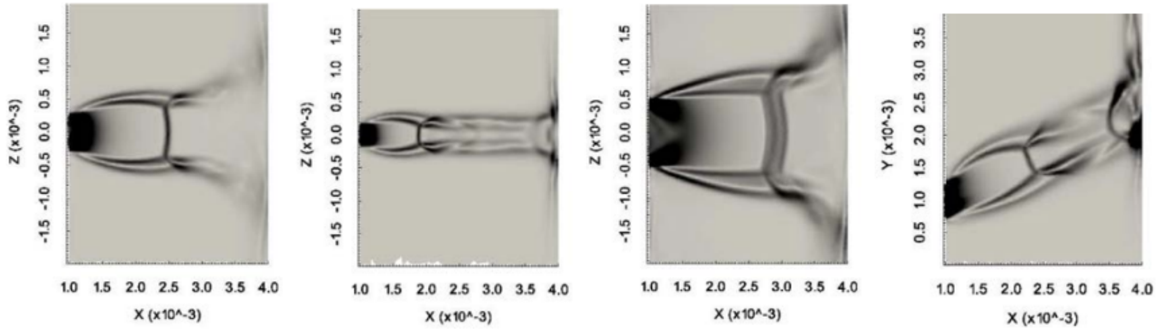

(a) D5 (b) D28 (c) D1 (d) Y45

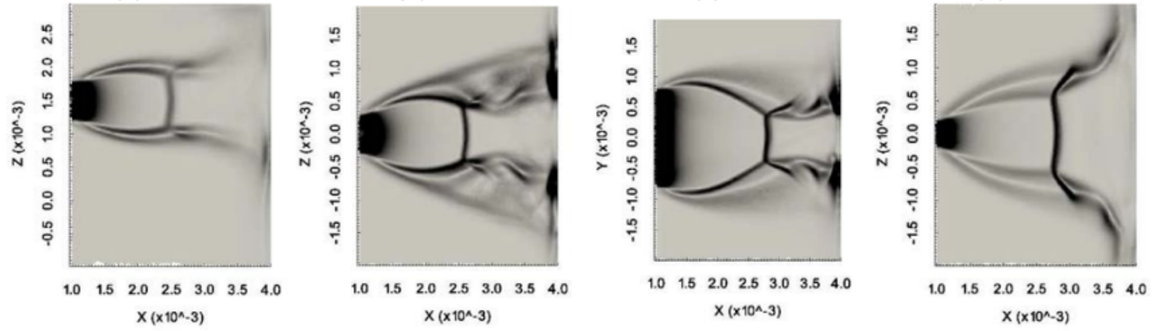

(e) Z15 (f) SC (g) SR (Length direction) (h) SR (Width direction)

Figure B.2: Schlieren images of jets impinging upon substrates.[4]

This requires careful consideration of substrate location to make use of this effect for nanoparticle deposition.

BIBLIOGRAPHY

BIBLIOGRAPHY

[1] Richard K. Ahrenkiel and S. Phil Ahrenkiel. *Theory and methods of photovoltaic material characterization: Optical and electrical measurement techniques*, volume 13. 2019.

[2] Marina Brustolon and Elio Giamello. *ELECTRON PARAMAGNETIC RESONANCE A Practitioner's Toolkit*. 1999.

[3] J. Ross and M. Rubin. High-quality GaN grown by reactive sputtering. *Materials Letters*, 12(4):215–218, nov 1991.

[4] F. Chen, A. Allou, Q. Douasbin, L. Selle, and J. D. Parisse. Influence of straight nozzle geometry on the supersonic under-expanded gas jets. *Nuclear Engineering and Design*, 339:92–104, 2018.

[5] Usman Ahmad, Samia Aslam, Faiza Mustafa, Ayesha Jamil, and Muhammad Ashfaq Ahmad. Synthesis and characterization of InN quantum dots for optoelectronic applications. *Optik*, 173:97–100, nov 2018.

[6] Jason Baxter, Zhixi Bian, Gang Chen, David Danielson, Mildred S. Dresselhaus, Andrei G. Fedorov, Timothy S. Fisher, Christopher W. Jones, Edward Maginn, Uwe Kortshagen, Arumugam Manthiram, Arthur Nozik, Debra R. Rolison, Timothy Sands, Li Shi, David Sholl, and Yiying Wu. Nanoscale design to enable the revolution in renewable energy. *Energy and Environmental Science*, 2(6):559–588, 2009.

[7] Andrey L. Rogach, Nikolai Gaponik, John M. Lupton, Cristina Bertoni, Diego E. Gallardo, Steve Dunn, Nello Li Pira, Marzia Paderi, Piermario Repetto, Sergei G. Romanov, Colm O'Dwyer, Clivia M. Sotomayor Torres, and Alexander Eychmüller. Light-emitting diodes with semiconductor nanocrystals. *Angewandte Chemie - International Edition*, 47(35):6538–6549, aug 2008.

[8] Vanessa Wood and Vladimir Bulović. Colloidal quantum dot light-emitting devices. *Nano Reviews*, 1(1):5202, jan 2010.

[9] Moon Sung Kang, Chul Ho Lee, Jun Beom Park, Hyobin Yoo, and Gyu Chul Yi. Gallium nitride nanostructures for light-emitting diode applications. *Nano Energy*, 1(3):391–400, may 2012.

[10] Nathan J. Castro, Joseph O'Brien, and Lijie Grace Zhang. Integrating biologically inspired nanomaterials and table-top stereolithography for 3D printed biomimetic osteochondral scaffolds. *Nanoscale*, 7(33):14010–14022, 2015.

[11] Xiao Li and Xinyu Liu. Group III nitride nanomaterials for biosensing. *Nanoscale*, 9(22):7320–7341, jun 2017.

[12] Didier Astruc. Introduction: Nanoparticles in Catalysis. *Chemical Reviews*, 120(2):461–463, jan 2020.

[13] Ekaterina Pomerantseva, Francesco Bonaccorso, Xinliang Feng, Yi Cui, and Yury Gogotsi. Energy storage: The future enabled by nanomaterials. *Science*, 366(6468), nov 2019.

[14] Darrah Johnson-Mcdaniel, Christopher A. Barrett, Asma Sharafi, and Tina T. Salguero. Nanoscience of an ancient pigment. *Journal of the American Chemical Society*, 135(5):1677–1679, feb 2013.

[15] Delphine Schaming and Hynd Remita. Nanotechnology: from the ancient time to nowadays. *Foundations of Chemistry*, 17(3):187–205, jul 2015.

[16] Michael Faraday. X. The Bakerian Lecture. —Experimental relations of gold (and other metals) to light. *Philosophical Transactions of the Royal Society of London*, 147:145–181, dec 1857.

[17] Uwe Kortshagen. Nonthermal Plasma Synthesis of Nanocrystals: Fundamentals, Applications, and Future Research Needs, 2016.

[18] L. Mangolini, E. Thimsen, and U. Kortshagen. High-yield plasma synthesis of luminescent silicon nanocrystals. *Nano Letters*, 5(4):655–659, 2005.

[19] X. D. Pi and U. Kortshagen. Nonthermal plasma synthesized freestanding silicon-germanium alloy nanocrystals. *Nanotechnology*, 20(29), 2009.

[20] Alexander Ho, Rajib Mandal, Richard R. Lunt, and Rebecca J. Anthony. Nonthermal Plasma Synthesis of Gallium Nitride Nanoparticles: Implications for Optical and Electronic Applications. *ACS Applied Nano Materials*, 4(6):5624–5629, jun 2021.

[21] Alejandro Alvarez Barragan, Niranjan V. Ilawe, Lanlan Zhong, Bryan M. Wong, and Lorenzo Mangolini. A Non-Thermal Plasma Route to Plasmonic TiN Nanoparticles. *Journal of Physical Chemistry C*, 121(4):2316–2322, 2017.

[22] Lorenzo Mangolini and Uwe Kortshagen. *Nonthermal Plasma Synthesis of Silicon Nanocrystals*. 2010.

[23] Ethan B. Secor. Principles of aerosol jet printing. *Flexible and Printed Electronics*, 3(3), 2018.

[24] A. L. Patterson. The scherrer formula for X-ray particle size determination. *Physical Review*, 56(10):978–982, 1939.

[25] C.J. Gilmore, J. A. Kaduk, and H. Schenk. *International Tables for Crystallography*, volume H. 2019.

[26] G. K. Williamson and W. H. Hall. X-ray line broadening from filed aluminium and wolfram. *Acta Metallurgica*, 1(1):22–31, jan 1953.

[27] B. E. Warren and B. L. Averbach. The separation of cold-work distortion and particle size broadening in x-ray patterns [1]. *Journal of Applied Physics*, 23(4):497, 1952.

[28] Vitalij K. Pecharsky and Peter Y. Zavalij. Fundamentals of powder diffraction and structural characterization of materials. *Fundamentals of Powder Diffraction and Structural Characterization of Materials*, pages 1–741, 2005.

[29] Enrico Mignaioli, Giancarlo Capitani, Fernando Nieto, and Marcello Mellini. Accurate and precise lattice parameters by selected-area electron diffraction in the transmission electron microscope. *American Mineralogist*, 94(5-6):793–800, 2009.

[30] J. O. Malm and M. A. O'Keefe. Deceptive 'lattice spacings' in high-resolution micrographs of metal nanoparticles. *Ultramicroscopy*, 68(1):13–23, may 1997.

[31] S. C.Y. Tsen, P. A. Crozier, and J. Liu. Lattice measurement and alloy compositions in metal and bimetallic nanoparticles. *Ultramicroscopy*, 98(1):63–72, dec 2003.

[32] W. J. de Ruijter, R. Sharma, M. R. McCartney, and David J. Smith. Measurement of lattice-fringe vectors from digital HREM images: experimental precision. *Ultramicroscopy*, 57(4):409–422, mar 1995.

[33] Jessica Nannini. The Nobel Prize in Physics 2014, oct 2014.

[34] Shuji Nakamura and M. R. Krames. History of gallium-nitride-based light-emitting diodes for illumination. *Proceedings of the IEEE*, 101(10):2211–2220, oct 2013.

[35] M. H. Kane and N. Arefin. Gallium nitride (GaN) on silicon substrates for LEDs. *Nitride Semiconductor Light-Emitting Diodes (LEDs): Materials, Technologies and Applications*, pages 99–143, jan 2013.

[36] Abhiram Gundimeda, Shibin Krishna, and Neha Aggarwal. Cite as. *Appl. Phys. Lett*, 110:103507, 2017.

[37] M. A. Qaeed, K. Ibrahim, K. M.A. Saron, and A. Salhin. Optical and structural properties of indium nitride nanoparticles synthesized by chemical method at low temperature. *Solar Energy*, 97:614–619, nov 2013.

[38] Sandra Ruffenach, Matthieu Moret, Olivier Briot, and Bernard Gil. Recent advances in the MOVPE growth of indium nitride. *physica status solidi (a)*, 207(1):9–18, jan 2010.

[39] Burak Tekcan, Sabri Alkis, Mustafa Alevli, Nikolaus Dietz, Bulend Ortac, Necmi Biyikli, and Ali Kemal Okyay. A near-infrared range photodetector based on indium nitride nanocrystals obtained through laser ablation. *IEEE Electron Device Letters*, 35(9):936–938, 2014.

[40] Nikos Chaniotakis and Nikoletta Sofikiti. Novel semiconductor materials for the development of chemical sensors and biosensors: A review. *Analytica Chimica Acta*, 615(1):1–9, may 2008.

[41] Ashraful Ghani Bhuiyan, Akihiro Hashimoto, and Akio Yamamoto. Indium nitride (InN): A review on growth, characterization, and properties ARTICLES YOU MAY BE INTERESTED IN. *Journal of Applied Physics*, 94:2779, 2003.

[42] Anthony C. Jones, Colin R. Whitehouse, and John S. Roberts. Chemical approaches to the Metalorganic CVD of Group-III Nitrides. *Chemical Vapor Deposition*, 1(3):65–74, nov 1995.

[43] Stacia Keller, Haoran Li, Matthew Laurent, Yanling Hu, Nathan Pfaff, Jing Lu, David F Brown, Nicholas A Fichtenbaum, James S Speck, Steven P Denbaars, and Umesh K Mishra. Recent progress in metal-organic chemical vapor deposition of N-polar group-III nitrides. *Semicond. Sci. Technol*, 29:113001, 2014.

[44] Necmi Biyikli and Ali Haider. Atomic layer deposition: an enabling technology for the growth of functional nanoscale semiconductors Atomic layer deposition: an enabling technology for the growth of functional nanoscale semiconductors. *Semiconductor Science and Technology Semicond. Sci. Technol*, 32:52, 2017.

[45] Rebecca Joy Anthony, Elijah Thimsen, Joe Johnson, Stephen A Campbell, and Uwe Kortshagen. Fast High-Density Low-Pressure Plasma Synthesis of GaN Nanocrystals. *MRS Proceedings*, 892, 2005.

[46] Necip B. Uner, Dariusz M. Niedzwiedzki, and Elijah Thimsen. Nonequilibrium Plasma Aerotaxy of InN Nanocrystals and Their Photonic Properties. *Journal of Physical Chemistry C*, 123(50):30613–30622, 2019.

[47] Necip B. Uner and Elijah Thimsen. Nonequilibrium plasma aerotaxy of size controlled GaN nanocrystals. *Journal of Physics D: Applied Physics*, 53(9):095201, dec 2020.

[48] Manabu Shimada, Yasushi Azuma, Kikuo Okuyama, Yutaka Hayashi, and Eiji Tanabe. Plasma synthesis of light emitting gallium nitride nanoparticles using a novel microwave-resonant cavity. *Japanese Journal of Applied Physics, Part 1: Regular Papers and Short Notes and Review Papers*, 45(1 A):328–332, 2006.

[49] Jennifer C. Hsieh, Dong Soo Yun, Evelyn Hu, and Angela M. Belcher. Ambient pressure, low-temperature synthesis and characterization of colloidal InN nanocrystals. *Journal of Materials Chemistry*, 20(8):1435–1437, 2010.

[50] Balaji Manavaimaran and Sivasankaran B. Ravichandran. GaN and InGaN Based Nanocomposites for Ammonia Gas Sensing Applications. *physica status solidi (b)*, 259(2):2100362, feb 2022.

[51] N. J. Kramer, R. J. Anthony, M. Mamunuru, E. S. Aydil, and U. R. Kortshagen. Plasma-induced crystallization of silicon nanoparticles. *Journal of Physics D: Applied Physics*, 47(7), 2014.

[52] Z. C. Holman and U. R. Kortshagen. A flexible method for depositing dense nanocrystal thin films: Impaction of germanium nanocrystals. *Nanotechnology*, 21(33), 2010.

[53] Michael A. Reshchikov and Hadis Morko. Luminescence properties of defects in GaN. *Journal of Applied Physics*, 97(6), 2005.

[54] B. Giroire, S. Marre, A. Garcia, T. Cardinal, and C. Aymonier. Continuous supercritical route for quantum-confined GaN nanoparticles. *Reaction Chemistry and Engineering*, 1(2):151–155, 2016.

[55] Corrigendum: Comparison of three dielectric barrier discharges regarding their physical characteristics and influence on the adhesion properties of maple, high density fiberboard and wood plastic composite (Journal of Physics D: Applied Physics (2017) 50 . *Journal of Physics D: Applied Physics*, 51(15), 2018.

[56] P. J. Bruggeman, N. Sadeghi, D. C. Schram, and V. Linss. Gas temperature determination from rotational lines in non-equilibrium plasmas: A review. *Plasma Sources Science and Technology*, 23(2):32, 2014.

[57] Fei Chen, Xiaohong Ji, and Shu Ping Lau. Recent progress in group III-nitride nanostructures: From materials to applications. *Materials Science and Engineering R: Reports*, 142:100578, oct 2020.

[58] Hailin Qiu, Chuanbao Cao, and Hesun Zhu. Synthesis of nanocrystalline GaN by the sol-gel method. *Materials Science and Engineering B: Solid-State Materials for Advanced Technology*, 136(1):33–36, 2007.

[59] Manabu Shimada, Wei Ning Wang, and Kikuo Okuyama. Synthesis of gallium nitride nanoparticles by microwave plasma-enhanced CVD. *Chemical Vapor Deposition*, 16(4-6):151–156, jun 2010.

[60] Jong Won Yoon, Takeshi Sasaki, Cheong Hyun Roh, Seung Hwan Shim, Kwang Bo Shim, and Naoto Koshizaki. Quantum confinement effect of nanocrystalline GaN films prepared by pulsed-laser ablation under various Ar pressures. *Thin Solid Films*, 471(1-2):273–276, jan 2005.

[61] Lei Zhang, Shouzhi Wang, Yongliang Shao, Yongzhong Wu, Changlong Sun, Qin Huo, Baoguo Zhang, Haixiao Hu, and Xiaopeng Hao. One-step fabrication of porous GaN crystal membrane and its application in energy storage. *Scientific Reports*, 7, 2017.

[62] Donald R Baer, Kateryna Artyushkova, C Richard Brundle, James E Castle, Mark H Engelhard, Karen J Gaskell, John T Grant, Richard T Haasch, Matthew R Linford, Alexander G Shard, Peter M A Sherwood, and Vincent S Smentkowski. Practical Guides for X-Ray Photoelectron Spectroscopy (XPS): First Steps in planning, conducting and reporting XPS measurements. *J Vac Sci Technol A*, 37, 2019.

[63] V. Ganesh, S. Suresh, M. Balaji, and K. Baskar. Synthesis and characterization of nanocrystalline gallium nitride by nitridation of Ga-EDTA complex. *Journal of Alloys and Compounds*, 498(1):52–56, 2010.

[64] Hong Di Xiao, Hong Lei Ma, Cheng Shan Xue, Hui Zhao Zhuang, Jin Ma, Fu Jian Zong, and Wen Rong Hu. Thermal oxidation behaviors of GaN powders. *Materials Letters*, 59(29-30):4041–4043, 2005.

[65] B. Deb, A. Ganguly, S. Chaudhuri, B. R. Chakraborti, and A. K. Pal. Synthesis of wurtzite GaN films by reactive hot wall vapour deposition technique: Fabrication of Au/GaN Schottky diode. *Materials Chemistry and Physics*, 74(3):282–288, 2002.

[66] David Kisailus, Joon Hwan Choi, and F. F. Lange. GaN nanocrystals from oxygen and nitrogen-based precursors. Technical Report 1-2, 2003.

[67] C. J. Linnen and R. D. Coombe. Mechanism of the photochemically induced reaction between Ga(CH3)3 and HN3 and the deposition of GaN films. Technical Report 1, 1998.

[68] Urszula Szałaj, Anna Świderska-Ś Sroda, Agnieszka Chodara, Stanisław Gierlotka, and Witold Łojkowski. Nanoparticle size effect on water vapour adsorption by hydroxyapatite. *Nanomaterials*, 9(7), jul 2019.

[69] Sreekar Bhaviripudi, Jifa Qi, Evelyn L. Hu, and Angela M. Belcher. Synthesis, characterization, and optical properties of ordered arrays of III-nitride nanocrystals. *Nano Letters*, 7(11):3512–3517, 2007.

[70] O. I. Mićić, S. P. Ahrenkiel, D. Bertram, and A. J. Nozik. Synthesis, structure, and optical properties of colloidal GaN quantum dots. *Applied Physics Letters*, 75(4):478–480, 1999.

[71] Juan Hao, Sijia Xu, Bingrong Gao, and Lingyun Pan. PL tunable GaN nanoparticles synthesis through femtosecond pulsed laser ablation in different environments. *Nanomaterials*, 10(3):439, feb 2020.

[72] C. Haller, J. F. Carlin, G. Jacopin, W. Liu, D. Martin, R. Butté, and N. Grandjean. GaN surface as the source of non-radiative defects in InGaN/GaN quantum wells. *Applied Physics Letters*, 113(11):111106, sep 2018.

[73] K Nakamoto. *Infrared and raman spectra of inorganic and coordiation compounds*. 3 edition, 1978.

[74] M. Alevli, R. Atalay, G. Durkaya, A. Weesekara, A. G. U. Perera, N. Dietz, R. Kirste, and A. Hoffmann. Optical characterization of InN layers grown by high-pressure chemical vapor deposition. *Journal of Vacuum Science Technology A: Vacuum, Surfaces, and Films*, 26(4):1023–1026, 2008.

[75] M. Jothibas, C. Manoharan, S. Ramalingam, S. Dhanapandian, S. Johnson Jeyakumar, and M. Bououdina. Preparation, characterization, spectroscopic (FT-IR, FT-Raman, UV and visible) studies, optical properties and Kubo gap analysis of In2O3 thin films. *Journal of Molecular Structure*, 1049:239–249, oct 2013.

[76] Sheetal J. Patil, Dhananjay S. Bodas, A. B. Mandale, and S. A. Gangal. Characterization of indium nitride films deposited by activated reactive evaporation process. *Thin Solid Films*, 444(1-2):52–57, nov 2003.

[77] Aseel A. Hadi, Juhaina M. Taha, Khawla S. Khashan, and Sarah F. Abbas. Preparation and characterization of InN NPs by laser ablation in ammonium solution. *AIP Conference Proceedings*, 2213:20308, 2020.

[78] Tanveer Ahmad and Dongdong Zhang. A critical review of comparative global historical energy consumption and future demand: The story told so far. *Energy Reports*, 6:1973–1991, nov 2020.

[79] W. H. Ho and S. K. Yen. Preparation and characterization of indium oxide film by electrochemical deposition. *Thin Solid Films*, 498(1-2):80–84, mar 2006.

[80] A. Yahia, A. Attaf, H. Saidi, M. Dahnoun, C. Khelifi, A. Bouhdjer, A. Saadi, and H. Ezzaouia. Structural, optical, morphological and electrical properties of indium oxide thin films prepared by sol gel spin coating process. *Surfaces and Interfaces*, 14:158–165, mar 2019.

[81] J. Henry and J. Livingstone. Indium phosphide surface processing - an FTIR analysis. *Applied Surface Science*, 78(2):159–163, jun 1994.

[82] J. Chandradass, Dong Sik Bae, and Ki Hyeon Kim. A simple method to prepare indium oxide nanoparticles: Structural, microstructural and magnetic properties. *Advanced Powder Technology*, 22(3):370–374, may 2011.

[83] Martin Eriksson. *Photoluminescence Characteristics of III-Nitride Quantum Dots and Films*. PhD thesis, 2017.

[84] Noah D. Bronstein, Lance M. Wheeler, Nicholas C. Anderson, and Nathan R. Neale. Morphological Control of InxGa1- xP Nanocrystals Synthesized in a Nonthermal Plasma. *Chemistry of Materials*, 30(9):3131–3140, 2018.

[85] Michael K. Carpenter, Thomas E. Moylan, Ratandeep Singh Kukreja, Mohammed H. Atwan, and Misle M. Tessema. Solvothermal synthesis of platinum alloy nanoparticles for oxygen reduction electrocatalysis. *Journal of the American Chemical Society*, 134(20):8535–8542, may 2012.

[86] Elissa Roche, Yamina André, Geoffrey Avit, Catherine Bougerol, Dominique Castelluci, François Réveret, Evelyne Gil, François Médard, Joël Leymarie, Theo Jean, Vladimir G. Dubrovskii, and Agnès Trassoudaine. Circumventing the miscibility gap in InGaN nanowires emitting from blue to red. *Nanotechnology*, 29(46):465602, sep 2018.

[87] Dale E. Newbury and Nicholas W.M. Ritchie. Is scanning electron microscopy/energy dispersive X-ray spectrometry (SEM/EDS) quantitative? *Scanning*, 35(3):141–168, may 2013.

[88] Rebecca Anthony and Uwe Kortshagen. Photoluminescence quantum yields of amorphous and crystalline silicon nanoparticles. *Physical Review B - Condensed Matter and Materials Physics*, 80(11), 2009.

[89] Joo Hyung Kim, Seongcheol Mun, Hyun U. Ko, Gyu Young Yun, and Jaehwan Kim. Disposable chemical sensors and biosensors made on cellulose paper. *Nanotechnology*, 25(9):092001, mar 2014.

[90] R Mohan Sankaran, Dean Holunga, Richard C Flagan, and Konstantinos P Giapis. Synthesis of Blue Luminescent Si Nanoparticles Using Atmospheric-Pressure Microdischarges NANO LETTERS.

[91] Sadegh Askari, Manuel Macias-Montero, Tamilselvan Velusamy, Paul Maguire, Vladmir Svrcek, and Davide Mariotti. Silicon-based quantum dots: Synthesis, surface and composition tuning with atmospheric pressure plasmas. *Journal of Physics D: Applied Physics*, 48(31), 2015.

[92] S. Askari, I. Levchenko, K. Ostrikov, P. Maguire, and D. Mariotti. Crystalline Si nanoparticles below crystallization threshold: Effects of collisional heating in non-thermal atmospheric-pressure microplasmas. *Applied Physics Letters*, 104(16):163103, 2014.

[93] Victor Ivanov, Anna Lizunova, Oxana Rodionova, Andrei Kostrov, Denis Kornyushin, Arseniy Aybush, Arina Golodyayeva, Alexey Efimov, and Victor Nadtochenko. Aerosol Dry Printing for SERS and Photoluminescence-Active Gold Nanostructures Preparation for Detection of Traces in Dye Mixtures. *Nanomaterials*, 12(3):448, feb 2022.

[94] Wei Hung Chiang, Davide Mariotti, R. Mohan Sankaran, J. Gary Eden, and Kostya Ostrikov. Microplasmas for Advanced Materials and Devices, 2020.

[95] Tomohiro Nozaki, Kenji Sasaki, Tomohisa Ogino, Daisuke Asahi, and Ken Okazaki. Microplasma synthesis of tunable photoluminescent silicon nanocrystals. *Nanotechnology*, 18(23):235603, may 2007.

[96] J. McKenna, J. Patel, S. Mitra, N. Soin, V. Švrček, P. Maguire, and D. Mariotti. Synthesis and surface engineering of nanomaterials by atmospheric-pressure microplasmas. *The European Physical Journal Applied Physics*, 56(2):24020, nov 2011.

[97] Sadegh Askari, Manuel Macias-Montero, Tamilselvan Velusamy, Paul Maguire, Vladmir Svrcek, and Davide Mariotti. Silicon-based quantum dots: Synthesis, surface and composition tuning with atmospheric pressure plasmas. *Journal of Physics D: Applied Physics*, 48(31):314002, 2015.

[98] Ozgul Yasar-Inceoglu, Thomas Lopez, Ebrahim Farshihagro, and Lorenzo Mangolini. Silicon nanocrystal production through non-thermal plasma synthesis: A comparative study between silicon tetrachloride and silane precursors. *Nanotechnology*, 23(25):255604, may 2012.

[99] R. N. Pereira, D. J. Rowe, R. J. Anthony, and U. Kortshagen. Oxidation of freestanding silicon nanocrystals probed with electron spin resonance of interfacial dangling bonds. *Physical Review B - Condensed Matter and Materials Physics*, 83(15):155327, 2011.

[100] R. W. Liptak, U. Kortshagen, and S. A. Campbell. Surface chemistry dependence of native oxidation formation on silicon nanocrystals. *Journal of Applied Physics*, 106(6):64313, 2009.

[101] Denise C. Marra, Erik A. Edelberg, Ryan L. Naone, and Eray S. Aydil. Silicon hydride composition of plasma-deposited hydrogenated amorphous and nanocrystalline silicon films and surfaces. *Journal of Vacuum Science Technology A: Vacuum, Surfaces, and Films*, 16(6):3199–3210, 1998.

[102] M. Lattemann, E. Nold, S. Ulrich, H. Leiste, and H. Holleck. Investigation and characterisation of silicon nitride and silicon carbide thin films. *Surface and Coatings Technology*, 174-175:365–369, 2003.

[103] Z Lu, P Santos-Filho, and G Stevens. Fourier transform infrared study of rapid thermal annealing of a-Si:N:H(D) films prepared by remote plasma-enhanced chemical vapor deposition. *Journal of Vacuum Science Technology A*, 13:607, 1995.

[104] G. Lucovsky, J. Yang, S. S. Chao, J. E. Tyler, and W. Czubatyj. Nitrogen-bonding environments in glow-discharge—deposited a - Si:H films. *Physical Review B*, 28(6):3234, sep 1983.

[105] Kirill O. Bugaev, Anastasia A. Zelenina, and Vladimir A. Volodin. Vibrational Spectroscopy of Chemical Species in Silicon and Silicon-Rich Nitride Thin Films. *International Journal of Spectroscopy*, 2012:1–5, 2012.

[106] T Matsumoto, A I Belogorokhov, L I Belogorokhova, Y Masumoto, and E A Zhukov. The effect of deuterium on the optical properties of free-standing porous silicon layers. *Nanotechnology*, 11:340, 2000.

[107] Brandon J. Winters, Jason Holm, and Jeffrey T. Roberts. Thermal processing and native oxidation of silicon nanoparticles. *Journal of Nanoparticle Research*, 13(10):5473–5484, 2011.

[108] J Noborisaka, K Nishiguchi, and A Fujiwara. Electric tuning of direct-indirect optical transitions in silicon. 2014.

[109] Linhan Lin, Zhengcao Li, Jiayou Feng, and Zhengjun Zhang. Indirect to direct band gap transition in ultra-thin silicon films. *Physical Chemistry Chemical Physics*, 15(16):6063–6067, mar 2013.

[110] W. D.A.M. De Boer, D. Timmerman, K. Dohnalová, I. N. Yassievich, H. Zhang, W. J. Buma, and T. Gregorkiewicz. Red spectral shift and enhanced quantum efficiency in phonon-free photoluminescence from silicon nanocrystals. *Nature Nanotechnology 2010 5:12*, 5(12):878–884, nov 2010.

[111] Milan Sykora, Lorenzo Mangolini, Richard D. Schaller, Uwe Kortshagen, David Jurbergs, and Victor I. Klimov. Size-dependent intrinsic radiative decay rates of silicon nanocrystals at large confinement energies. *Physical Review Letters*, 100(6):067401, feb 2008.

[112] Sebastian Binder, Markus Glatthaar, and Edda Rädlein. Analytical investigation of aerosol jet printing. *Aerosol Science and Technology*, 48(9):924–929, 2014.

[113] Thi Cuc Le and Chuen Jinn Tsai. Inertial impaction technique for the classification of particulate matters and nanoparticles: A review. *KONA Powder and Particle Journal*, 38:42–63, 2021.

[114] S. Rennecke and A. P. Weber. The critical velocity for nanoparticle rebound measured in a low pressure impactor. *Journal of Aerosol Science*, 58:135–147, apr 2013.

[115] Virgil Alan Marple. A fundamental study of inertial impactors. *University of Minnesota*, page 266, 1970.

[116] Chih Liang Chien, Chi Yu Tien, Chun Nan Liu, Huajun Ye, Wei Huang, and Chuen Jinn Tsai. Design and Testing of the NCTU Micro-Orifice Cascade Impactor (NMCI) for the Measurement of Nanoparticle Size Distributions. *Aerosol Science and Technology*, 49(10):1009–1018, 2015.

[117] N. J. Wilkinson, M. A.A. Smith, R. W. Kay, and R. A. Harris. A review of aerosol jet printing—a non-traditional hybrid process for micro-manufacturing. *International Journal of Advanced Manufacturing Technology*, 105(11):4599–4619, 2019.

[118] Neil Dalal, Yuan Gu, Guang Chen, Daniel R. Hines, Abhijit Dasgupta, and Siddhartha Das. Effect of gas flow rates on quality of aerosol jet printed traces with nanoparticle conducting ink. *Journal of Electronic Packaging, Transactions of the ASME*, 142(1), 2020.

[119] Pradeep Lall, Jinesh Narangaparambil, Ved Soni, and Scott Miller. Sintering Process Conditions for Additive Printing of Multi-Layer Circuitry Aerosol-Jet Process in Conjunction with Nanoparticle Ink. *InterSociety Conference on Thermal and Thermomechanical Phenomena in Electronic Systems, ITHERM*, 2020-July:805–813, jul 2020.

[120] Chong Huang, William Nichols, Michael Becker, Desiderio Kovar, and John Keto. Supersonic jet deposition of silver nanoparticle aerosols: Correlations of impact conditions and film morphologies. *JOURNAL OF APPLIED PHYSICS*, 101, 2007.

[121] R. Israel and D. E. Rosner. Use of a generalized stokes number to determine the aerodynamic capture efficiency of non-stokesian particles from a compressible gas flow. *Aerosol Science and Technology*, 2(1):45–51, 1983.

[122] K. Wegner, P. Piseri, H. Vahedi Tafreshi, and P. Milani. Cluster beam deposition: A tool for nanoscale science and technology. *Journal of Physics D: Applied Physics*, 39(22):439–459, 2006.

[123] F. Di Fonzo, A. Gidwani, M. H. Fan, D. Neumann, D. I. Iordanoglou, J. V.R. Heberlein, P. H. McMurry, S. L. Girshick, N. Tymiak, W. W. Gerberich, and N. P. Rao. Focused nanoparticle-beam deposition of patterned microstructures. *Applied Physics Letters*, 77(6):910–912, 2000.

[124] Heechul Lee, Sukbeom You, Chang Gyu Woo, Kyunghoon Lim, Kimin Jun, and Mansoo Choi. Focused patterning of nanoparticles by controlling electric field induced particle motion. *Applied Physics Letters*, 94(5):53104, 2009.

[125] P. G. Saffman. The lift on a small sphere in a slow shear flow. *Journal of Fluid Mechanics*, 22(2):385–400, 1965.

[126] I. S. Akhatov, J. M. Hoey, O. F. Swenson, and D. L. Schulz. Aerosol focusing in micro-capillaries: Theory and experiment. *Journal of Aerosol Science*, 39(8):691–709, 2008.

[127] N. J. Kramer, E. S. Aydil, and U. R. Kortshagen. Requirements for plasma synthesis of nanocrystals at atmospheric pressures. *Journal of Physics D: Applied Physics*, 48(3):35205, 2015.

[128] Jaehong Park, Jimin Jeong, Chul Kim, and Jungho Hwang. Deposition of charged aerosol particles on a substrate by collimating through an electric field assisted coaxial flow nozzle. *Aerosol Science and Technology*, 47(5):512–519, 2013.

[129] V. A. Godyak and R. B. Piejak. Insitu simultaneous radio frequency discharge power measurements . *Journal of Vacuum Science Technology A: Vacuum, Surfaces, and Films*, 8(5):3833–3837, 1990.

[130] Valery Godyak. RF discharge diagnostics: Some problems and their resolution. *Journal of Applied Physics*, 129(4), 2021.

[131] Lutz Mädler and Sheldon K. Friedlander. Transport of Nanoparticles in Gases: Overview and Recent Advances. Technical Report 3, 2007.

[132] C. N. Davies. Definitive equations for the fluid resistance of spheres. *Proceedings of the Physical Society*, 57(4):259–270, 1945.

[133] N. P. Rao, H. J. Lee, M. Kelkar, D. J. Hansen, J. V.R. Heberlein, P. H. McMurry, and S. L. Girshick. Nanostructured materials production by hypersonic plasma particle deposition. Technical Report 1-8, 1997.